Elucidating Nanoparticle-Membrane Interactions Through Molecular Dynamics Simulations

by

Carlos Alberto Huang-Zhu

A dissertation submitted in partial fulfillment of
the requirements for the degree of

Doctor of Philosophy

(Chemical and Biological Engineering)

at the

UNIVERSITY OF WISCONSIN — MADISON

2026

Date of Final Oral Exam: 02/24/2026

This dissertation is approved by the following members of the Final Oral Committee:

Reid C. Van Lehn, Associate Professor, Chemical & Biological Engineering

Matthew A. Gebbie, Assistant Professor, Chemical & Biological Engineering

Michael D. Graham, Professor, Chemical & Biological Engineering

David M. Lynn, Professor, Chemistry

© Copyright by Carlos A. Huang-Zhu 2026.
All rights reserved.

Dedication

A mami y papi, por ser el origen de todo. Por el amor incondicional y por inculcar en mí valores vitales para poder enfrentarme a la vida. Gracias por una vida llena de sacrificios que hoy dan frutos y raíces; y por creer en mí desde niño, incluso antes de que yo supiese hasta dónde podía llegar.

A Bea, por tu amor paciente y generoso, por acompañarme en cada etapa de este arduo camino, en los días buenos y en los difíciles. Por escucharme, sostenerme y recordarme quién soy cuando comenzaba a perderme en el camino. Gracias por ser mi calma, mi impulso y mi hogar. Nada de esto tendría el mismo sentido sin ti.

Mis logros son sus logros también. Sin ustedes, no estaría aquí.

Los amo eternamente.

Acknowledgements

This dissertation was made possible by all the contributions from everyone that surrounds me and thus I would like to thank all of them. My time at UW – Madison was a success thanks to all the supportive staff in the Department, friends and colleagues, and especially my advisor, Prof. Reid C. Van Lehn.

I will forever be grateful to Reid for giving me the opportunity to join his research group. It was thanks to him that I discovered the world of computational science for chemistry and biology. Reid has been an extraordinary mentor who tailors his mentorship style according to each of his students' needs. During my time in the group, he has pushed me to grow as a scientist while allowing me to explore my own curiosity. A prime example of this is how he has allowed me to lead the acquisition of computing resources in the group, especially my constant requests for purchasing more powerful GPUs. His excellence goes even further with compassion in personal matters. As I endured grievous situations related to my family's immigration status, Reid provided me with the space and time I needed to support my family. Although I am unable to highlight here all the other meaningful actions that have had an impact in my life, I hope that the ones mentioned are enough to convey my gratitude and appreciation towards Reid.

Thanks to Prof. Matt Gebbie, Prof. Mike Graham, and Prof. Dave Lynn for being part of my PhD committee and supporting my academic development. I am also grateful to my collaborators Professor Shimon Weiss, Professor George W. Huber, Professor James A. Dumesic, and Professor Siddarth H. Krishna for welcoming me into their teams and for entrusting me to support their research endeavors. Working with all of them has been an amazing and fruitful experience. I also want to thank my fellow colleagues Lion Morgenstein, Shimon Yudovich, Hoya Ihara, and Matt Edgar for making collaborating with them an enjoyable experience and I wish them the best in their future careers.

I want to thank all past and present RVL group members for welcoming into the group, teaching me the ways of molecular modeling, and engaging in insightful scientific discussions. Jonathan, Lisa, and Juriti thanks for listening and for providing unconditional support. Throughout my PhD I made several friends whom I cherish, but I want to highlight Carlos

Pérez De Jesús, Kevin Rivera-Sánchez, and Javier Chavarrío Cañas. Carlos and Kevin, thanks for always being truthful and kind – without you I would have not chosen UW – Madison. Javier, thank you for providing both moral and intellectual support since the first day of orientation. Our regular coffee breaks and your knack for pulling me out of my apartment and office offered grounding moments of joy and encouragement throughout this journey.

Finally, I would like to acknowledge the Department of Chemical and Biological Engineering and its staff for their support of my academic and personal development, the Graduate Engineering Research Scholars for fostering a supportive community, and the Chemistry-Biology Training Program for providing opportunities to broaden and deepen my understanding of research at the chemistry–biology interface. This thesis was also made possible by funding from the National Science Foundation under grant DMR-2044997 and a Graduate Research Fellowship; the National Institute of General Medical Sciences under grant T32GM152341; and the Advanced Opportunity Fellowship from the University of Wisconsin – Madison. This thesis used computing resources from the Advanced Cyberinfrastructure Coordination Ecosystem: Services & Support (ACCESS) under grants CTS170045 and CHM230045, and the Euler computing cluster from the College of Engineering at the University of Wisconsin – Madison.

Abstract

Inorganic nanoparticles have shown promise as membrane-active materials in different biomedical applications such as targeted drug delivery, photosensing, antibacterial treatments, and cellular engineering. While experimental approaches have targeted the design and engineering of surface-functionalized nanoparticles, predictions of nano-bio interactions for these materials remain a challenge. Such challenges arise largely due to a lack of mechanistic understanding and design rules to engineer nano-bio interactions. Computational methods, and in particular, molecular dynamics simulations, have been employed to elucidate thermodynamic and mechanistic insight in biophysical processes that are not easily achieved through experiments. Therefore, in this thesis, I apply classical molecular simulations to study nanoparticle-membrane interactions with the objective of providing molecular-scale insight on the thermodynamics and mechanisms of these nano-bio interactions. I hypothesize that subtle and nonobvious changes in molecular structures influence nano-bio interactions. These changes are not captured by conventional macroscopic nanoparticle properties, thus limiting predictions on nanoparticle cellular uptake. In this thesis, I show that chemical modifications to ligand-grafted nanoparticles and physical adsorption of lipids will both drive complex molecular interactions between ligands and lipids that modulate nano-bio interactions. I demonstrate that single ligand descriptors, such as ligand lipophilicity, are insufficient to predict nanoparticle adsorption to lipid bilayers. Instead alkyl chain architecture strongly influences adsorption while lipid membrane mechanics dominate subsequent internalization. Additionally, I demonstrate that lipids can act as linactants to maximize cellular uptake of large nanoparticles and that they can also be used to control electrostatics-mediated adsorption through surface functionalization. Here, I have employed advanced molecular modeling techniques to establish design rules that will guide the future design and engineering of these nanoparticles as membrane-active materials in biomedicine. These findings challenge conventional approaches in which simplified models are assumed by proposing more complex molecular interactions that must also be considered in experimental protocols, but that can positively guide the design space towards safer biomaterials.

Contents

1 Introduction **1**
1.1 Motivation 1
1.2 Chemical modifications in nanoparticle-grafted ligands influence adsorption to lipid bilayers 2
1.3 Physisorbed lipids modulate nanoparticle insertion into biomembranes . . . 3
1.4 Outline of this work 4

2 Ligand Lipophilicity Determines Molecular Mechanisms of Nanoparticle Adsorption to Lipid Bilayers **9**
2.1 Introduction 9
2.2 Methods 12
2.2.1 Coarse-Grained Molecular Dynamics Simulation Parameters 12
2.2.2 System Description and Coarse-Grained Model Parameters 12
2.2.3 Definition of Collective Variables for Free Energy Calculations 14
2.2.4 2D Metadynamics 14
2.2.5 String Method with Swarms of Trajectories 14
2.2.6 Umbrella Sampling Simulations 15
2.3 Results and Discussion 16
2.3.1 Free Energy Landscape Reveals NP Adsorption and Desorption Modulated by Lipid Extraction 16
2.3.2 Potentials of Mean Force along the Minimum Free Energy Paths for NP Adsorption 19
2.3.3 Intercalation of Ligand R Group into the Bilayer Reduces Free Energy Barrier for Adsorption 21
2.3.4 Onset of Lipid Extraction Coincides with Free Energy Barrier for Adsorption 24
2.3.5 Ligand-Specific Adsorption Mechanisms 27
2.4 Conclusions 28

3 Influence of branched ligand architectures on nanoparticle interactions with lipid bilayers 39
3.1 Introduction . . . 39
3.2 Methods . . . 42
3.2.1 Simulation parameters . . . 42
3.2.2 Description of systems . . . 43
3.2.3 Definition of collective variables . . . 44
3.2.4 String method with swarms of trajectories . . . 44
3.2.5 1D umbrella sampling . . . 45
3.3 Results and Discussion . . . 46
3.3.1 Minimum free energy pathway yields reaction coordinate for potential of mean force calculation . . . 46
3.3.2 Branched R groups affect mechanisms of bilayer adsorption . . . 49
3.3.3 Protrusions increase exposure of lipophilic ligand R groups . . . 51
3.3.4 Ligand–lipid contacts relative to hydrophilic contacts provide insight into membrane disruption . . . 52
3.3.5 Branched R groups substantially increases thermodynamic stability of adsorbed AuNPs . . . 54
3.3.6 Surface exposure of lipophilic R groups influences adsorption free energies . . . 56
3.3.7 Ligands with branched R groups exhibit lipid-like behaviors . . . 58
3.4 Conclusions . . . 58

4 Membrane mechanics influence ligand flipping between leaflets 67
4.1 Introduction . . . 67
4.2 Methods . . . 68
4.2.1 Simulation parameters . . . 68
4.2.2 Description of systems . . . 69
4.2.3 System preparation and equilibration . . . 70
4.2.4 Defining the collective variable . . . 70
4.2.5 Ligand flipping steered molecular dynamics . . . 71
4.2.6 Replica-exchange umbrella sampling . . . 71
4.3 Results and Discussion . . . 72
4.3.1 Nanoparticle core induces asymmetry in charged group translocation 72
4.3.2 Ligand leaflet distribution influences free energies of ligand flipping . 74
4.3.3 Transmembrane polar pathways facilitate charged group translocation 76
4.3.4 Ligand splaying induce lipid reorganization . . . 78

4.3.5 Metastability with local membrane thinning minimizes increase in post-flip deformation . . . 79
4.3.6 Branched ligand end groups influence membrane mechanics . . . 82
4.4 Conclusions . . . 83

5 Long-Chain Lipids Facilitate Insertion of Large Nanoparticles into Membranes of Small Unilamellar Vesicles 89
5.1 Introduction . . . 89
5.2 Methods . . . 91
5.2.1 Chemicals . . . 91
5.2.2 TEM Imaging . . . 91
5.2.3 Absorbance Spectroscopy . . . 92
5.2.4 Preparation of NP Embedded SUVs . . . 92
5.2.5 Dynamic Light Scattering . . . 92
5.2.6 Cryo-EM Imaging . . . 92
5.2.7 Data Analysis for Insertion Efficiency . . . 93
5.2.8 Simulation Methods . . . 93
5.2.9 System Setup for Coarse-Grained MD Simulations . . . 93
5.3 Results and Discussion . . . 94
5.4 Conclusions . . . 103

6 Tunable electrostatic interactions of lipid-coated quantum dots and biological membranes 109
6.1 Introduction . . . 109
6.2 Methods . . . 111
6.2.1 Preparation of lcQDs for electrostatic interaction estimation . . . 111
6.2.2 Studying lcQDs-membrane interactions by FACS . . . 112
6.2.3 Electrostatic interactions . . . 112
6.2.4 Simulations of lipid self-assembly on QDs . . . 113
6.2.5 Simulations of lcQD-membrane interactions . . . 113
6.3 Results and Discussion . . . 114
6.3.1 Lipid mixture composition controls electrostatic properties of lcQDs . 114
6.3.2 Self-assembly simulations reveal structures of lipid coatings . . . 115
6.3.3 Lipid coating dictates interactions between lcQDs and HEK cells . . 118
6.3.4 Simulations reveal unbiased lcQD adsorption to anionic membranes . 118
6.3.5 Increasing DOTAP concentration promotes stronger membrane adsorption . . . 120
6.3.6 Lipid-lipid interactions and displacement of ions drive lcQD adsorption 122
6.4 Conclusions . . . 124

7 Conclusion **129**
7.1 General Summary 129
7.2 Key Findings 129
7.3 Future Work 131
7.3.1 Machine-learning a collective variable for AuNP translocation across biomembranes 131
7.3.2 Informing the design of lipid-coated QDs through machine learning . 132

List of Figures

2.1 Molecular structures and reaction coordinate 11
2.2 2D Free Energy Landscape 17
2.3 PMFs along S 20
2.4 Free Energy Barriers and Contacts 22
2.5 Radial Distribution Functions 25
2.6 Descriptors of NP adsorption 26
2.7 Proposed adsorption mechanisms 27

3.1 Molecular structures 42
3.2 Examples of MFEPs 47
3.3 Resolved PMFs for ligand pairs 48
3.4 Free energy barriers to adsorption and snapshots 50
3.5 RDFs quantifying ligand protrusions 52
3.6 Relative hydrophobic-hydrophilic ligand-lipid contacts 53
3.7 Adsorption free energies and snapshots 55
3.8 SASA decrease uopn adsorption 57

4.1 Molecular structures and reaction coordinate 69
4.2 Free energy profiles for NP, ligand, and R group of different chemical groups 73
4.3 Free energy profiles for different chemical groups of AuNP in different states 75
4.4 Coordination numbers for different chemical groups of AuNP in different states 76
4.5 Number densities for different chemical groups of adsorbed AuNP 79
4.6 Membrane fitting and local mean curvature pre- and post-flip 80
4.7 Estimates of leaflet-resolved bending energies for different chemical groups . 81
4.8 Free energy profiles for comparing branched ligands 83

5.1 TEM images and probabilities of QD internalization 96
5.2 NP distance to midplane from cryo-EM images 97
5.3 Long-chain lipid enrichment at the NP-membrane interface 99
5.4 Area density and P_2 order calculations 101

5.5 Schematic of linactant-like behavior by long-chain lipids 102

6.1 Molecular structures 111
6.2 ζ-potential and mean intensity of lcQDs 115
6.3 Computational characterization of simulated lcQDs 117
6.4 Fluorescence intensity from flow cytometry 119
6.5 Number density correlates to lcQD adsorption 120
6.6 Surface charge dictates strength of lcQD adsorption 121
6.7 Displacement of counterions promotes lipid reorganization 123

List of Tables

5.1 Experimental lipid composition of samples 95

Chapter 1

Introduction

1.1 Motivation

Rational design of nanomaterials for biomedical applications such as targeted drug delivery[1], bioimaging[2], biosensing[3], cellular engineering[4], photothermal therapies[5], diagnostics[5], and antimicrobial treatments[6] has been a longstanding challenge. Properties including, but not limited to, electric charge, lipophilicity, and morphology govern nano–bio interactions, and therefore facile tuning of these properties to elicit specific biological responses has become a central goal of nanomedicine.[7] Synthetic inorganic nanomaterials are highly attractive model systems that enable systematic variation of molecular properties while maintaining other nanoparticle (NP) features constant. However, because current state-of-the-art analytical methods capture macroscopic features, biological responses (*e.g.*, cellular internalization, cytotoxicity, hemolysis) are often unsuitably related to molecular descriptors, and in doing so, molecular-scale phenomena are not accounted for. Such neglect often leads to outliers in data that limit the ability to predict nano–bio interactions and hinder the development of novel nanomedicine technologies. Understanding how physicochemical properties influence nano–bio interactions between surface-functionalized NPs and model lipid membranes is therefore imperative to establish crucial design and engineering rules for safe and efficient nano-biomaterials.

In this thesis, I use molecular dynamics (MD) simulations to demonstrate that the interactions between ligand- or lipid-functionalized NPs and lipid bilayers cannot be predicted through single ligand descriptors or any single NP macroscopic property. Instead, non-obvious properties such as ligand end group chain architecture, and complex ligand-ligand, ligand-lipid, and lipid-lipid interactions induce heterogeneities on the surface of functionalized NPs and at the lipid membrane interface to drive NP-membrane interactions. This understanding of how physicochemical properties (*i.e.*, ligands in relation to NPs and lipids in relation to biomembranes) give rise to different descriptors that collectively influence the

cellular internalization process and will inform the future development of nano-biomaterials as biomedical agents.

Here, I present two case studies, each using a different NP model, to elucidate nano–bio interactions. In the first case study, I used gold (Au) NPs functionalized with an organic ligand to systematically study ligand end group effects. Informed by experimental data, we designed different ligands with a cationic end group where each ligand was terminated with different substituents (*e.g.*, alkyl, sulfonate, benzyl) to show that alkyl chain architecture, in addition to ligand lipophilicity, influence NP adsorption. We further show that lipid membrane mechanics dominate the NP translocation across biomembranes as ligand end group effects become negligible. In the second case study, I used octadecylamine-capped (ODA) CdSe/ZnS quantum dots (QDs), with experimental data from collaborators, to demonstrate how lipids play a major role in stabilizing the insertion of large NPs into model membranes and how novel lipid coating methods increase QD-membrane complexation. These two case studies will demonstrate that there exists a complex interplay between ligands and lipids at the molecular scale that cannot be predicted from single ligand descriptors a priori and that is driven by a combination of descriptors altogether.

1.2 Chemical modifications in nanoparticle-grafted ligands influence adsorption to lipid bilayers

Ligand-functionalized gold nanoparticles (AuNPs) represent a versatile platform to study nanoscale phenomena at biological interfaces, especially cellular membranes, thanks to a wide range of methods that enable precise engineering of surface chemistry.[7, 8] Self-assembled ligand monolayers are comprised of organic amphiphiles with hydrophobic backbones (*e.g.*, alkyl chains) that confer stability and hydrophilic groups (*e.g.*, ethylene oxide chains) that confer biocompatibility to AuNPs.[9, 10] Through building block design, these ligands can be end-terminated with functional groups that enable fine control over nano–bio interactions. This approach has been employed extensively in experiments to design AuNPs that interface with cell membranes through non-cytotoxic and non-hemolytic pathways. Objectively, simple physicochemical descriptors such as NP size, surface charge, and ligand lipophilicity (*i.e.*, log P) have been shown to correlate with cellular uptake and membrane adsorption of these AuNPs, yet these relationships often break down across broader ligand chemistries.[10–13] Furthermore, these AuNPs still exhibit unpredictable behavior towards cells for which there is a lack of mechanistic insight.

Computational modeling techniques have been commonly employed to elucidate interaction mechanisms. In particular, classical molecular dynamics (MD) simulations have been

extensively used to model biomolecular systems (*e.g.*, proteins, nucleic acids, lipids, ligands) and understand molecular-level interactions from a mechanistic and thermodynamics perspective (*e.g.*, protein folding, protein-ligand binding, drug solvation free energies). Analogously, these techniques have been applied to design soft materials and study their interactions with biomembranes at the nanoscale. Past studies have used molecular simulations to show that the adsorption to and insertion of AuNPs into lipid bilayers are driven by NP size[14], monolayer composition[14], lipid tail protrusions[15, 16], ligand lipophilicity[17, 18], hydrophobic surface coatings[19], surface ligand rearrangement[20], NP aggregation [21], and ligand anchoring [22]. Therefore, MD simulations represent an ideal platform to systematically engineer the surface of AuNPs and study the effects of ligand end group chemistry on NP adsorption to lipid bilayers. Exploring the large design space of ligands design through computational methods permits the derivation of invaluable design rules that will support and guide future experimental protocols through less resource-intensive approaches.

In this thesis, I propose that single ligand descriptors are insufficient to predict nano–bio interactions *a priori*. Instead, complex molecular level interactions (*i.e.*, ligand-ligand, ligand-lipid, and lipid-lipid) will modulate the mechanisms and thermodynamics of the interactions between AuNPs and lipid membranes. Therefore, I hypothesize that MD simulations can be used to show that ligand end group chemistry will influence adsorption to and insertion into biomembranes through nonobvious pathways.

1.3 Physisorbed lipids modulate nanoparticle insertion into biomembranes

Quantum dots (QDs) are inorganic nanoparticles (NPs) that can be capped with alkyl ligands and possess size-tunable optical properties, high photostability, and sensitivity to electric fields making them a promising nanoscale probe for bioimaging[2], biosensing[3], and membrane-based signal transduction[23]. However, the optimal performance of these QDs relies on their as-synthesized hydrophobic surfaces, which render them poorly compatible with aqueous and cellular environments and increase their cytotoxicity. Because these materials must be both hydrophobic and water-soluble, this inherent dichotomy has hindered the development of inorganic probes for membrane-interfacing applications. Alternatively, ligand-exchange[24] and polymer encapsulation[25] methods increase the solubility of these QDs in aqueous environments at the expense of photophysical performance while precluding their stable incorporation into the hydrophobic core of lipid bilayers. In contrast, the use of lipids physically adsorbed on NPs has been shown to increase biocompatibility and pharmacokinetics.[26–28]

Previous works have used molecular modeling to study NP-membrane interactions on the

basis that lipid bilayers – and lipid components – are an active participant in the modulation of NP translocation. Mainly, lipids will actively reorganize and selectively interact with other lipids or NPs to minimize the cellular membrane's free energy.[29–34] Hence, coarse-grained (CG) MD simulations, which enable access to long time scales and large length scales, are needed to model physically relevant lipid membranes and lipid behavior, particularly heterogeneous NP-embedded biomembranes.

In this thesis, I propose that lipids play a critical role in modulating NP insertion into lipid bilayers and in stabilizing NP-membrane complexes through physical coordination. Rather than chemically modifying the hydrophobic ligands on the surface of QDs, lipids will reorganize to increase mechanically and thermodynamically favorable interactions with the QDs. Therefore, I hypothesize that MD simulations can be used to show that lipids adsorb physically to the surface of hydrophobic QDs to promote favorable NP-membrane interactions.

1.4 Outline of this work

The overarching theme of this thesis is to use classical molecular modeling techniques to elucidate mechanistic and thermodynamic insight on the interactions between surface-functionalized NPs and model lipid membranes. Specifically, I focus on using CG models to study complex reaction coordinates and large-scale systems that would otherwise be too computationally expensive to simulate using fully atomistic systems.

In Chapters 2–4, I investigate the effects of chemical modifications in nanoparticle-grafted ligands. Chapter 2 of this thesis will focus on developing CG models for ligand-coated AuNPs through bottom-up parameterization and subsequently using them to study how ligand end groups influence AuNP adsorption to single-component lipid bilayers. Here, we described the reaction coordinate using two collective variables and employed enhanced sampling techniques to derive minimum free energy pathways and compute free energies while capturing molecular-scale mechanistic insight. Ultimately, showing that AuNP adsorption to lipid bilayer is nonmonotonic with respect to ligand end group lipophilicity due to ligand-ligand interactions within the self-assembled monolayer that influence favorable ligand-lipid interactions. Chapter 3 expands on the library of ligands by including ligand end groups with branched chain architectures that will be compared to their linear analogs (chemically similar with equivalent lipophilicity). We designed additional AuNPs to compare directly two ligands with similar end group lipophilicity but that differ in alkyl chain architecture – mainly linear ligands versus branched ligands. We demonstrate that for pairs of ligands with similar lipophilicity and different chain architecture, the AuNPs with the branched ligands will exhibit lower free energy barriers to adsorption and lower adsorption free energies. Chapter

4 will focus on the effects of ligand end group chemistry on AuNP insertion into lipid bilayers through an iterative ligand flipping mechanism. I implement replica-exchange simulations to model individual ligands flipping from one leaflet to the opposite – representative of a diffusive mechanism for AuNP insertion and subsequent translocation across the lipid bilayer. Finally, I show that after initial AuNP adsorption, the influence of ligand end group chemistry decreases and instead lipid membrane mechanics will facilitate ligand flipping, potentially driving NP insertion.

In chapters 5–6, I investigate the effects of physisorbed lipids from the lipid membrane or from a self-assembled lipid coating. Chapter 5 of this thesis will also focus on modeling large ($>$ 2 nm diameter) alkyl-capped CdSe/ZnS QDs embedded within multicomponent lipid membranes to show long-chain lipids act as linactants to stabilize the insertion of large NPs into biomembranes. Large-scale simulations will show that long-chain lipids displace short-chain lipids and aggregate at NP-membrane interfaces, allowing long lipid tails to fill voids within the QD's ligand monolayer while increasing lipid tail packing and overall membrane rigidity and stability. In addition, these lipids decrease the line tension, resulting in more favorable thermodynamics. Chapter 6 will expand on key conclusions from Chapter 5 to engineer the surface of CdSe/ZnS QDs through a self-assembled monolayer of lipids. Implicit solvent simulations will show that NP-membrane interactions can be controlled by fine tuning the ratio of charged lipids within the QD's lipid coating through the initial lipid mixture. Explicit solvent simulations will then reveal how the surface charge of the QDs, induced by the presence of charged lipids in the lipid coating, promote NP adsorption to negatively charged model membranes by increasing electrostatic attraction.

In Chapter 7, I present a brief summary of this thesis and discuss potential questions with proposed methods that can be explored in future research projects.

References

[1] T. Sun, Y. S. Zhang, B. Pang, D. C. Hyun, M. Yang, Y. Xia, "Engineered Nanoparticles for Drug Delivery in Cancer Therapy", *Angewandte Chemie International Edition* **2014**, *53*, 12320–12364.

[2] X. Gao, Y. Cui, R. M. Levenson, L. W. K. Chung, S. Nie, "In vivo cancer targeting and imaging with semiconductor quantum dots", *Nature Biotechnology* **2004**, *22*, 969–976.

[3] S. Li, K. Zhang, J.-M. Yang, L. Lin, H. Yang, "Single Quantum Dots as Local Temperature Markers", *Nano Letters* **2007**, *7*, 3102–3105.

[4] S. Patel, D. Jung, P. T. Yin, P. Carlton, M. Yamamoto, T. Bando, H. Sugiyama, K.-B. Lee, "NanoScript: A Nanoparticle-Based Artificial Transcription Factor for Effective Gene Regulation", *ACS Nano* **2014**, *8*, 8959–8967.

[5] X. Huang, P. K. Jain, I. H. El-Sayed, M. A. El-Sayed, "Gold Nanoparticles: Interesting Optical Properties and Recent Applications in Cancer Diagnostics and Therapy", *Nanomedicine* **2007**, *2*, 681–693.

[6] X. Jin, N. Peng, A. Cui, Y. Liu, X. Peng, L. Huang, A. Ed-Dra, F. He, Y. Li, S. Yang, M. Yue, "Sodium dodecyl sulfate-coated silver nanoparticles accelerate antimicrobial potentials by targeting amphiphilic membranes", *mLife* **2024**, *3*, 551–564.

[7] A. Gupta, W. Ndugire, C.-M. Hirschbiegel, L. Grigely, V. M. Rotello, "Interfacing Nanomaterials with Biology through Ligand Engineering", *Accounts of Chemical Research* **2023**, *56*, 2151–2169.

[8] R. Mout, D. F. Moyano, S. Rana, V. M. Rotello, "Surface functionalization of nanoparticles for nanomedicine", *Chem. Soc. Rev.* **2012**, *41*, 2539–2544.

[9] M. De, S. Rana, H. Akpinar, O. R. Miranda, R. R. Arvizo, U. H. F. Bunz, V. M. Rotello, "Sensing of proteins in human serum using conjugates of nanoparticles and green fluorescent protein", *Nature Chemistry* **2009**, *1*, 461–465.

[10] K. Saha, S. T. Kim, B. Yan, O. R. Miranda, F. S. Alfonso, D. Shlosman, V. M. Rotello, "Surface functionality of nanoparticles determines cellular uptake mechanisms in mammalian cells", *Small* **2013**, *9*, 300–305.

[11] D. F. Moyano, K. Saha, G. Prakash, B. Yan, H. Kong, M. Yazdani, V. M. Rotello, "Fabrication of Corona-Free Nanoparticles with Tunable Hydrophobicity", *ACS Nano* **2014**, *8*, 6748–6755.

[12] K. Saha, M. Rahimi, M. Yazdani, S. T. Kim, D. F. Moyano, S. Hou, R. Das, R. Mout, F. Rezaee, M. Mahmoudi, V. M. Rotello, "Regulation of Macrophage Recognition through the Interplay of Nanoparticle Surface Functionality and Protein Corona", *ACS Nano* **2016**, *10*, 4421–4430.

[13] Z.-J. Zhu, T. Posati, D. F. Moyano, R. Tang, B. Yan, R. W. Vachet, V. M. Rotello, "The Interplay of Monolayer Structure and Serum Protein Interactions on the Cellular Uptake of Gold Nanoparticles", *Small* **2012**, *8*, 2659–2663.

[14] R. C. Van Lehn, P. U. Atukorale, R. P. Carney, Y.-S. Yang, F. Stellacci, D. J. Irvine, A. Alexander-Katz, "Effect of Particle Diameter and Surface Composition on the Spontaneous Fusion of Monolayer-Protected Gold Nanoparticles with Lipid Bilayers", *Nano Letters* **2013**, *13*, 4060–4067.

[15] R. C. Van Lehn, M. Ricci, P. H. Silva, P. Andreozzi, J. Reguera, K. Voïtchovsky, F. Stellacci, A. Alexander-Katz, "Lipid tail protrusions mediate the insertion of nanoparticles into model cell membranes", *Nature Communications* **2014**, *5*, 4482.

[16] R. C. Van Lehn, A. Alexander-Katz, "Pathway for insertion of amphiphilic nanoparticles into defect-free lipid bilayers from atomistic molecular dynamics simulations", *Soft Matter* **2015**, *11*, 3165–3175.

[17] C. A. Lochbaum, A. K. Chew, X. Zhang, V. Rotello, R. C. Van Lehn, J. A. Pedersen, "Lipophilicity of Cationic Ligands Promotes Irreversible Adsorption of Nanoparticles to Lipid Bilayers", *ACS Nano* **2021**, *15*, 6562–6572.

[18] A. K. Chew, J. A. Pedersen, R. C. Van Lehn, "Predicting the Physicochemical Properties and Biological Activities of Monolayer-Protected Gold Nanoparticles Using Simulation-Derived Descriptors", *ACS Nano* **2022**, *16*, 6282–6292.

[19] Y. Badhe, P. Sharma, R. Gupta, B. Rai, "Elucidating collective translocation of nanoparticles across the skin lipid matrix: a molecular dynamics study", *Nanoscale Adv.* **2023**, *5*, 1978–1989.

[20] P. Gkeka, T. Evangelidis, M. Pavlaki, V. Lazani, S. Christoforidis, B. Agianian, Z. Cournia, "Investigating the Structure and Dynamics of the PIK3CA Wild-Type and H1047R Oncogenic Mutant", *PLOS Computational Biology* **2014**, *10*, 1–12.

[21] F. Lolicato, L. Joly, H. Martinez-Seara, G. Fragneto, E. Scoppola, F. Baldelli Bombelli, I. Vattulainen, J. Akola, M. Maccarini, "The Role of Temperature and Lipid Charge on Intake/Uptake of Cationic Gold Nanoparticles into Lipid Bilayers", *Small* **2019**, *15*, 1805046.

[22] F. Simonelli, D. Bochicchio, R. Ferrando, G. Rossi, "Monolayer-Protected Anionic Au Nanoparticles Walk into Lipid Membranes Step by Step", *The Journal of Physical Chemistry Letters* **2015**, *6*, 3175–3179.

[23] V. De Leo, L. Catucci, A. Falqui, R. Marotta, M. Striccoli, A. Agostiano, R. Comparelli, F. Milano, "Hybrid Assemblies of Fluorescent Nanocrystals and Membrane Proteins in Liposomes", *Langmuir* **2014**, *30*, 1599–1608.

[24] B.-K. Pong, B. L. Trout, J.-Y. Lee, "Modified Ligand-Exchange for Efficient Solubilization of CdSe/ZnS Quantum Dots in Water: A Procedure Guided by Computational Studies", *Langmuir* **2008**, *24*, 5270–5276.

[25] B. Dubertret, P. Skourides, D. J. Norris, V. Noireaux, A. H. Brivanlou, A. Libchaber, "In Vivo Imaging of Quantum Dots Encapsulated in Phospholipid Micelles", *Science* **2002**, *298*, 1759–1762.

[26] M. M. van Schooneveld, E. Vucic, R. Koole, Y. Zhou, J. Stocks, D. P. Cormode, C. Y. Tang, R. E. Gordon, K. Nicolay, A. Meijerink, Z. A. Fayad, W. J. M. Mulder, "Improved Biocompatibility and Pharmacokinetics of Silica Nanoparticles by Means of a Lipid Coating: A Multimodality Investigation", *Nano Letters* **2008**, *8*, 2517–2525.

[27] A. Luchini, G. Vitiello, "Understanding the Nano-bio Interfaces: Lipid-Coatings for Inorganic Nanoparticles as Promising Strategy for Biomedical Applications", *Frontiers in Chemistry* **2019**, *7*, 2296–2646.

[28] Y. Guo, E. Terazzi, R. Seemann, J. B. Fleury, V. A. Baulin, "Direct proof of spontaneous translocation of lipid-covered hydrophobic nanoparticles through a phospholipid bilayer", *Science Advances* **2016**, *2*, e1600261.

[29] Y. Li, X. Zhang, D. Cao, "The Role of Shape Complementarity in the Protein-Protein Interactions", *Scientific Reports* **2013**, *3*, 3271.

[30] A. E. Nel, L. Mädler, D. Velegol, T. Xia, E. M. V. Hoek, P. Somasundaran, F. Klaessig, V. Castranova, M. Thompson, "Understanding biophysicochemical interactions at the nano–bio interface", *Nature Materials* **2009**, *8*, 543–557.

[31] R. Kariuki, R. Penman, S. J. Bryant, R. Orrell-Trigg, N. Meftahi, R. J. Crawford, C. F. McConville, G. Bryant, K. Voïtchovsky, C. E. Conn, A. J. Christofferson, A. Elbourne, "Behavior of Citrate-Capped Ultrasmall Gold Nanoparticles on a Supported Lipid Bilayer Interface at Atomic Resolution", *ACS Nano* **2022**, *16*, 17179–17196.

[32] J. Cardellini, L. Caselli, E. Lavagna, S. Salassi, H. Amenitsch, M. Calamai, C. Montis, G. Rossi, D. Berti, "Membrane Phase Drives the Assembly of Gold Nanoparticles on Biomimetic Lipid Bilayers", *The Journal of Physical Chemistry C* **2022**, *126*, 4483–4494.

[33] T. Pfeiffer, A. De Nicola, C. Montis, F. Carlà, N. F. A. van der Vegt, D. Berti, G. Milano, "Nanoparticles at Biomimetic Interfaces: Combined Experimental and Simulation Study on Charged Gold Nanoparticles/Lipid Bilayer Interfaces", *The Journal of Physical Chemistry Letters* **2019**, *10*, 129–137.

[34] I. Palaia, A. Paraschiv, V. E. Debets, C. Storm, A. Šarić, "Durotaxis of Passive Nanoparticles on Elastic Membranes", *ACS Nano* **2021**, *15*, 15794–15802.

Chapter 2

Ligand Lipophilicity Determines Molecular Mechanisms of Nanoparticle Adsorption to Lipid[1]

2.1 Introduction

Ligand-functionalized gold nanoparticles (NPs) provide platforms for a wide variety of biomedical applications, including drug delivery, biosensing, and photothermal therapy.[1–5] These applications are facilitated by grafting a self-assembled monolayer of organic ligands to the NP surface to modulate interactions with biological materials.[6–10] Selecting or designing ligands to mediate desired nano-bio interactions is a central challenge and opportunity for NP applications. Ligands are commonly designed using a modular structure comprising separately selected backbone and end group moieties.[11–13] Ligand backbones are often alkane chains of varying length, possibly with an ethylene glycol segment inserted to confer stability in biological environments,[14] while end groups can include a wide variety of moieties of varying charge, size, and lipophilicity (*i.e.*, thermodynamic affinity for lipids).[6–10] Varying the ligand backbone and end group properties, as well as the relative proportions of different ligands in multicomponent ligand monolayers,[15] thus leads to a large feasible design space of NP compositions. To guide ligand design, experimental studies have systematically investigated how variations to ligand properties such as end group charge or lipophilicity affect behaviors including cellular uptake,[16, 17] cytotoxicity,[16, 18, 19] antimicrobial activity,[20, 21] and immunological response.[22, 23] Recent computational models have also related descriptors of NP properties to experimentally measured biological activities.[24–31] However, predicting how ligand structure influences nano-bio interactions remains challeng-

[1]This chapter is adapted with permission from Huang-Zhu, Sheavly, Chew, Patel, and Van Lehn, *ACS Nano*, 18:6424-6437, 2024. Copyright 2024 American Chemical Society. Supporting Information (SI) referenced is available at DOI:`https://doi.org/10.1021/acsnano.3c11854`.

ing because subtle differences in ligand chemical properties can manifest as large changes in NP behavior (*e.g.*, swapping the positions of charged moieties in zwitterionic end groups can substantially influence cellular uptake[17]). This challenge is exacerbated for small (< 10 nm in diameter) NPs because the free volume accessible to ligands in the monolayer can influence ligand conformations, which has motivated a number of molecular simulation studies to understand how the interplay of NP size and ligand properties affects the surface properties of NPs in solution.[31–40]Understanding how ligand properties influence interactions between NPs and cell membranes is of particular biomedical importance.[9, 41–43] For example, NP adsorption to the cell membrane can drive intracellular transport,[44] which is critical for applications requiring delivery of NPs to the cell interior, but may also cause membrane disruption and cytotoxicity.[45, 46] Given the complex composition of the cell membrane, simplified lipid bilayer systems, such as supported lipid bilayers (SLBs) and lipid vesicles with a small number of components, are routinely used experimentally as model membranes to enable mechanistic studies of NP-bilayer interactions.[47] Experimental studies of NP-bilayer interactions can be related to biologically relevant behaviors; for example, the adsorption of NPs to lipid bilayers correlates with endocytic uptake,[44] NP-induced disruption of lipid bilayers correlates with cytotoxicity,[48] and the insertion of amphiphilic NPs into lipid bilayers correlates with nonendocytic cell entry.[49] The simplicity of these model systems further permits comparisons to molecular dynamics (MD) simulations. For example, all-atom (AA) and coarse-grained (CG) MD simulations have revealed pathways by which amphiphilic NPs insert into lipid bilayers,[50–54] explained the preferential adsorption of NPs to different lipid phases or phase boundaries,[55–58] and explored the effect of NP charge on bilayer adsorption.[59–62] Together, experiments and corresponding simulations with model membranes permit analysis of how ligand properties affect nano-bio interactions.

Recently, we combined experiments and AA MD simulations to explore the relationship between the lipophilicity of ligand end groups and NP adsorption to single-component lipid bilayers.[63] We studied a library of gold NPs with 2 nm core diameters, each protected by a monolayer of ligands with the structure shown in Figure 2.1A. Each ligand was composed of (1) a backbone consisting of a lipophilic alkanethiol segment and hydrophilic tetraethylene(glycol) segment and (2) an end group consisting of a cationic quaternary ammonium group substituted with two methyl groups and an R group. Different R groups were selected to vary their lipophilicity and the adsorption of the resulting NPs on a 1,2-dioleoyl-sn-glycero-3-phosphocholine (DOPC) SLB was measured via quartz crystal microbalance with dissipation (QCM-D) experiments.[63] These experiments found that increased R group lipophilicity resulted in increased adsorbed mass and increased rate of adsorption as measured by QCM-D. Notably, only the most lipophilic R groups (C_9 and C_1Bn in Figure 2.1B) remained adsorbed after extended rinsing, indicating irreversible adsorption to the SLB. AA

MD simulations, coupled with umbrella sampling calculations, were used to compute the potential of mean force (PMF) for NP adsorption to explain this behavior. PMFs computed by using the distance between the NP and the bilayer center as a collective variable (CV) revealed that adsorption is thermodynamically favorable once sufficient contacts between lipophilic ligand R groups and lipid tails are formed. Separate PMF calculations using the number of these hydrophobic contacts as a CV indicated that contacts were promoted by ligands intercalating within the bilayer, suggesting that intercalation promotes irreversible adsorption.[63] However, the computational expense of AA MD simulations limited these studies to sampling only a single CV at a time for a limited number of NPs, inhibiting more detailed analysis of the impact of ligand R group properties on mechanisms of adsorption and limiting the number of ligand R groups that could be studied.

In this work, we perform CG MD simulations to further investigate the thermodynamics and associated mechanisms of NP adsorption to single-component lipid bilayers as a function of ligand R group lipophilicity. We perform metadynamics calculations to compute the free energy landscape for NP adsorption using both the distance of the NP from the bilayer and the number of NP-lipid contacts as CVs, revealing local free energy minima associated with (1) the adsorption of the NP onto the bilayer and (2) the extraction of lipids from the bilayer and into the ligand monolayer. To further resolve ligand-dependent adsorption mechanisms,

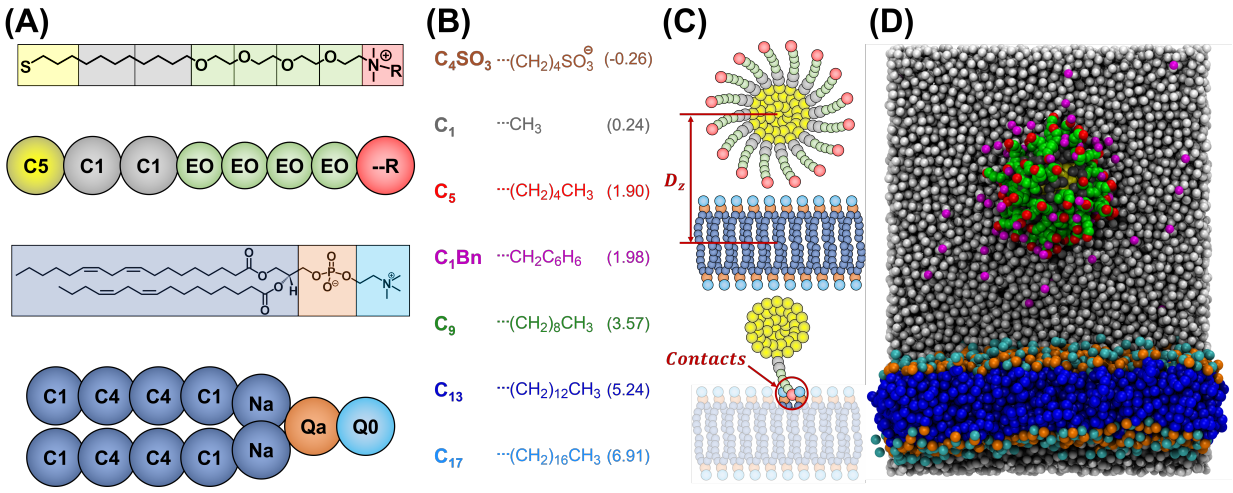


Figure 2.1: (A) AA and CG representations of the ligand chemical structure and the DIPC lipid. Chemical groups are colored according to their coarse-grained bead. (B) Seven R groups studied with their corresponding chemical structures and log P values. Label colors are consistent with colors used in other figures. (C) Schematic illustrating the defined CVs. For each lipid, the choline group is colored cyan, the phosphate group is colored orange, and the tails are colored blue. Water molecules and counterions are included in all simulations but are excluded from this schematic. (D) Snapshot of an equilibrated simulation of a C_1 NP solvated in water (white) neutralized with Cl^- counterions (magenta) and far from a DIPC bilayer; the color scheme follows that in (A). Visual Molecular Dynamics (VMD)[64] was used to generate all simulation snapshots.

we use the string method with swarms of trajectories[65–68] to compute minimum energy paths (MFEPs) for NP adsorption to the upper leaflet of the bilayer from an initial state in solution. The MFEP is defined as the path with the highest likelihood of NP adsorption and is used to quantify the free energy barrier that each NP must cross to adsorb to the bilayer. Comparing the free energy barrier for adsorption for seven different NPs reveals an unexpected nonmonotonic dependence on R group lipophilicity. All seven NPs demonstrate deep minima associated with adsorption without a clear trend in the global adsorption free energy minimum. We relate these findings to the likelihood of lipids to extract from the bilayer and the competition between the intercalation of lipophilic ligands within the bilayer or within the hydrophobic core of the ligand monolayer. Together, these results provide mechanistic insights into kinetic phenomena underlying NP adsorption and how they depend nonintuitively on ligand R group properties.

2.2 Methods

2.2.1 Coarse-Grained Molecular Dynamics Simulation Parameters

All simulations were performed with GROMACS 2021.5[69, 70] patched with PLUMED 2.8.0[71] using a leapfrog integrator with a time step of 20 fs. The temperature was controlled at 300 K using the velocity-rescale thermostat. System equilibration was performed stepwise for a total of 45 ns in the *NPT* ensemble with semi-isotropic pressure coupling at 1 bar using a Berendsen barostat. Production runs were performed with the same parameters used for equilibration with the exception of using the Parrinello-Rahman barostat to control the pressure. A detailed description of other simulation parameters is included in the SI, and details for the production simulations are provided below.

Coarse-grained simulations were performed using the MARTINI force field[72] version 2.3P.[73–76] This version improves aromatic-choline interactions to reproduce membrane-binding events. We also used the refined polarizable water model to model electrostatic interactions more accurately.[75, 76] The use of a polarizable water model improves the treatment of electrostatic interactions to satisfactorily capture behavior from more accurate all-atom (AA) simulations[53, 59] and thus is suitable for analyzing adsorption behavior.

2.2.2 System Description and Coarse-Grained Model Parameters

Following our previous work,[63] we modeled NP adsorption to a single-component zwitterionic lipid bilayer composed of DIPC, which is commonly used as a representation of DOPC in MARTINI simulations.[77] The initial bilayer was generated using the *insane.py* script[78] with dimensions of 14 nm ×14 nm ×24 nm and 289 lipids in each leaflet. After solvating the

NP and the bilayer, the final number of water molecules ranged between 29000 and 31000 with 72 Cl^- counterions to neutralize the cationic ligands; Table S1 reports exact numbers.

We modeled 2 nm diameter gold NPs coated with 72 ligands; this grafting density is based on the average number of ligands per NP measured experimentally for similar NPs.[17] The core of the NP was modeled as a spherical hollow shell following our prior work.[55, 58] All ligands have the modular structure shown in Figure 2.1A. Each ligand consists of an undecanethiol segment, a tetraethylene glycol segment, and an R group. For the thiol segment, we modeled the $S(CH_2)_3$ group as a C5 bead (using MARTINI naming conventions) and each $(CH_2)_4$ group as a C1 bead. For the tetraethylene glycol segment, we modeled each ethylene oxide group using the EO bead model developed by Grunewald *et al.*[79] which has been shown to capture experimentally relevant NP-bilayer interactions in numerous past simulations. [50, 52, 53, 55–57] We mapped the EO bead to each [O-CH_2-CH_2] group instead of its original [CH_2-O-CH_2] group. We chose this mapping to model the quaternary ammonium in the R group as a Q0 (choline) bead in which none of its carbon atoms are considered part of the R group beads. Keeping the original EO bead mapping would require a smaller 3:1 bead mapping for the undecanethiol segment.

Structures of the ligand R groups modeled in this study are shown in Figure 2.1B. R groups were selected based on our previous study and prior experimental studies to ensure that all R groups are experimentally relevant.[63, 80] We modeled cationic ligands comprised of either linear alkanes or a benzyl group to study how R group lipophilicity modulates adsorption thermodynamics and mechanisms. We also modeled a zwitterionic ligand with 1-butanesulfanote bonded to the quaternary ammonium as an R group expected to exhibit a large free energy barrier for adsorption to zwitterionic bilayers. For the R groups, we modeled $(CH_2)_4$ groups as C1 beads, the benzene ring as a cyclic moiety of three SC5 beads (quaternary ammonium bonded to a single SC5 bead that is bonded to the other two SC5 beads), and the 1-butanesulfonate group as an SC1 bead bonded to a Qda bead.[35] The lipophilicity of each R group was quantified by computing log P values using Crippen's method[81] as implemented in ChemDraw 21.0.0 (reported in Figure 2.1B).

Bonded parameters for the ligands were obtained through a bottom-up parametrization approach using data obtained from molecular dynamics simulations using all-atom models of each NP coated with the same number of ligands and solvated in water. We chose to parametrize each ligand independently to capture potential effects on ligand conformations due to grafting to the gold core. Detailed descriptions of our parametrization are included in the Figures S6-S11 in the SI. The 72 ligands were distributed spherically and uniformly to generate the NP, and all C5 beads were bonded to their nearest C5 neighbors within 1.24 nm with a harmonic potential of 5000 kJ/(mol·nm^2) to ensure the stability and rigidity of the core.

2.2.3 Definition of Collective Variables for Free Energy Calculations

We defined two CVs, D_z and contacts, to describe NP adsorption to the bilayer as schematically shown in Figure 2.1C. D_z quantifies the distance in the z dimension between the center of mass of the NP (including its ligands) and the center of mass of 20 randomly selected lipids from the bilayer (10 from the upper leaflet and 10 from the lower leaflet). D_z is reported either as a distance in units of nm or as a unitless value that is scaled by the z-dimension of the simulation box. For metadynamics calculations, we sampled D_z in nm, while for free energy calculations we used D_z as a unitless value to ensure appropriate biasing of the CVs regardless of possible bilayer or box size changes during sampling. Contacts quantify the number of CG beads from one set of beads that are within 0.47 nm (the standard diameter of MARTINI beads) of any bead from another set of beads. For metadynamics and free energy calculations, a contact was counted when any NP bead was within the specified cutoff of any lipid bead. For other analyses, a contact was defined between specific subgroups of beads: ligand backbone beads and lipid tail beads, ligand R group beads and lipid tail beads. All CVs were computed using the DISTANCE (D_z) and COORDINATION (contacts) collective variables in PLUMED 2.8.0.[71]

2.2.4 2D Metadynamics

We performed 2D well-tempered metadynamics[82] to approximate the free energy landscape for NP adsorption to the bilayer as a function of D_z and contacts. These simulations were initiated with the NP far from the bilayer. The two CVs were biased using two-dimensional Gaussian hills with a height of 0.2 kJ/mol and width of 0.2 nm for D_z and 1 contact. Hills were deposited every 20 steps (400 ps) during a 500 ns simulation with a bias factor of 10 kJ/mol. Four walkers were sampled simultaneously for a total of 2 μs of sampling time. To avoid sampling configurations with large D_z (*i.e.*, with the NP diffusing in solution far from the bilayer), we imposed an upper wall on the scaled value of D_z at 0.40 with a harmonic potential of 150000 kJ/mol. The contacts sampled were those between all NP beads and all lipid beads. Metadynamics was only performed for the C_1 NP with convergence being shown in Figure S12.

2.2.5 String Method with Swarms of Trajectories

We used the string method with swarms of trajectories[65–67] to compute the minimum free energy path (MFEP) for NP adsorption to the bilayer as a function of D_z and contacts. We chose the initial string for each MFEP as the pathway that connects two states, the NP in solution and the NP adsorbed to the upper leaflet of the bilayer, which are expected to represent stable equilibrium states (Figure 2.2).[63] Each string was comprised of

24 evenly spaced independent windows. Restrained simulations were performed to equilibrate the CVs and generate a set of 128 independent configurations (from each restrained simulation) that were subsequently used to generate 24 swarms of unbiased simulations (*i.e.*, the swarms of trajectories). The average drift computed from the unbiased trajectories for each window was added to the old CVs to evolve the string. A new string was generated by linearly interpolating through the new sets of CVs and reparameterized to ensure equal distances between consecutive windows.[65–67] A total of 75 iterations was required to achieve convergence (Figures S14-S20). Since the string method with swarms of trajectories is a finite-temperature method, the final path fluctuates slightly every iteration even after convergence. Therefore, we determined the MFEP by averaging the last five strings using a spline fit. A more detailed description and a schematic depicting this method are shown in the SI.

2.2.6 Umbrella Sampling Simulations

We performed 1D umbrella sampling to compute the PMF as a function of the distance along the MFEP. We used the path CV equations defined by Branduardi *et al.*[68] to define the distance along the path, S, and the normal distance away from the path, Z. The MFEP was discretized into 72 windows evenly spaced in S. Each umbrella sampling window was restrained at a chosen value of S using strong harmonic potentials near the region between where the NP begins making contacts with the bilayer and where the adsorption process begins; weak harmonic potentials were used for all other values of S. The values of these restraints were slightly varied for each NP and for each replica to ensure numerical stability, particularly for cases in which the NP interacted very strongly with the bilayer (*i.e.*, due to strong lipid extraction and NP desorption). The restrained values of S and their corresponding spring constants are included in the SI. In all simulations, the value of Z was restrained at 0.02 using a harmonic potential of 20000000 kJ/mol to restrict sampling to the MFEP. For each window, we performed a 50 ns production run and discarded the first 5 ns as equilibration. The last 45 ns were used to compute the PMF in terms of S using the Weighted Histogram Analysis Method (WHAM).[83] For the C_4SO_3 NP, we discarded the first 10 ns as equilibration and used the last 40 ns for analyses. WHAM was performed as a function of both S and Z, with the final PMF reweighted to be a function of S only. To ensure robustness, the string method and umbrella sampling were repeated at least once for all NPs to ensure fully independent strings and PMFs between replicas. Due to the computational expense, two replicas were performed for all NPs and an additional replica (with a new string) was performed for NPs that exhibited instability during umbrella sampling (described in the SI).

2.3 Results and Discussion

2.3.1 Free Energy Landscape Reveals NP Adsorption and Desorption Modulated by Lipid Extraction

In our past computational and experimental study, we found that the adsorption of NPs (functionalized with a subset of the ligands shown in Figure 2.1B) to DOPC lipid bilayers depends upon the lipophilicity of the ligand R group.[63] Increasing R group lipophilicity led to a transition from a reversibly adsorbed state to an irreversibly adsorbed state as quantified using QCM-D experimental measurements. AA simulations indicated that this difference could be related to the propensity of more lipophilic ligands to intercalate within the bilayer, eventually leading to the extraction of lipids from the bilayer and into the ligand monolayer.[63] However, it is too computationally expensive to sample the free energy landscape underlying the extraction of lipids using AA simulations, motivating CG simulations to model the adsorption process for a larger set of ligand R groups in this study to understand mechanisms influencing NP adsorption as a function of ligand properties. Figure 2.1A shows the chemical structures and CG models of the cationic ligand structure and DIPC lipid (which has 16-18 carbon tails with two cis-unsaturated bonds on each tail and is used to represent DOPC in the CG simulations), and Figure 2.1B shows the seven ligand R groups we used in this study. Each R group is labeled with a corresponding value of its octanol-water partition coefficient (log P) as a measure of lipophilicity; larger, more positive values of log P indicate increasingly lipophilic R groups. The seven R groups span a range of log P values and consist of five R groups with varying alkyl chain lengths (C_1, C_5, C_9, C_{13}, and C_{17}), a benzyl group (C_1Bn), and an alkyl chain terminated in a sulfonate group (C_4SO_3). Ligands with all R groups excluding C_4SO_3 have a net positive charge due to the quaternary ammonium groups; the negative charge on the C_4SO_3 group causes its corresponding ligand to be neutral. This set of ligand exceeds those that we previously studied[63] by including longer alkyl groups (C_{13} and C_{17}) to probe larger values of log P and by including the zwitterionic C_4SO_3 to probe the impact of R group charge. CG parameters for all ligands were obtained following a bottom-up approach by reproducing more accurate AA MD simulations as detailed in Figures S6-S11 in the Supporting Information (SI).

To first gain insight into NP-bilayer adsorption behavior, we performed 2D well-tempered metadynamics[82] simulations in a space defined by two collective variables (CVs): the distance between the NP and the bilayer (D_z) and the number of contacts formed between the NP and the bilayer (contacts). A representative schematic of these CVs is shown in Figure 2.1C. Four walkers were simultaneously sampled every 400 ps during 500 ns production runs for a total of 2 μs of sampling time. Figure 2.2 shows the free energy landscape for the adsorption of the C_1 NP to a DIPC lipid bilayer. An upper wall is imposed to restrict the NP to sample values of D_z close to the bilayer (described in Methods) which may bias

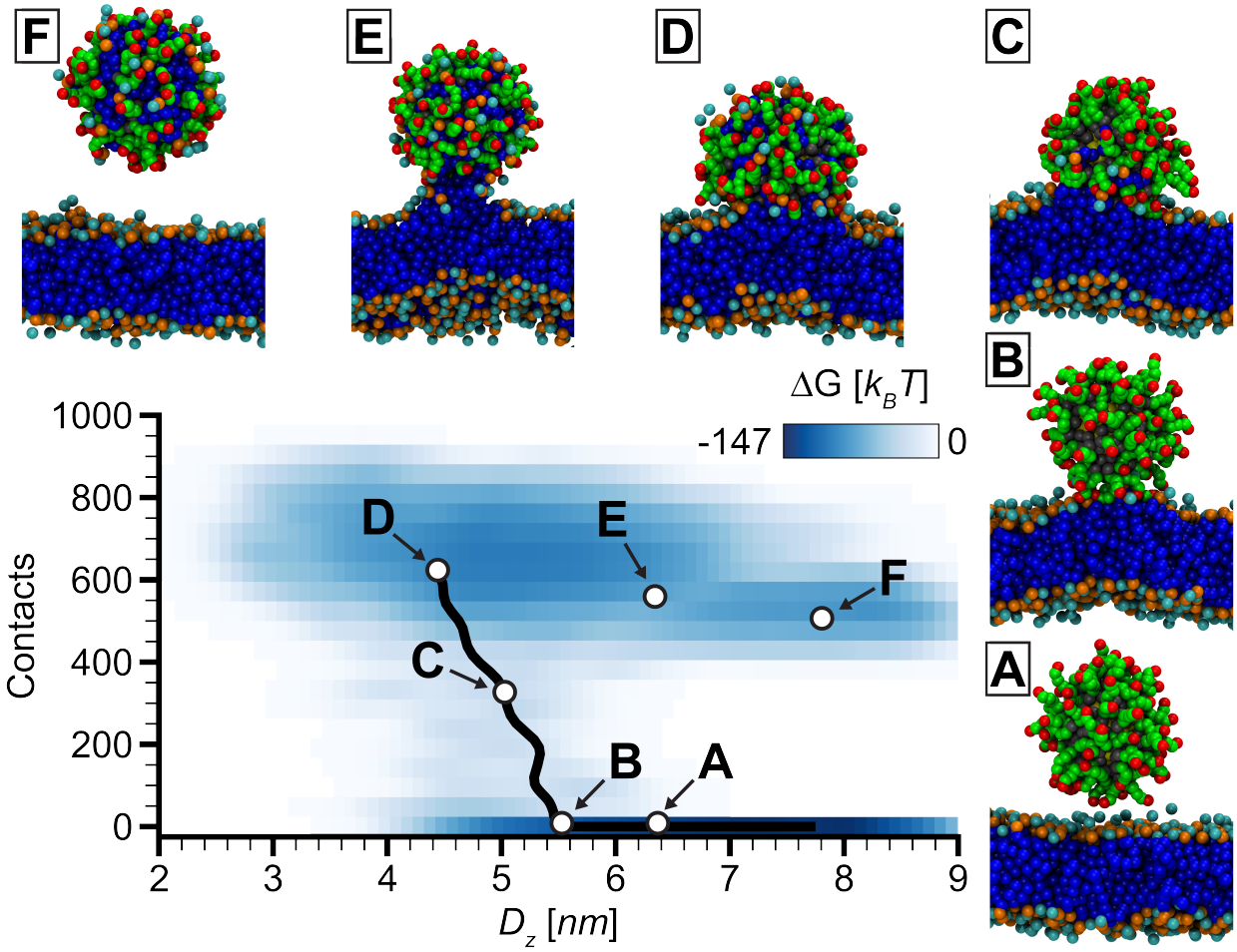


Figure 2.2: Free energy landscape for the adsorption of the C_1 NP computed using metadynamics. Regions of the free energy landscape are labeled according to representative simulation snapshots that show the NP-bilayer interactions at the defined set of CVs. Note that an upper wall is imposed to prevent large values of D_z from being sampled (as described in Methods). The MFEP computed using the string method with swarms of trajectories is overlaid (black line) to show that the MFEP connects two low free energy basins on the landscape. In the simulation snapshots, the NP and lipids are color coded as described in Figure 2.1A. Water molecules and ions are not shown. Lipids from the bilayer that are in front of the center of mass of the NP and farther than 2.5 nm of the S1 beads are not shown to visualize ligand intercalation in the bilayer while allowing visualization of lipids extracted onto the NP monolayer.

the numerical values of the free energies obtained from these calculations. Nonetheless, the metadynamics calculations are valuable for qualitatively identifying several important regions in the free energy landscape for NP adsorption; Figure 2.2 labels important regions with points and shows corresponding simulation snapshots. We now describe these points sequentially to highlight the sequence of events that may occur during the interaction with a bilayer.

The initial configuration of the NP is point A, which corresponds to a NP in solution away from the bilayer (large D_z) and not in contact with any lipids (zero contacts). The

free energy in this region is a local minimum. The NP can then approach the bilayer (decreasing value of D_z), which is associated with an increase in free energy, until reaching point B. Point B corresponds to the free energy barrier for adsorption and occurs when the NP initiates contacts with the bilayer. Metadynamics simulations do not sample the free energy landscape with sufficiently fine resolution near the free energy barrier to resolve its value; this limitation, as well as the limitation associated with the upper wall noted above, motivates the use of the string method with swarms of trajectories and umbrella sampling to compute this barrier (*vide infra*). Further decreasing D_z from point B likewise increases the number of contacts to reach point C, which lies within a low free energy basin. The snapshot at this point illustrates that the increase in contacts is due to the extraction of lipids from the bilayer and into the ligand monolayer. Once sufficient lipids are extracted, the NP adsorbs to the upper leaflet and the bilayer relaxes the deformations associated with the adsorption process, leading to a local free energy minimum at point D. Taken together, analysis of the free energy landscape indicates that NP adsorption is favorable due to lipid extraction that occurs after the NP initiates favorable contact with the hydrophobic core of the bilayer, which is in agreement with our prior AA MD simulations.[63] Further analysis confirming that lipid extraction is thermodynamically favorable, in agreement with this result, is presented in Figures S1-S5 in the SI.

The sequence represented by points A-D represents the expected adsorption process and highlights the importance of lipid extraction from the bilayer to stabilize the adsorbed state. However, the metadynamics calculations further reveal that the free energy landscape includes a region associated with the desorption of a NP with extracted lipids. Specifically, increasing D_z from point D with the number of contacts approximately constant leads to point E, in which the NP begins to detach from the bilayer while maintaining a "lipid bridge". The bridge eventually relaxes when the NP completely desorbs into solution at point F. Point F is similar to point A but is lower in free energy due to the favorable extraction of lipids from the bilayer; extracted lipids fill free volume within the NP monolayer to shield the hydrophobic NP surface area from water in agreement with prior simulations.[37, 51, 63] There is no apparent pathway from point A to point F without passing through a surface-adsorbed state; therefore, free energy calculations that sample only D_z as a CV may fail to detect point F, which could lead to a bias in free energy calculations depending upon the manner in which initial configurations are generated (*e.g.*, by permitting the extraction of lipids or not).[50, 63] Indeed, this behavior was observed in our past AA MD simulations, in which we observed hysteresis in the free energy computed as a function of D_z depending on whether initial configurations included large numbers of lipid contacts.[63] The results and configurations obtained in Figure 2.2 are thus consistent with those AA simulations and indicate that favorable lipid extraction occurs over long time scales not sampled in the AA simulations, highlighting the importance of explicitly biasing the formation of NP-bilayer

contacts.

2.3.2 Potentials of Mean Force along the Minimum Free Energy Paths for NP Adsorption

To complement the mechanistic insight gained from analyzing the free energy landscape, and to more accurately resolve the free energy barrier for NP adsorption, we established an alternative approach to compute a potential of mean force (PMF) using 1D umbrella sampling. We computed the most probable path for NP adsorption to the bilayer in terms of the same two CVs used during metadynamics by using the string method with swarms of trajectories, as described in Methods and schematically illustrated in Figure S13, to compute the MFEP.[65–68] This approach involves iteratively evolving strings composed of sets of physically relevant CV values toward a converged path between two free energy basins, labeled by states A and D in Figure 2.2, that passes through state C. The converged path is defined as the MFEP. To confirm the validity of the MFEP calculations, Figure 2.2 overlays the final converged string for one replica of the C_1 NP on the free energy landscape to show that it samples CV regions associated with an increase in NP-bilayer contacts and a decrease in D_z. The evolution of strings for all seven NPs (one replica) are included in Figures S14-S20 in the SI; MFEPs for all seven NPs appear similar to the MFEP shown in Figure 2.2. The MFEP was expressed using path CV equations[68] described by the distance along the path, S, and the distance away from the path, Z. 1D PMFs were then computed as a function of S, with additional details and data on convergence described in Figures S21-S26 in the SI.

Figure 2.3A shows PMFs as a function of S for all seven NPs. All PMFs have qualitatively similar features; PMFs for additional replicas are shown in Figures S27-S33 in the SI and exhibit similar features. Low values of S correspond to configurations where the NP is in solution far from the bilayer (state A in Figure 2.2 with large D_z and zero contacts). Accordingly, PMF values were set to zero for $S = 0$ so that the PMF represents the change in free energy associated with NP adsorption from an initial state in solution. All PMFs exhibit maxima for $0.3 < S < 0.5$. These values of S correspond to state B in Figure 2.2, where the NP comes close to the bilayer and initiates contact with the lipids, followed by lipid extraction after enough contacts are made. We associate these PMF maxima with NP-specific free energy barriers for adsorption, as discussed in detail below. Some PMFs also exhibit a local maximum and minimum prior to the global PMF maximum, which occurs when a low number of lipids are initially extracted before a larger number are extracted in subsequent windows (discussed in more detail below); when this behavior was observed, an additional simulation replica was performed to ensure adequate sampling near the PMF maximum. As S further increases, all PMFs decrease due to a decrease in D_z and an increase in contacts that promote lipid extraction (state C in Figure 2.2). Large values of

S correspond to NP adsorption to the upper leaflet of the bilayer with numerous extracted lipids stabilizing the adsorbed configuration (state D in Figure 2.2 with large D_z and a large number of contacts).

While all PMFs demonstrate qualitatively similar features, there are distinct quantitative differences depending upon the ligand R group. To explore these differences, we first define the adsorption free energy as the minimum value of the PMF as a function of S because this quantity reflects the free energy difference between state A (in solution) and state D (adsorbed to the upper leaflet of the bilayer); more negative values indicate that adsorption is more favorable. The adsorption free energies range between approximately $-47\ k_BT$ and $-202\ k_BT$, indicating that adsorption is favorable for all NPs. The observation of lipid extraction for all NPs indicates that negative adsorption free energies are due to favorable hydrophobic interactions between ligands and extracted lipids, with differences in the adsorption free energies attributed to differences in electrostatic and hydrophobic interactions between ligand R groups and lipid head groups. Adsorption is least favorable for the C_4SO_3 NP, which is expected given the weaker electrostatic interactions between lipid head groups and its zwitterionic R group compared to the cationic R groups for all other NPs. Adsorption is most favorable for the C_1Bn NP which can be attributed to stronger cation$-\pi$ binding

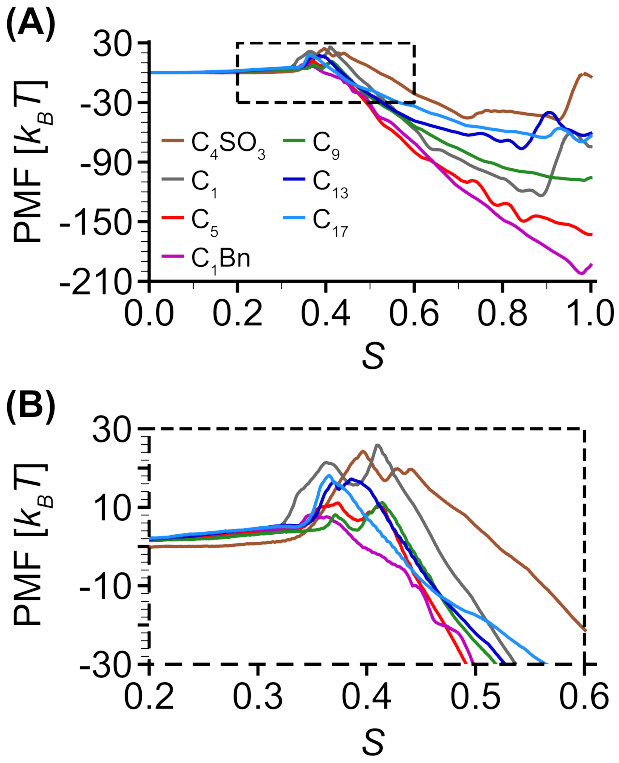


Figure 2.3: Potentials of mean force (PMFs) for the seven NPs with ligands shown in Figure 2.1B. PMFs are computed as a function of the distance along the MFEP, S. (A) Complete PMFs. (B) Enlarged PMFs to show differences in PMF maxima, which likewise indicate differences in free energy barriers of adsorption modulated by the physicochemical properties of the ligands and distinct NP-bilayer interaction mechanisms.

interactions.[73] For the remaining ligands with linear alkyl R groups, adsorption is more favorable for shorter, less lipophilic R groups (C_1, C_5, and C_9) than longer, more lipophilic R groups (C_{13} and C_{17}). This result is counterintuitive, as more lipophilic R groups might be expected to promote adsorption; this behavior reflects the reduced free volume in the monolayers of NPs with long, lipophilic R groups due to interactions between ligand R groups and ligand backbones, as further elaborated upon below.[84] Despite these R-group-specific differences in adsorption free energies, all adsorption free energies are sufficiently favorable that differences among predicted values would not influence experimentally observed adsorption behavior significantly. Therefore, we next focus on the values of the PMF maxima to understand if ligand R groups influence adsorption behavior by impacting free energy barriers to adsorption.

2.3.3 Intercalation of Ligand R Group into the Bilayer Reduces Free Energy Barrier for Adsorption

Figure 2.3B presents enlarged portions of the PMFs corresponding to values of S where the PMFs reach maxima. This plot shows differences in PMF maxima for different ligand R groups that correspond to differences in the barriers to adsorption. Prior work has shown that free energy barriers for the insertion of lipophilic groups into bilayers, similar to the behavior observed in Figure 2.2, can be related to the formation of contacts with lipid tails.[63, 84, 85] Therefore, we further outline quantitative comparisons between the thermodynamics and the molecular mechanisms that modulate NP adsorption to the upper leaflet of the bilayer to elucidate the role of lipophilicity during this process. Specifically, Figure 2.4B shows the free energy barrier for adsorption (from the PMFs in Figure 2.3) for each NP and Figure 2.4C quantifies the number of contacts between different groups computed from the umbrella sampling window that is closest in CV space to the value of S corresponding to each PMF maximum. Comparing these values to each other and to simulation snapshots of the same umbrella sampling windows in Figure 2.4A identifies several relevant ligand-lipid interactions that characterize the adsorption process, as we next describe.

The C_4SO_3 and C_1 NPs exhibit large free energy barriers of $19.2 \pm 4.1\ k_BT$ and $24.0 \pm 3.6\ k_BT$, respectively. The ligands for these NPs have low lipophilicity and solvent-exposed charged groups, suggesting that the interactions with the bilayer are primarily driven by electrostatic interactions. Simulation snapshots (Figure 2.4A) reveal that the free energy barrier to adsorption for these NPs is associated with strong membrane deformation induced by the partitioning of lipid tail groups into the NP hydrophobic core from the hydrophobic bilayer bulk, which we refer to as "lipid protrusions". Lipid protrusions are promoted by hydrophobic interactions between the nonpolar groups in the ligand backbones and the tails of the lipids as shown by the large number of contacts between ligand backbone and lipid

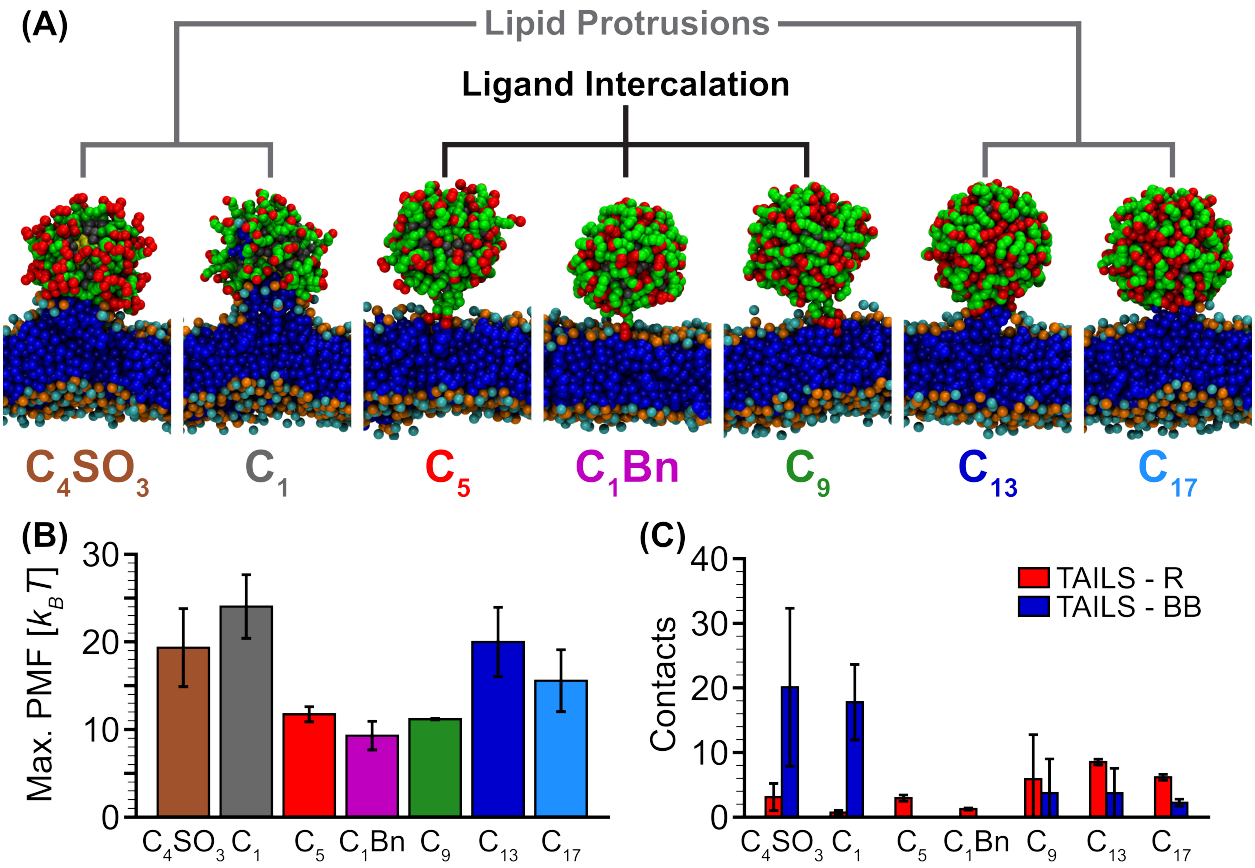


Figure 2.4: Comparison of free energy barriers to adsorption and ligand-lipid contacts. (A) Representative simulation snapshots of configurations from the umbrella sampling window corresponding to the free energy barrier for adsorption. The NP and lipids are color coded as described in Figure 2.1A. Water molecules and ions are not shown. Lipids from the bilayer that are in front of the center of mass of the NP and farther than 2.5 nm away from the S1 beads are not shown to visualize ligand intercalation in the bilayer and lipid extraction to the NP monolayer. (B) Maximum value of the PMF for each NP, which is defined as the free energy barrier of adsorption. (C) Contacts between lipid tails and either ligand R groups (TAILS - R) or ligand backbone groups (TAILS - BB). Contacts were computed from the same window used for the snapshots in (A). Error bars in (B) and (C) were calculated as the standard deviation between three replicas for C_4SO_3 and C_1 NPs and between two replicas for C_5, C_1Bn, C_9, C_{13}, and C_{17} NPs.

tail beads in Figure 2.4C. Because the R groups for these NPs are charged, lipid protrusions require the lateral displacement of ligand R groups and lipid head groups, which interact with each other through Coulombic interactions, as shown by the small number of contacts between ligand R groups and lipid tail groups in Figure 2.4C. The resulting "lipid bridge" structure that forms due to lipid protrusions (Figure 2.4A, and previously noted in Figure 2.2) resembles the high-energy stalk commonly observed during vesicle fusion.[51, 86, 87] This substantial bilayer disruption explains the large free energy barrier associated for adsorption of these NPs.

The C_5 ($11.7 \pm 0.9\ k_BT$), C_1Bn ($9.3 \pm 1.6\ k_BT$), and C_9 ($11.2 \pm 0.1\ k_BT$) NPs exhibit

substantially lower free energy barriers compared to the C_4SO_3 and C_1 NPs. The ligands for these NPs are of intermediate lipophilicity, and the corresponding simulation snapshots in Figure 2.4A indicate that their R groups insert into the upper leaflet of the bilayer due to favorable hydrophobic interactions with lipid tails. These configurations are consistent with the low-energy ligand intercalation mechanism identified in prior AA simulations.[63] Figure 2.4C indicates that intercalation primarily leads to contacts between the lipophilic R groups and lipid tail groups. While the C_9 NP also has contacts between ligand backbones and lipid tails, no visible lipid protrusions are observed, and these contacts are instead generated by the intercalated R group pulling the NP core and lipid tails close together without extracting the lipids from the bilayer. The lack of notable bilayer disruption associated with ligand intercalation explains the lower adsorption barrier for these three NPs.

Surprisingly, the C_{13} ($20.0 \pm 4.0\ k_BT$) and C_{17} ($15.6 \pm 3.5\ k_BT$) NPs exhibit free energy barriers comparable to those of the C_4SO_3 and C_1 NPs that are larger than the free energy barriers for the C_5 and C_9 NPs, even though C_{13} and C_{17} NPs are coated with linear alkyl-terminated ligands that are longer and more lipophilic than the C_5 and C_9 NPs. This comparison indicates that there is a nonmonotonic variation in the free energy barrier for adsorption as a function of ligand lipophilicity. Simulation snapshots indicate that unlike the C_5, C_1Bn, and C_9 NPs, the longer C_{13} and C_{17} R groups do not intercalate into the bilayer and instead lipid protrusions mediate contact with the NP as with the shorter C_1 and C_5 ligands, although the bilayer is noticeably less disrupted. Figure 2.4C confirms that both R groups and ligand backbones are in contact with tail groups, with the large number of backbone-tail group contacts being consistent with lipid protrusions and the formation of a high-energy lipid bridge.

To explain the inability of the C_{13} and C_{17} R groups to intercalate in the bilayer, we hypothesized that hydrophobic interactions with ligand backbones cause the ligands to fold back and bury R groups within the ligand monolayer, where they are shielded from the surrounding solvent. This "backfolding" behavior inhibits the extension of the R group out of the ligand monolayer and into contact with the lipid bilayer. To test this hypothesis, we explored the capacity of R groups from each NP to extend into solution by computing radial distribution functions (RDFs) from unbiased simulations of each NP in solution (*i.e.*, in the absence of lipids). These unbiased simulations were equilibrated with isotropic pressure coupling as described in the SI, and then sampled every 10 ps during a 50 ns production trajectory. We expect that ligand backfolding would result in the charged quaternary ammonium being exposed to solvent, while the last bead of the R group would be close to the core of the NP. RDFs were thus computed for the quaternary ammonium and the last bead of the ligands using the center of mass of the NP as reference. Figure 2.5 compares these RDFs for six NPs excluding the C_1 NP (since its R group bead is the quaternary ammonium

bead). The RDFs for the quaternary ammonium group and R group for the C_4SO_3 NP overlap, indicating that the R group extends toward solution as expected due to its zwitterionic nature. RDFs for the more lipophilic ligands (C_5, C_1Bn, and C_9) also overlap, albeit to a lesser degree, indicating that the R groups can extend appreciably into solution. In contrast, RDFs for the longer lipophilic ligands (C_{13} and C_{17}) show minimal overlap such that the R group is localized near the core of the NP. These results support the hypothesis that only the C_{13} and C_{17} R groups exhibit substantial backfolding, which explains their inability to intercalate into the bilayer.

2.3.4 Onset of Lipid Extraction Coincides with Free Energy Barrier for Adsorption

To further quantify the relationship between lipid protrusions, lipid extraction, and free energy barriers for adsorption, Figure 2.6 compares values of D_z, contacts, and the number of lipids extracted computed for each umbrella window along the MFEP for one replica of the C_1, C_1Bn, and C_{13} NPs, which are the NPs with the smallest (C_1Bn) and two largest (C_1 and C_{13}) free energy barriers. We classify a lipid as being extracted when its phosphate group is coordinated to (1) at most one phosphate group of another lipid and (2) at least one quaternary ammonium of the NP ligands. The cutoff distance for phosphate-phosphate coordination was chosen as 1.1 nm from the radial distribution function of phosphate groups in a plain bilayer. The cutoff distance for the phosphate-ammonium coordination was chosen as 1.2 nm by matching the computed number of lipids extracted to the simulation snapshots; this cutoff consistently yielded good agreement between quantitative measurements and qualitative observations.

All three plots exhibit a similar increase in the PMF as D_z decreases prior to the formation of contacts with the bilayer. Upon the initial increase in contacts (near $S = 0.3$), however, the C_1 and C_{13} NPs show a sharp increase in the PMF. Both NPs exhibit similar features with the increase in the PMF and number of contacts coinciding with the initial extraction of lipids from the bilayer. The PMF maxima are reached at a larger value of S after more lipids are extracted. These behaviors are characteristic of initial lipid protrusions followed by substantial lipid extraction. One difference between the C_1 and C_{13} NPs is the first local maximum observed for the C_1 NP, which coincides with the first lipid being extracted (Figure 2.6A). Similar behavior is occasionally observed in other PMFs and is attributed to the stochastic nature of lipid extraction. In contrast to the behavior of the C_1 and C_{13} NPs, the PMF maximum for the C_1Bn NP (Figure 2.6B) coincides with first lipid contacts and occurs with minimal lipid extraction. These behaviors are characteristic of ligand intercalation, which increases contacts without extracting lipids. Together, these observations quantify the extent of lipid extraction associated with lipid protrusions compared to ligand intercalation.

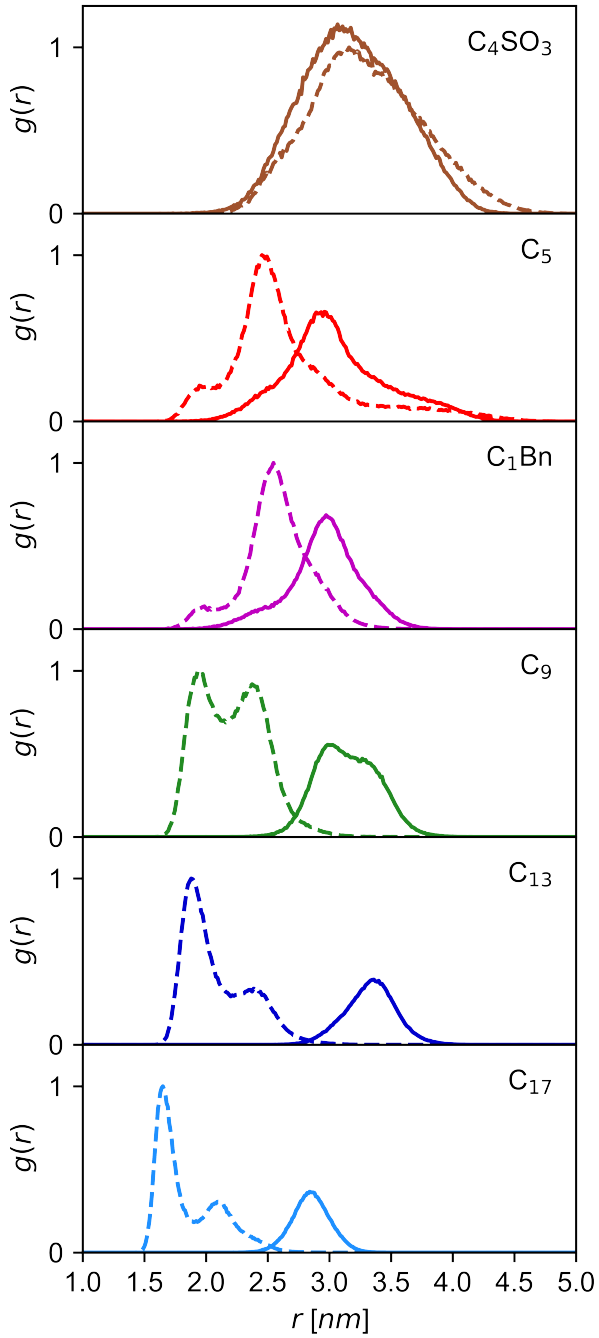


Figure 2.5: Radial distribution functions, $g(r)$, computed for the quaternary ammonium bead (solid lines) and the last bead of each ligand R group (dashed lines) using the center of mass of the NP as reference. The RDF for the C_1Bn NP was computed with the center of mass of the benzene ring. All data were normalized using the maximum counts for the last bead and were computed from a single unbiased simulation of each NP in solvent. The *gmx rdf* tool was used with a bin size of 0.01 nm.

Moreover, all NPs eventually extract lipids as the PMFs decrease, indicating that lipid extraction is a key factor in stabilizing NP adsorption. This prevalence of lipid extraction is consistent with prior studies that have shown the extraction of lipids to form a lipid corona

around charged NPs.[88–91]

Since lipid extraction refers specifically to lipids that are removed from the bilayer environment, the number of lipids extracted does not directly quantify the formation of the lipid bridge observed in the snapshot of the C_{13} NP in Figure 2.4A. The bilayer disruption associated with this lipid bridge is expected to contribute to the free energy barrier to adsorption.

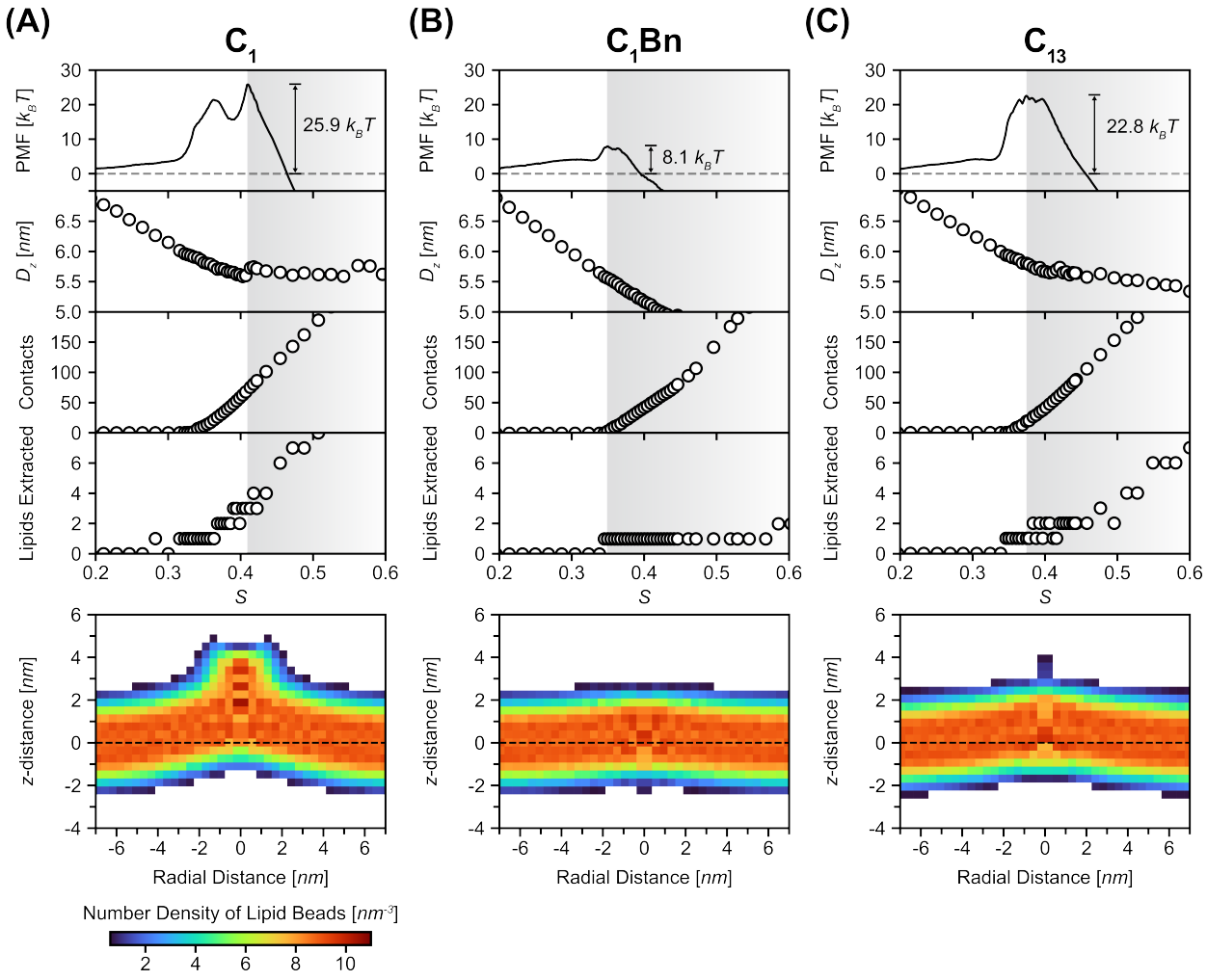


Figure 2.6: Values of the PMF, the distance between the NP and the bilayer (D_z), the number of contacts formed between the NP and the bilayer, and the number of extracted lipids along the MFEP computed for the (A) C_1, (B) C_1Bn, and (C) C_{13} NPs. The shaded regions indicate values of S greater than the value that corresponds to the free energy barrier of adsorption. The plots at the bottom show histograms of the time-averaged number density of all lipid beads as a function of the z-component of the distance from the bilayer center (z-distance) and the distance from the center of the NP in the xy plane (radial distance). Histograms were generated from the same trajectories used to generate the snapshots in Figure 2.4A, which correspond to the maximum values of the PMFs for these NPs. Histogram bins were 0.375 nm in the radial direction and 0.375 nm in the z-direction. Densities for positive and negative radial distances are equivalent; negative distances are included for visualization purposes only. The bilayer center was computed as the center of mass of the phosphate group for lipids farther than 5 nm radially from the center of the NP.

To more clearly highlight the bilayer disruption associated with the lipid bridge, Figure 2.6 shows the time-averaged number density of lipid beads from the umbrella sampling window corresponding to the maximum value of the PMF (*i.e.*, the same trajectory from which the snapshots in Figure 2.4A were obtained). These plots support the observation that the C_1 and C_{13} NPs induce substantial bilayer deformations (visible from the high density of lipid beads at z-distances greater than 2 nm from the bilayer center) associated with high free energy barriers, whereas the bilayer is essentially unperturbed upon intercalation of the C_1Bn ligands. These NPs are also unable to move closer to the bilayer due to these lipid deformations, explaining the plateaus in D_z observed at higher values of S. The deformation for the C_{13} NP is less pronounced than for the C_1 NP and consequently has a smaller free energy barrier. These densities explain the origin of the larger barrier for the C_{13} NP in comparison to the C_1Bn NP.

2.3.5 Ligand-Specific Adsorption Mechanisms

Based on our observations, we propose three different mechanisms that modulate NP adsorption to the upper leaflet of the bilayer in Figure 2.7: lipid protrusions, ligand intercalation, and lipid protrusions with ligand backfolding. The lipid protrusions mechanism refers to the extension of lipid tail groups out of the bilayer and into the hydrophobic core of the NP to initiate irreversible adsorption. Lipid protrusions were observed for the C_4SO_3 and C_1 NPs and led to large free energy barriers of adsorption because such protrusions are energetically unfavorable,[51, 92] manifesting as minimal irreversible adsorption for similar NPs in experiments.[63] Ligand intercalation refers to the extension of sufficiently long and lipophilic ligand R groups into the hydrophobic core of the lipid bilayer to promote hydrophobic contact with lipid tail groups. The intercalation mechanism led to the lowest free energy barriers of adsorption for the C_5, C_1Bn, and C_9 NPs, which were again observed experimentally to

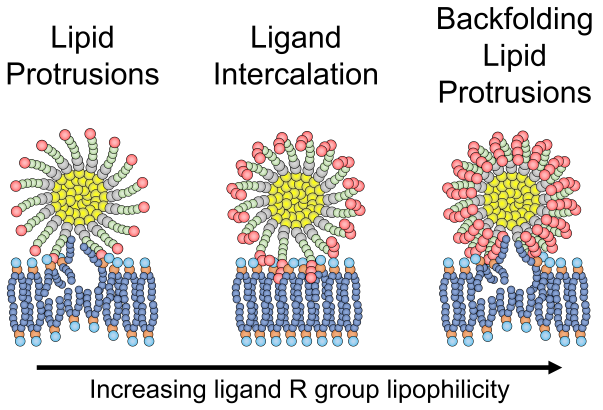


Figure 2.7: Schematic illustrations of the three mechanisms that determine the free energy of adsorption and how they depend upon ligand R group properties.

adsorb to the greatest extent.[63] Further increasing the length of the ligand R group to C_{13} and C_{17} unexpectedly led to lipid protrusion behavior with free energy barriers of adsorption comparable to those of C_4SO_3 and C_1. To explain this result, we identified ligand backfolding as a mechanism that competes against ligand intercalation because the preferential partitioning of sufficiently long ligand R groups within the ligand monolayer inhibits contact with the bilayer, requiring lipid protrusions to initiate hydrophobic contact. Ligand backfolding thus leads to the nonmonotonic behavior in the adsorption free energy barrier with R group lipophilicity, as shown in Figure 2.4A.

2.4 Conclusions

In this work, we performed CG simulations to investigate the adsorption of seven different small (2 nm in diameter) ligand-functionalized, cationic gold NPs to single-component lipid bilayers. For similar NPs, prior experimental QCM-D measurements revealed that NP adsorption increased with increasing ligand R group lipophilicity and was reversible for NPs with short aliphatic R groups but (quasi)-irreversible for NPs with more lipophilic R groups (longer aliphatic groups or a benzyl group).[63] To understand mechanisms dictating these results, we performed CG simulations with metadynamics to determine the free energy landscape for NP adsorption as a function of two collective variables: the distance of the NP from the membrane and the number of NP-lipid contacts. The free energy landscape (Figure 2.2) reveals free energy changes associated with NP adsorption and desorption from the bilayer, with adsorption being stabilized by the extraction of lipids from the bilayer and into the corona of the NP. Biasing two collective variables is necessary to resolve distinct adsorption (without extraction) and desorption (after extraction) regions of the free energy landscape. We further computed minimum free energy paths for adsorption and corresponding PMFs (Figure 2.3) to resolve adsorption free energies and free energy barriers for all seven NPs. All NPs exhibit highly favorable adsorption free energies consistent with irreversible adsorption. However, the adsorption free energy barrier depends upon ligand lipophilicity, indicating that experimentally observed differences in adsorption are a kinetic phenomenon. In particular, we find that the C_5, C_1Bn, and C_9 NPs have the lowest adsorption free energy barriers, which is consistent with experimental observations that similar NPs exhibit the most irreversible adsorption.[63] Surprisingly, however, increasing ligand lipophilicity further for the C_{13} and C_{17} increases the free energy for adsorption. We explain this nonmonotonic dependence of the adsorption free energy on ligand lipophilicity based on the three mechanisms proposed in Figure 2.7. Short, less lipophilic ligand R groups lead to NP adsorption through unfavorable lipid protrusions, ligand R groups of medium length and lipophilicity modulate adsorption through favorable ligand intercalation, and NPs with long, highly lipophilic ligand R groups adsorb through unfavorable lipid protrusions due to backfolding mechanisms that prevent R

group intercalation into the bilayer.

Together, these results suggest design considerations for nanomaterials and related soft materials that interact with lipid membranes. The finding of a nonmonotonic dependence of the free energy barrier of adsorption on R group lipophilicity due to backfolding highlights that simple descriptors of ligand R group properties are insufficient to capture the complex interplay of interactions at the nano-bio interface. A similar backfolding mechanism has also been shown by simulations to influence NP-protein interactions,[35] suggesting that this counterintuitive behavior generally influences nano-bio interactions. Simulation-derived descriptors, such as the NP-lipid contacts calculated here, may be better suited to capture the interactions between system components and used to guide NP design.[25] The results also suggest opportunities for separately tuning properties of the hydrophobic component of the ligand backbone (to modulate the free energy for irreversible adsorption) and the ligand R groups (to modulate the free energy barrier for adsorption). While here we investigated a limited set of R groups, future work will consider how a broader range of R group chemistries and structure, in combination with variations in core size, impact adsorption. We note that dozens of ligands with the modular chemical structure in Figure 2.1A have been synthesized previously, leading to a large feasible design space encompassing variations in R group length, bulkiness, lipophilicity, and charge.[17, 22, 80, 93]

The molecular mechanisms and thermodynamics for adsorption explored in this work reflect interactions with single-component, zwitterionic lipid bilayers, which are commonly used as model cell membranes.[46–48] Biological membranes can contain numerous lipid components as well as distinct domains (*e.g.*, lipid rafts), which may influence NP-membrane interactions.[30, 55, 56] We expect the ligand-mediated adsorption mechanisms described in this work to generalize to adsorption on multicomponent membranes because they emerge from the ability of ligands to intercalate into the hydrophobic core of the bilayer or from ligand-ligand interactions, both factors that should be largely independent of membrane composition. Nonetheless, in future work we will study ligand-specific variations in NP adsorption to multicomponent lipid bilayers with components that influence the surface charge density (*e.g.*, anionic lipids) or fluidity (*e.g.*, cholesterol). Probing the mechanisms and thermodynamics of NP adsorption to such biomimetic multicomponent bilayers will provide valuable insight into developing these synthetic nanomaterials for applications in biotechnology and targeted drug delivery.

Finally, the definitions of the collective variables used in this work are appropriate for studying adsorption of a NP to one leaflet of the bilayer but are not intended to bias the observation of rare events related to the translocation of charged ligand R groups across the bilayer.[51–53, 94] Nonetheless, visual inspection of the umbrella sampling windows

corresponding to S values near the second energetic barriers for some of the NPs revealed strong bilayer disruption. In the case of the strongly lipophilic NPs, at least one linear alkyl ligand translocated across the bilayer to the lower leaflet (Figure S34). Such processes may lead to the further insertion of the NP into the bilayer core and could be associated with biophysical processes such as nondisruptive cellular internalization.[49] Future work will thus extend the computational methodology developed here to also consider translocation processes to explore effects of ligand R groups on a wider variety of membrane interactions.

References

[1] X. Huang, P. K. Jain, I. H. El-Sayed, M. A. El-Sayed, "Gold Nanoparticles: Interesting Optical Properties and Recent Applications in Cancer Diagnostics and Therapy", *Nanomedicine-UK* **2007**, *2*, 681.

[2] X. Gao, Y. Cui, R. M. Levenson, L. W. K. Chung, S. Nie, "In Vivo Cancer Targeting and Imaging with Semiconductor Quantum Dots", *Nat. Biotechnol.* **2004**, *22*, 969.

[3] P. Ghosh, G. Han, M. De, C. K. Kim, V. M. Rotello, "Gold Nanoparticles in Delivery Applications", *Adv. Drug Deliv Rev.* **2008**, *60*, 1307.

[4] T. Sun, Y. S. Zhang, B. Pang, D. C. Hyun, M. Yang, Y. Xia, "Engineered Nanoparticles for Drug Delivery in Cancer Therapy", *Angew. Chem. Int. Ed.* **2014**, *53*, 12320.

[5] D. P. O'Neal, L. R. Hirsch, N. J. Halas, J. D. Payne, J. L. West, "Photo-Thermal Tumor Ablation in Mice Using near Infrared-Absorbing Nanoparticles", *Cancer Lett.* **2004**, *209*, 171.

[6] R. Mout, D. F. Moyano, S. Rana, V. M. Rotello, "Surface Functionalization of Nanoparticles for Nanomedicine", *Chem. Soc. Rev.* **2012**, *41*, 2539.

[7] D. A. Giljohann, D. S. Seferos, W. L. Daniel, M. D. Massich, P. C. Patel, C. A. Mirkin, "Gold Nanoparticles for Biology and Medicine", *Angew. Chem. Int. Ed.* **2010**, *49*, 3280.

[8] A. M. Alkilany, S. E. Lohse, C. J. Murphy, "The Gold Standard: Gold Nanoparticle Libraries to Understand the Nano-Bio Interface", *Acc. Chem. Res.* **2013**, *46*, 650.

[9] A. Verma, F. Stellacci, "Effect of Surface Properties on Nanoparticle–Cell Interactions", *Small* **2010**, *6*, 12.

[10] Z. R. Goddard, M. J. Marín, D. A. Russell, M. Searcey, "Active Targeting of Gold Nanoparticles as Cancer Therapeutics", *Chem. Soc. Rev.* **2020**, *49*, 8774.

[11] R. Huang, D. C. Luther, X. Zhang, A. Gupta, S. A. Tufts, V. M. Rotello, "Engineering the Interface between Inorganic Nanoparticles and Biological Systems through Ligand Design", *Nanomaterials* **2021**, *11*, 1001.

[12] H. Heinz, C. Pramanik, O. Heinz, Y. Ding, R. K. Mishra, D. Marchon, R. J. Flatt, I. Estrela-Lopis, J. Llop, S. Moya, R. F. Ziolo, "Nanoparticle Decoration with Surfactants: Molecular Interactions, Assembly, and Applications", *Surf. Sci. Rep* **2017**, *72*, 1.

[13] J. C. Love, L. A. Estroff, J. K. Kriebel, R. G. Nuzzo, G. M. Whitesides, "Self-Assembled Monolayers of Thiolates on Metals as a Form of Nanotechnology", *Chem. Rev.* **2005**, *105*, 1103.

[14] R. Hong, N. O. Fischer, A. Verma, C. M. Goodman, T. Emrick, V. M. Rotello, "Control of Protein Structure and Function through Surface Recognition by Tailored Nanoparticle Scaffolds", *J. Am. Chem. Soc.* **2004**, *126*, 739.

[15] P. Pengo, M. Şologan, L. Pasquato, F. Guida, S. Pacor, A. Tossi, F. Stellacci, D. Marson, S. Boccardo, S. Pricl, P. Posocco, "Gold Nanoparticles with Patterned Surface Monolayers for Nanomedicine: Current Perspectives", *Eur. Biophys. J.* **2017**, *46*, 749.

[16] X. Bai, S. Wang, X. Yan, H. Zhou, J. Zhan, S. Liu, V. K. Sharma, G. Jiang, H. Zhu, B. Yan, "Regulation of Cell Uptake and Cytotoxicity by Nanoparticle Core under the Controlled Shape, Size, and Surface Chemistries", *ACS Nano* **2020**, *14*, 289.

[17] Y. Jiang, S. Huo, T. Mizuhara, R. Das, Y. W. Lee, S. Hou, D. F. Moyano, B. Duncan, X. J. Liang, V. M. Rotello, "The Interplay of Size and Surface Functionality on the Cellular Uptake of Sub-10 Nm Gold Nanoparticles", *ACS Nano* **2015**, *9*, 9986.

[18] C. M. Goodman, C. D. McCusker, T. Yilmaz, V. M. Rotello, "Toxicity of Gold Nanoparticles Functionalized with Cationic and Anionic Side Chains", *Bioconjug Chem.* **2004**, *15*, 897.

[19] C. Carnovale, G. Bryant, R. Shukla, V. Bansal, "Identifying Trends in Gold Nanoparticle Toxicity and Uptake: Size, Shape, Capping Ligand, and Biological Corona", *ACS Omega* **2019**, *4*, 242.

[20] X. Li, S. M. Robinson, A. Gupta, K. Saha, Z. Jiang, D. F. Moyano, A. Sahar, M. A. Riley, V. M. Rotello, "Functional Gold Nanoparticles as Potent Antimicrobial Agents against Multi-Drug-Resistant Bacteria", *ACS Nano* **2014**, *8*, 10682.

[21] K. Zheng, M. I. Setyawati, D. T. Leong, J. Xie, "Surface Ligand Chemistry of Gold Nanoclusters Determines Their Antimicrobial Ability", *Chem. Mater.* **2018**, *30*, 2800.

[22] D. F. Moyano, Y. Liu, D. Peer, V. M. Rotello, "Modulation of Immune Response Using Engineered Nanoparticle Surfaces", *Small* **2016**, *12*, 76.

[23] L. A. Dykman, N. G. Khlebtsov, "Immunological Properties of Gold Nanoparticles", *Chem. Sci.* **2017**, *8*, 1719.

[24] W. Wang, A. Sedykh, H. Sun, L. Zhao, D. P. Russo, H. Zhou, B. Yan, H. Zhu, "Predicting Nano-Bio Interactions by Integrating Nanoparticle Libraries and Quantitative Nanostructure Activity Relationship Modeling", *ACS Nano* **2017**, *11*, 12641.

[25] A. K. Chew, J. A. Pedersen, R. C. Van Lehn, "Predicting the Physicochemical Properties and Biological Activities of Monolayer-Protected Gold Nanoparticles Using Simulation-Derived Descriptors", *ACS Nano* **2022**, *16*, 6282.

[26] A. Bigdeli, M. R. Hormozi-Nezhad, H. Parastar, "Using Nano-QSAR to Determine the Most Responsible Factor(s) in Gold Nanoparticle Exocytosis", *RSC Adv.* **2015**, *5*, 57030.

[27] X. Yan, A. Sedykh, W. Wang, B. Yan, H. Zhu, "Construction of a Web-Based Nanomaterial Database by Big Data Curation and Modeling Friendly Nanostructure Annotations", *Nat. Commun.* **2020**, *11*, 1.

[28] Y. Oh, Q. Cui, "Non-Equilibrium Transport of Nanoparticles across the Lipid Membrane", *Nanoscale* **2023**, *15*, 12307.

[29] R. Kariuki, R. Penman, S. J. Bryant, R. Orrell-Trigg, N. Meftahi, R. J. Crawford, C. F. McConville, G. Bryant, K. Voïtchovsky, C. E. Conn, A. J. Christofferson, A. Elbourne, "Behavior of Citrate-Capped Ultrasmall Gold Nanoparticles on a Supported Lipid Bilayer Interface at Atomic Resolution", *ACS Nano* **2022**, *16*, 17179.

[30] T. Pfeiffer, A. De Nicola, C. Montis, F. Carlà, N. F. A. Van Der Vegt, D. Berti, G. Milano, "Nanoparticles at Biomimetic Interfaces: Combined Experimental and Simulation Study on Charged Gold Nanoparticles/Lipid Bilayer Interfaces", *J. Phys. Chem. Lett.* **2019**, *10*, 129.

[31] I. U. Foreman-Ortiz, D. Liang, E. D. Laudadio, J. D. Calderin, M. Wu, P. Keshri, X. Zhang, M. P. Schwartz, R. J. Hamers, V. M. Rotello, C. J. Murphy, Q. Cui, J. A. Pedersen, "Anionic Nanoparticle-Induced Perturbation to Phospholipid Membranes Affects Ion Channel Function", *Proc. Natl. Acad. Sci. U. S. A.* **2020**, *117*, 27854.

[32] A. K. Chew, B. C. Dallin, R. C. Van Lehn, "The Interplay of Ligand Properties and Core Size Dictates the Hydrophobicity of Monolayer-Protected Gold Nanoparticles", *ACS Nano* **2021**, *15*, 4534.

[33] A. K. Chew, R. C. Van Lehn, "Effect of Core Morphology on the Structural Asymmetry of Alkanethiol Monolayer-Protected Gold Nanoparticles", *J. Phys. Chem. C* **2018**, *122*, 26288.

[34] S. E. Hoff, D. Di Silvio, R. F. Ziolo, S. E. Moya, H. Heinz, "Patterning of Self-Assembled Monolayers of Amphiphilic Multisegment Ligands on Nanoparticles and Design Parameters for Protein Interactions", *ACS Nano* **2022**, *16*, 8766.

[35] F. Simonelli, G. Rossi, L. Monticelli, "Role of Ligand Conformation on Nanoparticle-Protein Interactions", *J. Phys. Chem. B* **2019**, *123*, 1764.

[36] D. Liang, U. Dahal, M. Wu, C. J. Murphy, Q. Cui, "Ligand Length and Surface Curvature Modulate Nanoparticle Surface Heterogeneity and Electrostatics", *J. Phys. Chem. C* **2020**, *124*, 24513.

[37] G. Chong, I. U. Foreman-Ortiz, M. Wu, A. Bautista, C. J. Murphy, J. A. Pedersen, R. Hernandez, "Defects in Self-Assembled Monolayers on Nanoparticles Prompt Phospholipid Extraction and Bilayer-Curvature-Dependent Deformations", *J. Phys. Chem. C* **2019**, *123*, 27951.

[38] Y. Yang, H. Qin, M. Jiang, L. Lin, T. Fu, X. Dai, Z. Zhang, Y. Niu, H. Cao, Y. Jin, F. Zhao, X. Peng, "Entropic Ligands for Nanocrystals: From Unexpected Solution Properties to Outstanding Processability", *Nano Lett.* **2016**, *16*, 2133.

[39] C. Gabellini, M. Şologan, E. Pellizzoni, D. Marson, M. Daka, P. Franchi, L. Bignardi, S. Franchi, Z. Posel, A. Baraldi, P. Pengo, M. Lucarini, L. Pasquato, P. Posocco, "Spotting Local Environments in Self-Assembled Monolayer-Protected Gold Nanoparticles", *ACS Nano* **2022**, *16*, 20902.

[40] M. V. Prud, A. Kyrychenko, O. N. Kalugin, "PH-Controllable Coating of Silver Nanoparticles with PMMA- b -PDMAEMA Oligomers: A Molecular Dynamics Simulation Study", *J. Phys. Chem. C* **2023**, *127*, 11748.

[41] A. E. Nel, L. Mädler, D. Velegol, T. Xia, E. M. V. Hoek, P. Somasundaran, F. Klaessig, V. Castranova, M. Thompson, "Understanding Biophysicochemical Interactions at the Nano–Bio Interface", *Nat. Mater.* **2009**, *8*, 543.

[42] A. Albanese, P. S. Tang, W. C. W. Chan, "The Effect of Nanoparticle Size, Shape, and Surface Chemistry on Biological Systems", *Annu. Rev. Biomed Eng.* **2012**, *14*, 1.

[43] C. Xie, L. Zhang, "Design and Characterization of Antithrombotic ClEKnsTy-Au Nanoparticles as Diagnostic and Therapeutic Reagents", *Phys. Chem. Chem. Phys.* **2023**, *25*, 20422.

[44] A. Lesniak, A. Salvati, M. J. Santos-Martinez, M. W. Radomski, K. A. Dawson, C. Åberg, "Nanoparticle Adhesion to the Cell Membrane and Its Effect on Nanoparticle Uptake Efficiency", *J. Am. Chem. Soc.* **2013**, *135*, 1438.

[45] S. T. Kim, K. Saha, C. Kim, V. M. Rotello, "The Role of Surface Functionality in Determining Nanoparticle Cytotoxicity", *Acc. Chem. Res.* **2013**, *46*, 681.

[46] A. M. Farnoud, S. Nazemidashtarjandi, "Emerging Investigator Series: Interactions of Engineered Nanomaterials with the Cell Plasma Membrane; What Have We Learned from Membrane Models?", *Environ. Sci. Nano* **2019**, *6*, 13.

[47] E. Rascol, J. M. Devoisselle, J. Chopineau, "The Relevance of Membrane Models to Understand Nanoparticles–Cell Membrane Interactions", *Nanoscale* **2016**, *8*, 4780.

[48] K. L. Chen, G. D. Bothun, "Nanoparticles Meet Cell Membranes: Probing Nonspecific Interactions Using Model Membranes", *Environ. Sci. Technol.* **2014**, *48*, 873.

[49] R. C. Van Lehn, P. U. Atukorale, R. P. Carney, Y. S. Yang, F. Stellacci, D. J. Irvine, A. Alexander-Katz, "Effect of Particle Diameter and Surface Composition on the Spontaneous Fusion of Monolayer-Protected Gold Nanoparticles with Lipid Bilayers", *Nano Lett.* **2013**, *13*, 4060.

[50] F. Lolicato, L. Joly, H. Martinez-Seara, G. Fragneto, E. Scoppola, F. Baldelli Bombelli, I. Vattulainen, J. Akola, M. Maccarini, "The Role of Temperature and Lipid Charge on Intake/Uptake of Cationic Gold Nanoparticles into Lipid Bilayers", *Small* **2019**, *15*, 1805046.

[51] R. C. Van Lehn, A. Alexander-Katz, "Pathway for Insertion of Amphiphilic Nanoparticles into Defect-Free Lipid Bilayers from Atomistic Molecular Dynamics Simulations", *Soft Matter* **2015**, *11*, 3165.

[52] F. Simonelli, D. Bochicchio, R. Ferrando, G. Rossi, "Monolayer-Protected Anionic Au Nanoparticles Walk into Lipid Membranes Step by Step", *J. Phys. Chem. Lett.* **2015**, *6*, 3175.

[53] S. Salassi, F. Simonelli, D. Bochicchio, R. Ferrando, G. Rossi, "Au Nanoparticles in Lipid Bilayers: A Comparison between Atomistic and Coarse-Grained Models", *J. Phys. Chem. C* **2017**, *121*, 10927.

[54] L. Sun, Y. Cao, X. Chen, Q. Liang, "Interactions between Amphiphilic Nanoparticles Coated with Striped Hydrophilic/Hydrophobic Ligands and a Lipid Bilayer", *Commun. Theor. Phys.* **2023**, *75*, 065601.

[55] J. K. Sheavly, J. A. Pedersen, R. C. Van Lehn, "Curvature-Driven Adsorption of Cationic Nanoparticles to Phase Boundaries in Multicomponent Lipid Bilayers", *Nanoscale* **2019**, *11*, 2767.

[56] X. Lin, X. Lin, "Surface Ligand Rigidity Modulates Lipid Raft Affinity of Ultra-Small Hydrophobic Nanoparticles: Insights from Molecular Dynamics Simulations", *Nanoscale* **2021**, *13*, 9825.

[57] X. Chen, D. P. Tieleman, Q. Liang, "Modulating Interactions between Ligand-Coated Nanoparticles and Phase-Separated Lipid Bilayers by Varying the Ligand Density and the Surface Charge", *Nanoscale* **2018**, *10*, 2481.

[58] J. K. Sheavly, R. C. Van Lehn, "Bilayer-Mediated Assembly of Cationic Nanoparticles Adsorbed to Lipid Bilayers: Insights from Molecular Simulations", *AIChE J.* **2020**, *66*, e16993.

[59] M. Das, U. Dahal, O. Mesele, D. Liang, Q. Cui, "Molecular Dynamics Simulation of Interaction between Functionalized Nanoparticles with Lipid Membranes: Analysis of Coarse-Grained Models", *J. Phys. Chem. B* **2019**, *123*, 10547.

[60] Z. Shen, W. Baker, H. Ye, Y. Li, "PH-Dependent Aggregation and PH-Independent Cell Membrane Adhesion of Monolayer-Protected Mixed Charged Gold Nanoparticles", *Nanoscale* **2019**, *11*, 7371.

[61] T. Lunnoo, J. Assawakhajornsak, S. Ruangchai, T. Puangmali, "Role of Surface Functionalization on Cellular Uptake of AuNPs Characterized by Computational Microscopy", *J. Phys. Chem. B* **2020**, *124*, 1898.

[62] X. Quan, D. Zhao, L. Li, J. Zhou, "Understanding the Cellular Uptake of PH-Responsive Zwitterionic Gold Nanoparticles: A Computer Simulation Study", *Langmuir* **2017**, *33*, 14480.

[63] C. A. Lochbaum, A. K. Chew, X. Zhang, V. Rotello, R. C. Van Lehn, J. A. Pedersen, "Lipophilicity of Cationic Ligands Promotes Irreversible Adsorption of Nanoparticles to Lipid Bilayers", *ACS Nano* **2021**, *15*, 6562.

[64] W. Humphrey, A. Dalke, K. Schulten, "VMD: Visual Molecular Dynamics", *J. Mol. Graph* **1996**, *14*, 33.

[65] A. C. Pan, D. Sezer, B. Roux, "Finding Transition Pathways Using the String Method with Swarms of Trajectories", *J. Phys. Chem. B* **2008**, *112*, 3432.

[66] S. J. Patel, R. C. Van Lehn, "Analysis of Charged Peptide Loop-Flipping across a Lipid Bilayer Using the String Method with Swarms of Trajectories", *J. Phys. Chem. B* **2021**, *125*, 5862.

[67] L. Maragliano, B. Roux, E. Vanden-Eijnden, "Comparison between Mean Forces and Swarms-of-Trajectories String Methods", *J. Chem. Theory Comput* **2014**, *10*, 524.

[68] D. Branduardi, F. L. Gervasio, M. Parrinello, "From A to B in Free Energy Space", *J. Chem. Phys.* **2007**, *126*, 54103.

[69] D. Van Der Spoel, E. Lindahl, B. Hess, G. Groenhof, A. E. Mark, H. J. C. Berendsen, "GROMACS: Fast, Flexible, and Free", *J. Comput. Chem.* **2005**, *26*, 1701.

[70] E. Lindahl, M. Abraham, B. Hess, D. van der Spoel, *GROMACS 2021.5 Source code*, **2022**.

[71] G. A. Tribello, M. Bonomi, D. Branduardi, C. Camilloni, G. Bussi, "PLUMED 2: New Feathers for an Old Bird", *Comput. Phys. Commun.* **2014**, *185*, 604.

[72] S. J. Marrink, H. J. Risselada, S. Yefimov, D. P. Tieleman, A. H. De Vries, "The MARTINI Force Field: Coarse Grained Model for Biomolecular Simulations", *J. Phys. Chem. B* **2007**, *111*, 7812.

[73] H. M. Khan, P. C. T. Souza, S. Thallmair, J. Barnoud, A. H. De Vries, S. J. Marrink, N. Reuter, "Capturing Choline-Aromatics Cation- Interactions in the MARTINI Force Field", *J. Chem. Theory Comput* **2020**, *16*, 2550.

[74] D. H. De Jong, G. Singh, W. F. D. Bennett, C. Arnarez, T. A. Wassenaar, L. V. Schäfer, X. Periole, D. P. Tieleman, S. J. Marrink, "Improved Parameters for the Martini Coarse-Grained Protein Force Field", *J. Chem. Theory Comput* **2013**, *9*, 687.

[75] S. O. Yesylevskyy, L. V. Schäfer, D. Sengupta, S. J. Marrink, "Polarizable Water Model for the Coarse-Grained MARTINI Force Field", *PLoS Comput. Biol.* **2010**, *6*, e1000810.

[76] J. Michalowsky, L. V. Schäfer, C. Holm, J. Smiatek, "A Refined Polarizable Water Model for the Coarse-Grained MARTINI Force Field with Long-Range Electrostatic Interactions", *J. Chem. Phys.* **2017**, *146*, 54501.

[77] R. S. Davis, P. B. Sunil Kumar, M. M. Sperotto, M. Laradji, "Predictions of Phase Separation in Three-Component Lipid Membranes by the MARTINI Force Field", *J. Phys. Chem. B* **2013**, *117*, 4072.

[78] T. A. Wassenaar, H. I. Ingólfsson, R. A. Böckmann, D. P. Tieleman, S. J. Marrink, "Computational Lipidomics with Insane: A Versatile Tool for Generating Custom Membranes for Molecular Simulations", *J. Chem. Theory Comput* **2015**, *11*, 2144.

[79] F. Grunewald, G. Rossi, A. H. De Vries, S. J. Marrink, L. Monticelli, "Transferable MARTINI Model of Poly(Ethylene Oxide)", *J. Phys. Chem. B* **2018**, *122*, 7436.

[80] D. F. Moyano, K. Saha, G. Prakash, B. Yan, H. Kong, M. Yazdani, V. M. Rotello, "Fabrication of Corona-Free Nanoparticles with Tunable Hydrophobicity", *ACS Nano* **2014**, *8*, 6748.

[81] A. K. Ghose, G. M. Crippen, "Atomic Physicochemical Parameters for Three-Dimensional-Structure-Directed Quantitative Structure-Activity Relationships. 2. Modeling Dispersive and Hydrophobic Interactions", *J. Chem. Inf. Comput. Sci.* **1987**, *27*, 21.

[82] A. Laio, M. Parrinello, "Escaping Free-Energy Minima", *Proc. Natl. Acad. Sci. U. S. A.* **2002**, *99*, 12562.

[83] J. S. Hub, B. L. De Groot, D. Van Der Spoel, "G-Whams-a Free Weighted Histogram Analysis Implementation Including Robust Error and Autocorrelation Estimates", *J. Chem. Theory Comput* **2010**, *6*, 3713.

[84] J. R. Rogers, P. L. Geissler, "Breakage of Hydrophobic Contacts Limits the Rate of Passive Lipid Exchange between Membranes", *J. Phys. Chem. B* **2020**, *124*, 5884.

[85] R. C. Van Lehn, A. Alexander-Katz, "Membrane-Embedded Nanoparticles Induce Lipid Rearrangements Similar to Those Exhibited by Biological Membrane Proteins", *J. Phys. Chem. B* **2014**, *118*, 12586.

[86] P. M. Kasson, E. Lindahl, V. S. Pande, "Atomic-Resolution Simulations Predict a Transition State for Vesicle Fusion Defined by Contact of a Few Lipid Tails", *PLoS Comput. Biol.* **2010**, *6*, e1000829.

[87] G. Brosio, G. Rossi, D. Bochicchio, "Nanoparticle-Induced Biomembrane Fusion: Unraveling the Effect of Core Size on Stalk Formation", *Nanoscale Adv.* **2023**, *5*, 4675.

[88] L. L. Olenick, J. M. Troiano, A. Vartanian, E. S. Melby, A. C. Mensch, L. Zhang, J. Hong, O. Mesele, T. Qiu, J. Bozich, S. Lohse, X. Zhang, T. R. Kuech, A. Millevolte, I. Gunsolus, A. C. McGeachy, M. Doğangün, T. Li, D. Hu, S. R. Walter, A. Mohaimani, A. Schmoldt, M. D. Torelli, K. R. Hurley, J. Dalluge, G. Chong, Z. V. Feng, C. L. Haynes, R. J. Hamers, J. A. Pedersen, Q. Cui, R. Hernandez, R. Klaper, G. Orr, C. J. Murphy, F. M. Geiger, "Lipid Corona Formation from Nanoparticle Interactions with Bilayers", *Chem.* **2018**, *4*, 2709.

[89] T. Mandal, N. V. Konduru, A. Ramazani, R. M. Molina, R. G. Larson, "Effect of Surface Charge and Hydrophobicity on Phospholipid-Nanoparticle Corona Formation: A Molecular Dynamics Simulation Study", *Colloid Interface Sci. Commun.* **2018**, *25*, 7.

[90] A. Maity, S. K. De, D. Bagchi, H. Lee, A. Chakraborty, "Mechanistic Pathway of Lipid Phase-Dependent Lipid Corona Formation on Phenylalanine-Functionalized Gold Nanoparticles: A Combined Experimental and Molecular Dynamics Simulation Study", *J. Phys. Chem. B* **2022**, *126*, 2241.

[91] X. Zhang, A. K. Pandiakumar, R. J. Hamers, C. J. Murphy, "Quantification of Lipid Corona Formation on Colloidal Nanoparticles from Lipid Vesicles", *Anal. Chem.* **2018**, *90*, 14387.

[92] M. A. Tahir, R. C. Van Lehn, S. H. Choi, A. Alexander-Katz, "Solvent-Exposed Lipid Tail Protrusions Depend on Lipid Membrane Composition and Curvature", *Biochimica et Biophysica Acta (BBA) - Biomembranes* **2016**, *1858*, 1207.

[93] K. Saha, D. F. Moyano, V. M. Rotello, "Protein Coronas Suppress the Hemolytic Activity of Hydrophilic and Hydrophobic Nanoparticles", *Mater. Horiz* **2014**, *1*, 102.

[94] R. C. Van Lehn, A. Alexander-Katz, "Energy Landscape for the Insertion of Amphiphilic Nanoparticles into Lipid Membranes: A Computational Study", *PLoS One* **2019**, *14*, e0209492.

Chapter 3

Influence of branched ligand architectures on nanoparticle interactions with lipid bilayers[1]

3.1 Introduction

Surface-functionalized nanoparticles (NPs) have become a valuable tool for biomedical applications.[1–3] These materials possess highly tunable physicochemical properties that make them versatile materials for applications such as antibacterial treatments,[4] therapeutics,[5] diagnostics,[5] disease prevention,[6] photothermal therapy,[7] and drug delivery.[8] In these applications, the interactions of NPs with cellular membranes are critical in determining their efficacy and safety, motivating interest in design criteria that impact NP-membrane interactions. For example, experimental studies have shown that tuning NP size, shape, and surface chemistry can significantly influence nano–bio interactions such as cellular entry.[9–11] Recent advances have been made to increase cellular uptake, in particular, by functionalizing NP surfaces with organic ligands that can modulate their interactions with the cell membrane.[12, 13] However, the nano–bio interactions that drive cellular entry can also lead to adverse behaviors such as cytotoxicity and hemolysis, hindering the utility of these nanomaterials for biomedical applications and inhibiting clinical translation.[14, 15] These challenges have motivated efforts to design NPs that can enter cells with minimal cytotoxicity.[9, 12] Although parametric studies have shown that cellular internalization is dependent on NP core material,[10, 11] size,[9, 16, 17] shape,[16, 18] surface charge,[9, 11, 19] and ligand lipophilicity10 (log P), pathways and mechanisms for cellular entry remain under active study.

[1]This chapter is adapted with permission from Huang-Zhu and Van Lehn, *Nanoscale*, 17:1659-1672, 2025. Copyright 2025 Royal Society of Chemistry. Electronic Supplementary Information (ESI) referenced is available at DOI:`https://doi.org/10.1039/D4NR03848G`.

Within the large design space of nanomaterials, gold nanoparticles (AuNPs) coated with a self-assembled monolayer of amphiphilic ligands have been shown to exhibit high cellular uptake, biocompatibility, and versatility.[9, 20, 21] These amphiphilic ligands possess tunable lipophilic and charged groups that interact with lipid tails and head groups, respectively, making ligand-functionalized AuNPs promising biomedical agents and excellent platform materials to elucidate nano–bio interactions.[22–24] However, the design space of potential ligand structures – even when restricted to amphiphilic ligands – remains challenging to explore experimentally due to the expense and time associated with AuNP synthesis and in vitro cellular entry assays. Consequently, methods are needed to predict interactions between ligand-functionalized AuNPs and biological membranes prior to synthesis.

As a step toward predicting ligand-mediated nano–bio interactions, Rotello and coworkers have identified log P as a ligand-specific descriptor that can be easily evaluated prior to synthesis and correlates with AuNP interactions.[12, 13, 15, 25, 26] Ligand log P is a measure of lipophilicity that describes how strongly (or weakly) the ligands favor the hydrophobic core of lipid bilayers; larger values of log P indicate a stronger preference for partitioning into hydrophobic environments. For example, AuNPs coated with zwitterionic ligands were shown to generally exhibit higher cellular uptake for ligands with higher log P in the absence of serum proteins.[12] The same set of AuNPs, however, showed a nonmonotonic trend in the presence of serum proteins, where the least and most lipophilic ligands showed the highest uptake.[12] More defined nonmonotonic trends have also been observed for cationic ligands with uncharged alkyl moieties as end groups.[13] However, ligand-functionalized AuNPs with end groups composed of alcohols, cyclic structures, or branches exhibit weaker correlations between cellular uptake and log P.[13, 15, 26, 27] In general, these studies have demonstrated that ligand log P can describe nano–bio interactions to some extent, but there are still outliers that are yet to be explained, such as ligands with branched alkyl end groups.[13, 15, 26] Additionally, the lack of mechanistic insight further minimizes the feasibility of exclusively relating log P to nano–bio interactions a priori.

To better understand how physicochemical properties of ligands modulate nano–bio interactions, computational modeling has been employed to predict NP surface properties from the interplay of interactions between self-assembled ligands,[28, 29] and to elucidate thermodynamic and mechanistic insight on NP-bilayer interactions.[30–51] Recent work in our group has focused on studying the relationship between log P and the quasi-irreversible adsorption of AuNPs coated with a cationic ligand monolayer to zwitterionic lipid bilayers.[30, 31] This cationic ligand is composed of (1) a 1-undecanethiol hydrophobic backbone, (2) a tetraethylene glycol (PEG) chain for biocompatibility, and (3) a cationic quaternary ammonium (TTMA) with a tunable R group that modulates nano–bio interactions. The

tunable R group is of great importance as it has been shown by the Rotello group that its lipophilicity (*i.e.*, log P) can regulate cellular uptake, cytotoxicity, hemolysis, and protein corona formation.[1, 8, 12, 13, 21] We performed coarse-grained (CG) molecular dynamics simulations to study the adsorption of AuNPs to zwitterionic lipid bilayers for a series of AuNPs with ligands of varying log P.[30] We demonstrated that combining the distance between the AuNP and bilayer and the number of contacts between ligands and lipids provides an appropriate reaction coordinate to describe AuNP adsorption. We further found that ligand R group log P is nonmonotonically related to the free energy barrier for adsorption by dictating whether adsorption occurs through ligands favorably intercalating into the lipid bilayer or lipid tails unfavorably protruding out of the bilayer. These results indicate that single-ligand descriptors, such as log P, can lead to incomplete predictions of NP-membrane interactions. However, this past study, as well as related literature on nano–bio interactions,[31, 35–37, 52–57] has focused on ligands with linear architectures, neglecting more complex chain architectures that may lead to significantly different nano–bio interactions.

In this work, we sought to explore the hypothesis that chain architecture will affect AuNP adsorption for ligands with similar values of log P by perturbing the interplay of ligand–ligand and ligand–lipid interactions that was found to determine adsorption thermodynamics and mechanisms in our past work.30 To do so, we expanded the library of AuNPs studied in past work[30] by systematically designing four pairs of AuNPs coated with ligands of similar log P but different chain architecture (*i.e.*, alkyl R group branching) as shown in Figure 3.1. All ligand architectures are based on the same structure developed by Rotello and coworkers to ensure experimental relevance.[13, 15] Three pairs consist of a linear and either a double-branched or triple-branched R group, while the most lipophilic pair consists of a double-branched and a triple-branched R group. Throughout the rest of this manuscript, we will refer to the linear 11-carbon (11-C), 15-carbon (15-C), 19-carbon (19-C), and double-branched 27-carbon (27-C) as the lower-branched R groups, while the double-branched 11-C, triple-branched 15-C, double-branched 19-C, and triple-branched 27-C will be referred to as the higher-branched R groups. We employed CG simulations using the string method with swarms of trajectories[30, 58–60] and path variables[30, 61] to simulate the adsorption of a single AuNP to a zwitterionic 1,2-dilinoleoyl-sn-glycero-3-phosphocoline (DIPC) bilayer – which is a CG representation of the more common 1,2-dioleoyl-sn-glycero-3-phosphocoline DOPC bilayer – as a function of the distance between the AuNP and the bilayer and the number of ligand–lipid contacts.[30] We show that similarly lipophilic ligands with different chain architectures exhibit different thermodynamics and mechanisms for adsorption to DIPC bilayers. Increasing the number of alkyl R group branches, while keeping a fixed number of hydrophobic beads (representing carbon atoms), decreases the average free energy barrier for adsorption. We attribute this behavior to increased alkyl R group protrusions that promote favorable lipophilic contacts with the lipid tails while minimizing membrane disruption (e.g.,

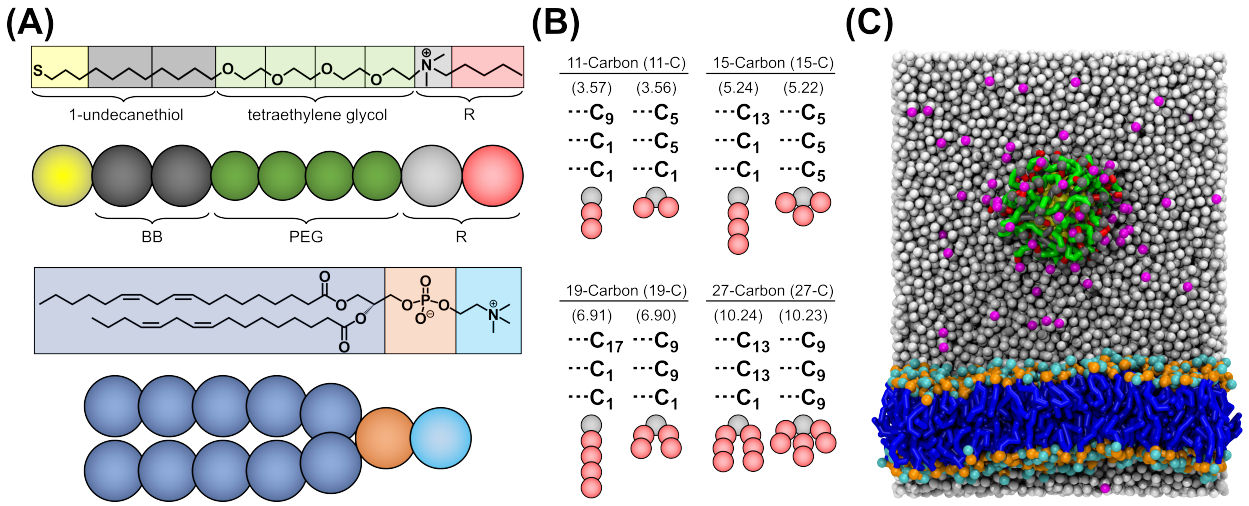


Figure 3.1: (A) Chemical structures and CG models of the cationic ligand and DIPC lipids. The R group consists of the TTMA cation (bead mapping includes only three carbon atoms) and the additional carbon atoms of the branches. (B) Library of R groups studied (labels do not include the hydrogen atoms). Log P values of the R groups are shown in parentheses and were extracted from ChemDraw version 21.0.0 using Crippen's method.[62] Log P for the 27-Carbon pair was estimated by cumulative contributions of single carbons since ChemDraw was unable to compute these values. (C) Representative snapshot of the initial configurations for the solvated AuNPs. The colors for the AuNP and the DIPC lipids follow (A); BB and TTMA are the same shade of grey, but the latter is represented as a sphere for visual purposes. Water beads are white and Cl^- counterions are magenta. Half of the water beads are not shown for clarity. All simulations snapshots were rendered using visual molecular dynamics.[63]

mechanisms associated with lipid extraction, such as lipid tails protruding out of the bilayer). We also show that increased alkyl R group branching substantially decreases adsorption free energies due to a greater decrease in surface area exposure to water that is mediated by increased exposure to the nonpolar environment of the membrane core. Both results emerge from the disruption of packing due to the branched groups. These findings reveal striking and nonintuitive behaviors for nano–bio interactions that cannot be predicted from log P alone, indicating the importance of alternative ligand design criteria when considering the molecular design and engineering of nanomaterials for biomedical applications.

3.2 Methods

3.2.1 Simulation parameters

All coarse-grained simulations were performed with GROMACS 2021.5[64] patched with PLUMED 2.8.0.[65] Interactions were described using the MARTINI force field (version 2.3P[66, 67]) with the refined polarizable water model.[68, 69] Molecular dynamics simulations were performed using a leapfrog integrator with a 20 fs timestep. The temperature was kept constant at 300 K using a velocity-rescale thermostat with a 1.0 ps time con-

stant. The pressure was kept constant at 1 bar with semi-isotropic pressure coupling and a compressibility of 3×10^{-4} bar^{-1} in both the xy and z directions. Systems were first energy-minimized using the steepest descents method for 5000 steps or until the maximum force was less than 1000 $kJ{\cdot}mol^{-1}{\cdot}nm^{-1}$. During equilibration simulations (*vide infra*), a Berendsen barostat with a coupling constant of 5.0 ps^{-1} was used. A total of 45 ns of equilibration was performed for unbiased simulations of the AuNPs solvated in water far from the bilayer. The equilibrated systems were then used as initial configurations for the calculation of the MFEPs. During production simulations, a Parrinello–Rahman barostat with a coupling constant of 12.0 ps^{-1} was used. AuNP bonds that yielded force constants greater than 15 000 $kJ{\cdot}mol^{-1}{\cdot}nm^{-2}$ during parameterization were constrained using the LINCS algorithm with an order of 4 for stability. van der Waals interactions were modeled using a Lennard-Jones interaction with the potential smoothly shifted to zero at a cutoff distance of 1.1 nm. Neighbor lists were generated using the Verlet algorithm with a cut-off of 1.1 nm. Electrostatic interactions were modeled using the smooth Particle Mesh Ewald algorithm with a short-range cut-off of 1.1 nm, a spacing of 0.12 nm for the Fourier grid, and a dielectric constant of 2.5. These interaction parameters are all consistent with MARTINI recommendations.[66–69]

3.2.2 Description of systems

Solvated zwitterionic bilayers were generated using the *insane.py* script[70] with initial system dimensions of 14 nm × 14 nm × 24 nm and contained a total of 578 DIPC lipids and 30 000 water beads (using the polarizable water model). System neutrality was achieved by adding 72 Cl^- counterions. Table S1 contains the exact number of water molecules for each system.

The AuNPs were modeled using 72 ligands, as shown in Figure 3.1, with the grafting density based on experimental data.[9] Ligands were arranged spherically to form a hollow shell with a diameter of 2 nm following our prior work.[30, 55, 56] From the 1-undecanethiol segment, the $S(CH_2)_3$ group was modeled as a C5 bead in MARTINI, while the $(CH_2)_4$ groups were modeled as C1 beads. The tetraethylene glycol groups were modeled using four ethylene oxide (EO) beads developed by Grunewald *et al.*[71] The quaternary ammonium (TTMA) group was modeled as a Q0 bead representing a choline group in which the carbons are not shared with the R groups. Although we refer to the positively charged group as a quaternary ammonium, the actual CG bead mapping consists of three carbon atoms instead of four to ensure a 4 : 1 mapping for the 1-undecanethiol and correct restructuring of branched chain architectures, which was only possible by mapping the EO bead as [O–CH_2–CH_2] instead of the original [CH_2–O–CH_2]. Each R group bead represents four carbon atoms.

Each AuNP was individually parameterized based on all-atom (AA) simulations through a bottom-up approach to capture conformational effects that arise from ligand grafting to the AuNP surface.[30] Simulations of the AuNPs at the AA scale used the CHARMM36[72] force field. Distributions of the bond lengths and angles were used to calculate the CG bonded parameters. The C5 beads that compose the hollow shell were bonded to their nearest C5 neighbors within 1.24 nm using a harmonic potential with a spring constant of 5000 $\mathrm{kJ{\cdot}mol^{-1}{\cdot}nm^{-2}}$ to obtain a stable and rigid core. Specific details regarding this bottom-up parameterization can be found in our previous work.[30]

3.2.3 Definition of collective variables

The reaction coordinate for free energy calculations was described using two CVs: $\widetilde{D}_Z$ and N_C. We defined $\widetilde{D}_Z$ as the scaled distance (with respect to the z-component of the simulation box) between the center of mass of the AuNP and the center of mass of the bilayer projected onto the z-axis normal to the membrane. The center of mass of the bilayer was computed using 20 randomly selected lipids (10 lipids from each leaflet). We chose to use the scaled distance to minimize numerical instabilities that may originate from bilayer deformations during steered MD simulations and umbrella sampling. However, we plot all data using the unscaled distance (D_Z, which has units of nm) for improved interpretability (Figure 3.2 and Fig. S2–S21, S54–S57). To calculate D_Z, we multiplied $\widetilde{D}_Z$ by either the z-component of the simulation box averaged from the final configurations of the 24 restrained windows of the last five strings, or the time-averaged z-component of the simulation box of each umbrella trajectory. For free energy calculations, a contact, N_C, was defined as one bead found within 0.47 nm of another bead (*i.e.*, any AuNP bead with respect to any lipid bead) following the standard size of MARTINI beads. The distance and coordination collective variables implemented in PLUMED 2.8.0[65] were used to compute $\widetilde{D}_Z$ and N_C, respectively.

3.2.4 String method with swarms of trajectories

We computed the minimum free energy paths (MFEPs) using the string method with swarms of trajectories.[30, 58–60] Following our previous work,[30] the initial string was defined between two equilibrium states: the AuNP in solution far from the bilayer, and the AuNP adsorbed to the upper leaflet of the bilayer, as shown in states (i) and (iii) in Figure 3.2A. Configurations for the initial string were obtained from two steered-MD simulations. During the first, $\widetilde{D}_Z$ was decreased from 0.41 to 0.16 at a rate of -0.01 $\mathrm{ns^{-1}}$ using a harmonic potential with a spring constant of 100 000 $\mathrm{kJ{\cdot}mol^{-1}}$ while N_C was retrained to 0 using a harmonic potential with a spring constant of 200 $\mathrm{kJ{\cdot}mol^{-1}{\cdot}contact^{-2}}$. The final configuration from this simulation was used to initiate the second steered-MD simulation in which N_C was

increased from 0 to 800 at a rate of 10 contacts ns^{-1} using a harmonic potential with a spring constant of 0.5 $kJ{\cdot}mol^{-1}{\cdot}contact^{-2}$ while $\widetilde{D}_Z$ was restrained to 0.16 using a harmonic potential with a spring constant of 100 000 $kJ{\cdot}mol^{-1}$.

The initial string was composed of 24 total windows: 6 windows with decreasing $\widetilde{D}_Z$ and N_C restrained to 0, and 18 windows with increasing N_C and $\widetilde{D}_Z$ restrained to 0.16.[30, 58] The evolution of the initial string was completed after 75 iterations. For all windows, each iteration began with a 0.2 ns simulation in which $\widetilde{D}_Z$ and N_C were restrained to their target values by harmonic potentials with spring constants of 100 000 $kJ{\cdot}mol^{-1}$ and 0.5 $kJ{\cdot}mol^{-1}{\cdot}contact^{-2}$, respectively. A second 0.2 ns simulation was performed with the spring constants increased to 200 000 $kJ{\cdot}mol^{-1}$ and 1 $kJ{\cdot}mol^{-1}{\cdot}contact^{-2}$. A third 0.2 ns simulation using the same restraints was performed as production from which 128 configurations were generated for each window. These 128 frames were used to initiate 24 swarms of unbiased simulations (*i.e.*, the swarms of trajectories), one per window.[30, 58] Each unbiased simulation in the swarm was performed for 0.2 ps without restraints to sample the CVs. The drift of the CVs was averaged over all trajectories for each window and added to the old CVs to evolve the string. The new string was then reparameterized to ensure equal distances between consecutive windows. The strings obtained from the last five iterations were averaged in CV space and fitted with a spline to obtain the MFEP.[30, 58] Evolutions of the strings are found in Fig. S2–S9. All converged MFEPs in CV space are found in Fig. S10–S13.

3.2.5 1D umbrella sampling

The MFEP was described using the path equations by Branduardi *et al.*[61] to define the distance along the path, S, and the normal distance away from the path, Z. The PATH collective variable implemented in PLUMED 2.8.0[65] was used to compute S and Z. The path was discretized into 72 windows equally spaced as a function of S for 1D umbrella sampling with initial configurations taken from the last five strings. Strong umbrella potentials were used for windows in which the AuNP begins generating contacts with the bilayer; these windows were slightly different across all ligands and across all replicas. Weak potentials were used for all other windows. To ensure exclusive sampling of the MFEP, an umbrella potential of 20 000 000 $kJ{\cdot}mol^{-1}$ was used to restrain Z close to 0. All values for S, Z, and their restraints are included in the ESI. All umbrella windows were simulated for 50 ns. CV values computed from the umbrella sampling trajectories were compared to the MFEP and the five strings used for the spline fit to ensure that CV sampling from both methodologies were in agreement (Fig. S14–S21). Convergence was assessed as described in the ESI (Fig. S22–S53). For ligands with linear R groups, the last 45 ns of the 50 ns simulations were used for analyses, and for ligands with branched R groups, the last 40 ns were used. Four fully independent strings and umbrella sampling calculations were performed for each

AuNP to ensure the robustness of the results. For the linear ligand architectures, two of the four replicas were taken from our past work,[30] while the other two replicas were newly simulated. The free energy as a function of S was computed using the weighted histogram analysis method (WHAM).[73]

3.3 Results and Discussion

3.3.1 Minimum free energy pathway yields reaction coordinate for potential of mean force calculation

To probe the effects of ligand R group branching on the thermodynamics for adsorption, we computed the potential of mean force (PMF) for AuNP adsorption to DIPC bilayers as a function of the distance along the minimum free energy path (MFEP), as described in our previous study.[30] The MFEP represents the most energetically favorable (*i.e.*, most probable) path for NP adsorption to the lipid bilayer. Free energy calculations along this transition pathway yield the free energy barrier that the NP must cross to initiate the adsorption process. We described the MFEP using two CVs: the center-of-mass distance between the AuNP and the bilayer projected onto the z-axis normal to the membrane (D_Z; note that this is computed using a scaled value, $\widetilde{D}_Z$, as discussed in the Methods), and the number of ligand–lipid contacts (N_C). To compute the MFEP, we solvated a single AuNP near a bilayer (representative snapshot shown in Figure 3.1C) and used the string method with swarms of trajectories[30],[58–60] to iteratively evolve an initial string toward the MFEP. A spline fit of the last five converged strings was defined as the MFEP using path variables[30, 61] and was discretized for umbrella sampling as a function of the distance of the path (S). Additional details are provided in the Methods section and a schematic of this workflow is shown in Fig. S1.

We computed four estimates of the MFEP from separate replicas (Fig. S2–S13) to relate states along the reaction coordinate with the thermodynamics and mechanisms of AuNP adsorption. To illustrate these calculations, Figure 3.2A shows a schematic of representative states sampled as the CVs change along the MFEP in addition to MFEPs computed for one replica of the 15-C ligand pair with representative simulation snapshots. All MFEPs are included in the ESI (Fig. S2–S13). The normalized distance along the MFEP (S) is represented by the color map in Figure 3.2B and C. For both linear (Figure 3.2B) and branched (Figure 3.2C) ligands, the number of ligand–lipid contacts, N_C, is zero when the AuNP is far from the bilayer (large D_Z), as illustrated in state (i) in Figure 3.2A. This state corresponds to small values of S. Following the MFEP (increasing S) leads to a decrease in D_Z and, as the AuNP approaches the bilayer, an increase in N_C, as represented in state (ii) in Figure 3.2A. Qualitatively, MFEPs for the linear and branched ligands show

distinct differences during the initial interaction with the bilayer associated with state (ii). As observed by comparing Figure 3.2B and C, the MFEP for the linear ligand shows a steep increase in N_C at approximately $D_Z = 5.60$ nm whereas the branched ligand instead shows a gradual increase at approximately $D_Z = 6.10$ nm. This trend is consistently observed for linear and branched ligand R groups, indicating distinct mechanisms of adsorption, and is further discussed below. Fig. S14–S21 show these regions of interest zoomed-in for clarity. The initial increase in N_C between ligands and lipids associated with this region leads into the transition state where the AuNP must overcome an energetic barrier (further discussed below) to initiate adsorption that is dependent on the ligand alkyl R group and its interaction with the bilayer as observed from the simulation snapshots in Figure 3.2B and C. Following

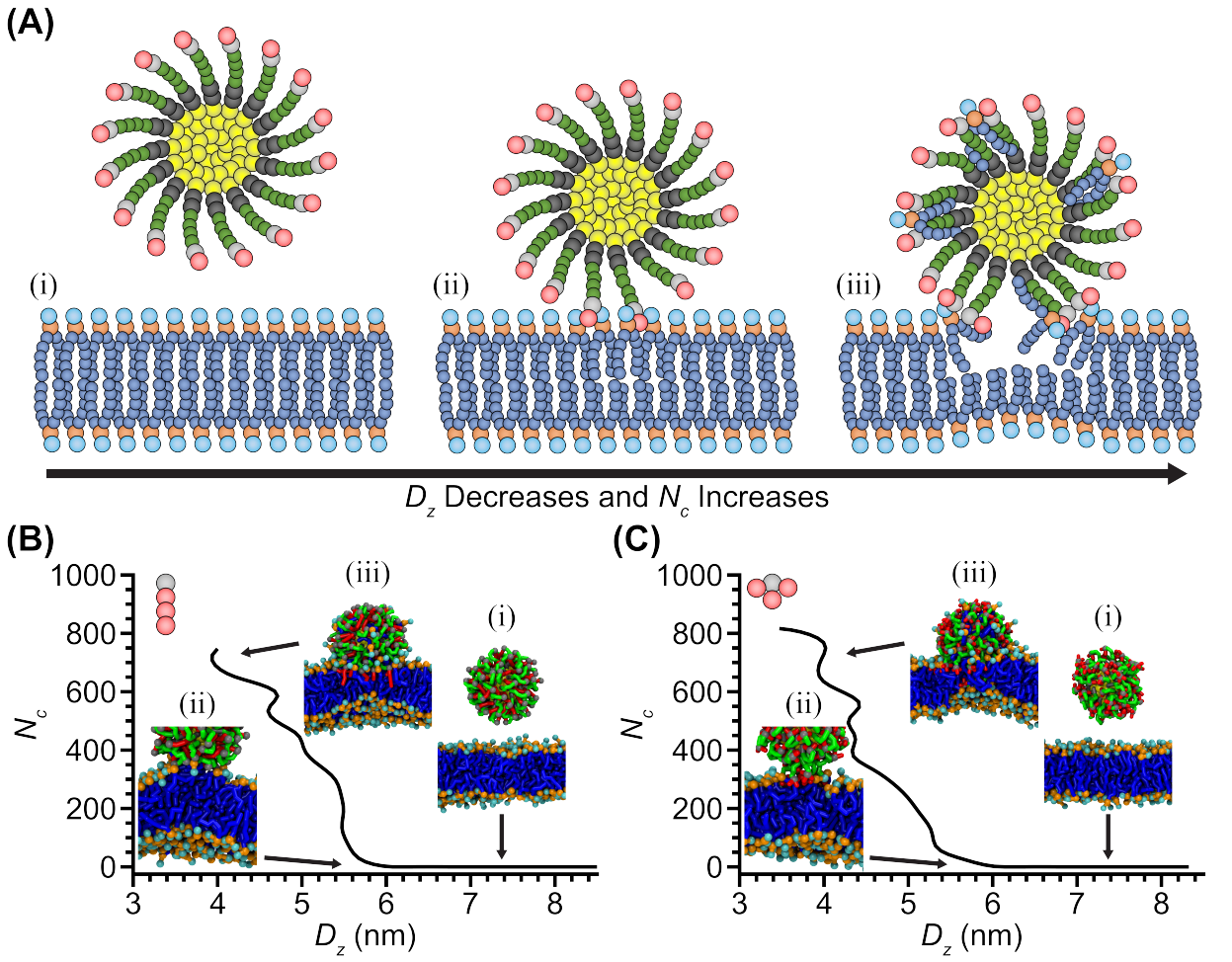


Figure 3.2: (A) Schematic of AuNP adsorption to lipid bilayers described in CV space. States (i) to (iii) schematically indicate key states in the MFEPs and correspond to the similarly labeled simulation snapshots. (B) MFEP for one replica of the linear 15-C ligand alkyl R group. (C) MFEP for one replica of the triple-branched 15-C ligand alkyl R group. The color map for the MFEPs corresponds to the normalized distance along the path (S). Representative simulation snapshots were taken from the last five strings that were used to fit the spline. All water beads, counterions, and lipids in the bilayer that are in front of the AuNP were removed for visual purposes. Colors follow Figure 3.1.

the transition state, increasing S toward values close to 1 leads to a decrease in D_Z with an increase in N_C that corresponds to NP adsorption and lipid extraction from the bilayer, as depicted in state (iii) in Figure 3.2A.

Next, we computed the PMF as a function of S. Since each MFEP differs in CV space from one another, S was normalized by its largest value for each replica to ensure $0 \leq S \leq 1$ in all cases. We defined the free energy barrier for adsorption as the largest PMF difference between the first maximum and the first minimum (PMF Max.), and the adsorption free energy as the global free energy minimum (PMF Min.). The PMFs in Figure 3.3 show that all AuNPs exhibit well-defined free energy barriers at $0.25 \leq S \leq 0.45$, ranging from 10.5 k_BT to 22.8 k_BT (13.0 k_BT to 21.4 k_BT when averaged across replicas, depending on the ligand R group). Furthermore, all AuNPs show strong irreversible adsorption with free energies of adsorption between -175.3 k_BT and -20.6 k_BT (-161.6 k_BT to -30.3 k_BT when averaged across replicas, depending upon the ligand R group). We discuss in detail the free energy barriers for adsorption and the adsorption free energies in the following sections. Qualitative

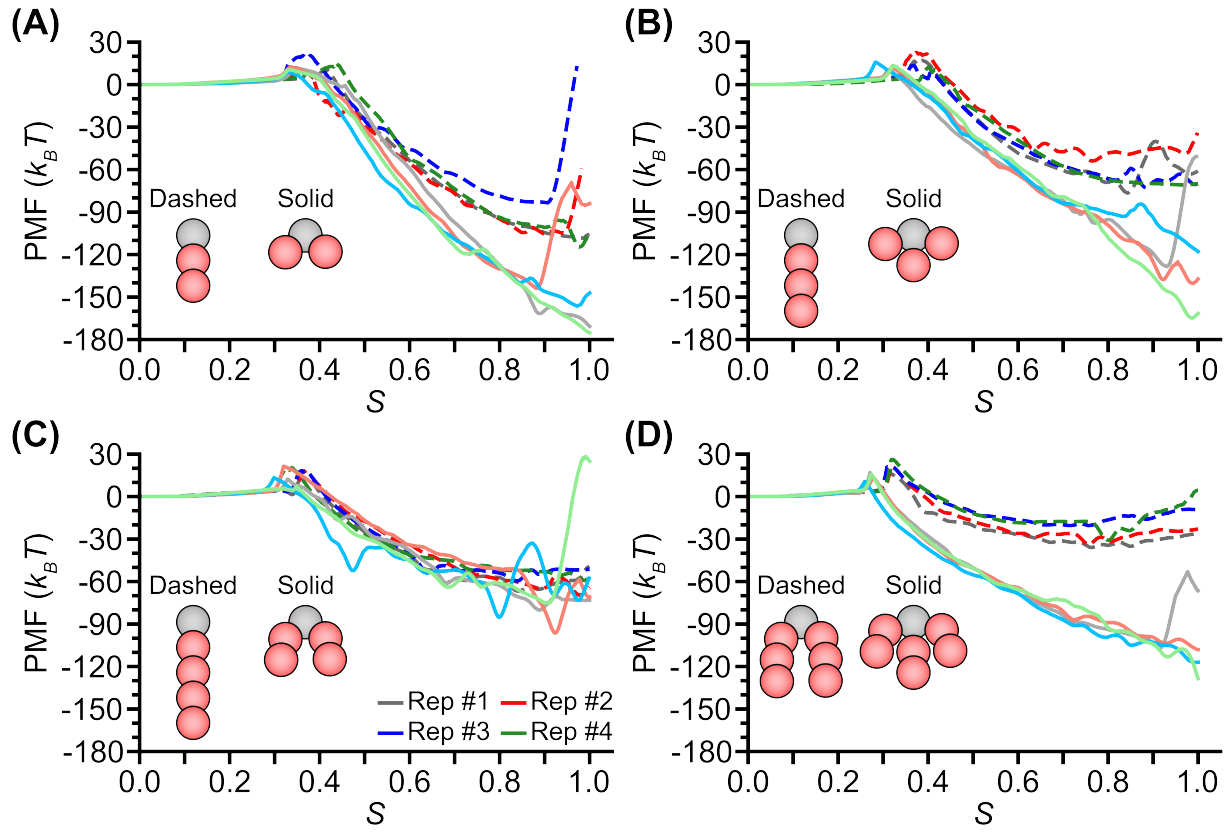


Figure 3.3: Potentials of mean force (PMF) computed along the MFEPs for: (A) 11-carbon pair, (B) 15-carbon pair, (C) 19-carbon pair, (D) 27-carbon pair. Dashed curves correspond to lower-branched alkyl R groups and solid curves correspond to higher-branched alkyl R groups. Each curve corresponds to a single replica (four replicas per ligand). PMF values for small S, corresponding to the NP in solution far from the bilayer, were set to 0 k_BT for all replicas.

observations for the PMFs between each pair of ligands reveal that replicas of higher-branched ligands (solid lines) generally exhibit a sharp free energy barrier (single peak) that is shifted to lower values of S, whereas lower-branched ligands (dashed lines) show wider free energy barriers (broader peak). Higher-branched ligands also lead to lower adsorption free energies on average with PMFs that exhibit similar and more consistent features, as opposed to the PMFs of the lower-branched counterparts that show more deviations between replicas. These observations can be correlated to more variation in umbrella sampling near the free energy barrier for adsorption where ligands with linear alkyl R groups have more windows with similar D_Z, but vary in N_C, whereas ligands with branched alkyl R groups will have less variation (Fig. S14–S21). The sharp PMF increases observed at large S for some replicas are attributed to sampling small values of D_Z and large values of N_C that can lead to subsequent transition pathways for full NP insertion into the bilayer bulk (*i.e.*, several ligands interacting with the opposite leaflet of the bilayer). However, in-depth analysis of those high free energy states is out of the scope of this manuscript and will be investigated in future work.

3.3.2 Branched R groups affect mechanisms of bilayer adsorption

To quantify the effects that branching has on adsorption thermodynamics and mechanisms, Figure 3.4 compares free energy barriers for adsorption (PMF Max.) for pairs of ligands with equal log P values but different degrees of branching. For each AuNP, we show the replica free energy barriers (white circles) and the mean free energy barrier (gray diamonds). Although replica values show moderate spread in some cases, the mean values are consistently lower for higher-branched alkyl R groups with standard deviations between replicas within 1.6 k_BT and 5.9 k_BT. Upon further inspection of the replica MFEPs (Fig. S14–S21), we attribute these deviations to slight differences in CV values for each replica. Particularly, for higher-branched alkyl R groups, replicas that show a higher free energy barrier follow an early transition state where ligand–lipid contacts are initiated at larger D_Z (*i.e.*, when the NP is farther away from the bilayer) whereas lower barriers are observed when contacts are initiated at smaller D_Z (*i.e.*, when the NP is closer to the bilayer). Additionally, CV values calculated for the window near where the free energy barriers are observed show that linear R groups generally exhibit a larger number of ligand–lipid contacts (Fig. S14–S21). The data altogether show that, as branching of the alkyl R group increases, the free energy barrier decreases and is shifted to smaller S compared to the equivalent lower-branched ligands, which corresponds to an increase in N_C at larger D_Z. These observations suggest that chain architecture modulates NP adsorption and ligand–lipid contacts through nonintuitive mechanisms.

We inspected representative snapshots from umbrella sampling windows close to where the free energy barriers were observed to identify mechanistic pathways for adsorption. In

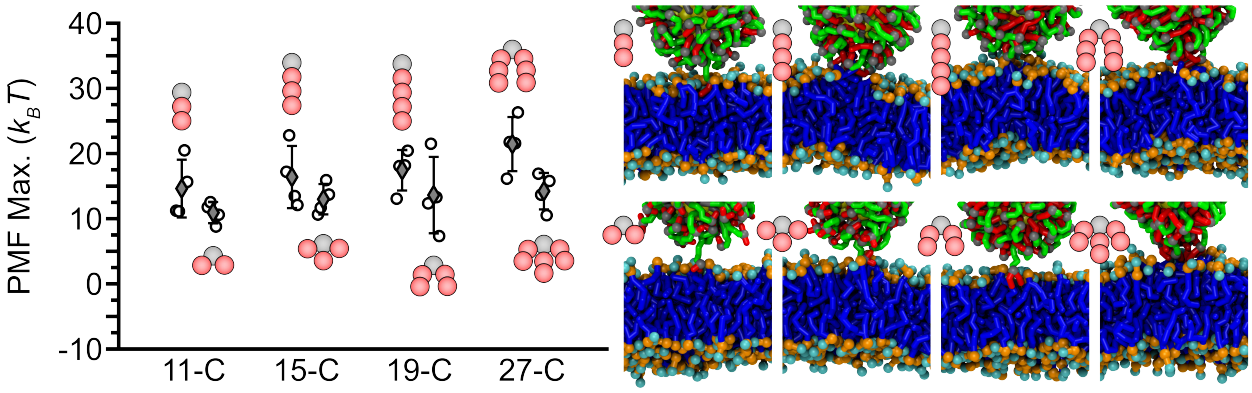


Figure 3.4: The plot shows replica values as white circles and the mean values as gray diamonds. Error was computed as the standard deviation between four replicas. Simulation snapshots were taken from the replica with the free energy barrier closest to the mean value, and from windows close to where the barrier is observed (in S). All water and counterions, and lipids in the bilayer that are in front of the AuNP were removed for visual purposes. Colors follow Figure 3.1.

our previous works, we identified three mechanisms for adsorption in which ligand R group log P determines whether adsorption occurs through favorable ligand intercalation into the bilayer or unfavorable lipid tail protrusions.[30, 31] Ligands with short and slightly lipophilic (*i.e.*, small log P) R groups require unfavorable lipid tail protrusions out of the bilayer (*i.e.*, stochastic protrusion out of the bilayer hydrophobic bulk into solution) due to the inability of short ligand alkyl chains to protrude out of the ligand monolayer (*i.e.*, stochastic protrusion out of the ligand monolayer into solution) to initiate ligand–lipid contacts. On the contrary, alkyl R groups of medium chain length and moderate lipophilicity can protrude out of the ligand monolayer to initiate contacts, minimizing unfavorable lipid tail protrusions by favorably intercalating within the bilayer. However, long and highly lipophilic ligand alkyl chains result in R groups strongly backfolding back into the ligand monolayer (*i.e.*, R groups remain partitioned within the hydrophobic core of the ligand monolayer), preventing R group protrusions, and then requiring unfavorable lipid tail protrusions to initiate NP adsorption. These mechanisms led to a nonmonotonic trend in free energy barriers to adsorption with log P. Based on these findings, we sought to compare our previous results to the previously identified mechanisms.

The representative snapshots in Figure 3.4 show that the least lipophilic AuNPs (11-C) adsorb to the bilayer through ligand intercalation (*i.e.*, red R groups intercalate into the bilayer) with mean barriers of 14.6 ± 4.4 k_BT for the linear R group and 10.9 ± 1.6 k_BT for the double-branched alkyl R group. In the case of AuNPs with intermediate lipophilicities (15-C and 19-C), we observed strikingly different adsorption mechanisms between linear and branched alkyl R groups. The AuNPs with linear ligands adsorb through backfolding lipid tail protrusions, where the R group strongly backfolds into the ligand monolayer requiring

unfavorable lipid tail protrusions to initiate adsorption (*i.e.*, blue lipid tail groups extend into the AuNP monolayer) with mean barriers of 16.4 ± 4.8 k_BT and 17.4 ± 3.1 k_BT, for the 15-C and 19-C AuNPs, respectively. However, their branched counterparts adsorbed through more favorable ligand intercalation with lower mean barriers of 13.0 ± 2.3 k_BT and 13.6 ± 5.9 k_BT, respectively. Although these are positive free energy barriers, the decreased barrier height along with the observation of ligand intercalation is in agreement with our previous conclusions that ligand intercalation is more favorable than lipid tail protrusions due to lower membrane disruption.[30] Finally, the most lipophilic AuNPs (27-C) adsorb through a previously unseen, fusion-like mechanism with a mean barrier of 21.4 ± 4.7 k_BT for the double-branched alkyl R group, and 14.2 ± 2.8 k_BT for the triple-branched alkyl R group. This mechanism consists of ligand R groups not fully protruding due to moderate backfolding but instead being highly exposed to the membrane due to steric effects induced by the branched chain architectures. This exposure, in conjunction with the inability for ligands to intercalate into the bilayer, results in the formation of a lipid bridge30 formed by the alkyl R group branches and the lipid tails at the AuNP-membrane interface. This state is similar to the lipid mixing observed during vesicle-vesicle fusion and is stabilized by (1) electrostatic attraction between the ligand TTMA groups and lipid phosphate groups, and (2) lipophilic contacts between ligand alkyl R groups and lipid tails.

3.3.3 Protrusions increase exposure of lipophilic ligand R groups

The simulation snapshots in Figure 3.4 suggest that ligand branching promotes the intercalation of ligands, motivating analysis of radial distribution functions (RDFs) to quantify the extent to which this behavior can be related to ligand protrusions into solution even when far from the bialyer.[30] In Figure 3.5 we computed the RDFs for the ligand TTMA and R groups and show that higher-branched ligands protrude into solution more than their lower-branched counterparts. To quantify the number of beads that protrude out of the ligand monolayer, we used the radius of the RDF peak corresponding to the ligand TTMA group (r_{TTMA}) as a reference cut-off distance. For the single RDF showing a binodal distribution (*i.e.*, triple-branched 27-C), we used the mean radius instead. Comparing the RDFs of the R groups and TTMA groups suggests that a number of R group beads lie at the same radial distance as that of the TTMA or farther away, indicating R group protrusions out of the ligand monolayer and into solution where they would be available to interact with the bilayer. We integrated the RDF of R groups for $r > r_{TTMA}$ (Table S2) and found that the number of beads that protrude for higher branched ligands is approximately 5×, 82×, 10×, and 5× higher for the 11-C, 15-C, 19-C, and 27-C ligand R groups, respectively. The AuNPs with ligand R groups of intermediate lipophilicities (15-C and 19-C) show the largest increase in protrusions upon increasing the number of branches, correlating with the change in adsorp-

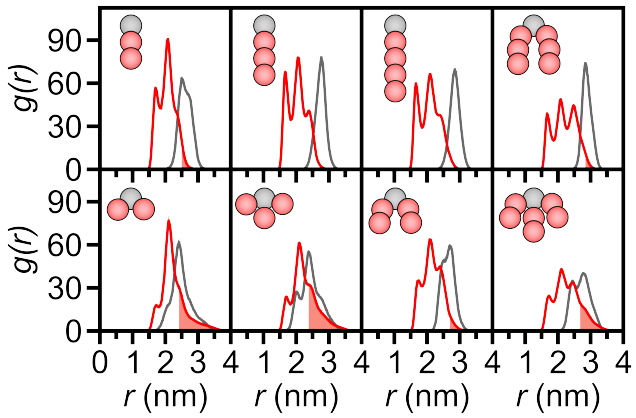


Figure 3.5: Error was computed as the standard deviation between three replicas. Integrals of the red shaded area under the curve are calculated in Table S2. Curves are color coded as the included schematic of the R groups (same as in Figure 3.1). The *gmx rdf* tool was used with a bin size of 0.01 nm to calculate $g(r)$.

tion mechanism during initial NP–bilayer contact observed in Figure 3.4. Specifically, linear architectures for 15-C and 19-C ligand R groups require unfavorable lipid tail protrusions because strong R group backfolding limits intercalation into the bilayer. However, changing the chain architecture by increasing the number of branches and decreasing the branch chain length weakens R group backfolding, increasing protrusions out of the ligand monolayer that permit favorable ligand intercalation. In contrast, the 11-C and 27-C ligands show only a 5× increase in protrusions out of the ligand monolayer for the branched alkyl R groups, but the mechanistic pathway remains the same as the lower-branched counterparts. These results are thus in agreement with the free energy calculations and qualitative observations from simulation snapshots, further indicating that R group protrusions out of the ligand monolayer at the AuNP–bilayer interface promote intercalation for ligands terminated with lipophilic alkyl R groups.

3.3.4 Ligand–lipid contacts relative to hydrophilic contacts provide insight into membrane disruption

We next sought to formulate a quantitative metric that can provide characteristic insight on NP–bilayer interactions. Specifically, we rationalized that hydrophilic contacts due to strong electrostatic attraction between the ligand TTMA and the lipid phosphate groups must be present after initial lipophilic contacts between ligand R groups and lipid tails are established, such that comparing the balance of hydrophilic vs. lipophilic contacts could provide insight into interactions that impact adsorption free energy barriers. Therefore, in Figure 3.6 we computed $\hat{N}_C$ as the contacts between lipid tails and different ligand groups (*i.e.*, hydrophobic backbone, PEG chains, and R groups) normalized by the number of hydrophilic contacts. These relative ligand–lipid contacts were calculated for the trajectory corresponding to the umbrella sampling window closest to where the free energy barrier was

observed. Only groups lower than 1 nm below the center of mass of the AuNP and lipids within a cylinder with a 3 nm radius centered around the center of mass of the AuNP were considered for the calculation. These strict cut-offs restricted the calculation to only lipids at the AuNP–bilayer interface and excludes lipids that may have been extracted.

Figure 3.6 reveals that for all pairs of AuNPs, the backbone and PEG groups of the lower-branched ligands come into contact with lipid tails (positive BB and PEG values of $\hat{N}_C$). For the linear 11-C ligand R group, these contacts are present because the intercalated ligand can pull the NP close to bilayer without extracting lipids or causing lipid tails to unfavorably protrude out of the bilayer. This observation is in agreement with the less steep MFEP and earlier onset of contacts slightly farther away from the bilayer as observed in the MFEPs in Fig. S14–S21. For the linear 15-C and 19-C ligand R groups, the larger number of relative contacts for backbone and PEG chains is associated with lipid tails protruding out of the bilayer because the longer alkyl chains strongly backfold into the ligand monolayer. In contrast, the double-branched 27-C ligand R group has very few relative contacts with the backbone and PEG chains, but significantly more relative contacts with R groups. However, visualization of the umbrella sampling trajectories revealed that in one of the replicas, a lipid bridge was formed, but later relaxed by extracting a single lipid. The lipid extraction process thus produced the low number of relative contacts with the core groups of the ligand monolayer. For the rest of the trajectories, states alternate between semi-fusion through a lipid bridge, and ligand intercalation, suggesting that this alternating behavior could lead to slightly higher than expected free energy barriers for the double-branched 27-C ligand R group in Figure 3.4.

Surprisingly, none of the higher branched counterparts show any lipid contacts with the backbone and PEG chains of the ligands. For the higher-branched 11-C, 15-C, and

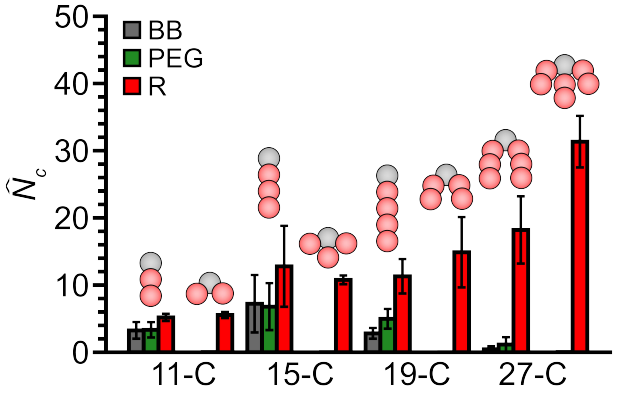


Figure 3.6: Contacts between ligand groups and lipid tails normalized by the number of hydrophilic contacts between ligand TTMA and lipid phosphate groups. Contacts were defined using a cut-off distance of 0.705 nm, corresponding to 1.5 × 0.47 nm (standard diameter of a MARTINI bead). Error was computed as the standard error between four replicas.

19-C ligand R groups, this correlates to ligands fully intercalating into the bilayer, which minimizes lipid tail protrusions that can reach the ligand backbone and PEG groups within the ligand monolayer. For both double- and triple-branched 27-C ligand R groups (after accounting for the single lipid extraction event), the large number of lipid relative contacts are due to the lipid bridge that stabilizes the semi-fused state. The much larger relative contacts for the triple-branched 27-C ligand R group are in agreement with visual inspection of the trajectories. As observed in the corresponding simulation snapshot from Figure 3.4, the lipid bridge appears to be more pronounced with slightly more R groups extended and in contact with more lipid tails due to more lateral displacement of lipids that exposes the hydrophobic bulk of the bilayer.

These data show that lipophilic contacts between NP–grafted ligands and lipids play an important role in NP adsorption to lipid bilayers. In particular, increased branching of ligand alkyl R groups reduces lipid tail contacts with the backbone and PEG chains of ligands by minimizing bilayer–disrupting lipid tail protrusions and lipid extraction. At the same time, lipophilic contacts between the ligand R groups and lipid tails either remain high or increase by promoting favorable NP–bilayer interactions. Therefore, the trends observed with the lipid relative contacts further support our hypothesis that branched ligand alkyl R groups can lower free energy barriers for adsorption by promoting favorable ligand intercalation that minimizes membrane disruption.

3.3.5 Branched R groups substantially increases thermodynamic stability of adsorbed AuNPs

Having established the effect of branching on mechanisms underlying the onset of adsorption to the bilayer, corresponding to state (ii) in Figure 3.2A, we next compared adsorption free energies to determine the effect of branching on the thermodynamics of adsorption, corresponding to state (iii) in Figure 3.2A. Figure 3.7 shows values of PMF Min. which are equivalent to adsorption free energies. Comparing values between the higher-branched ligands and the lower-branched ligands reveals that within pairs of ligands of similar log P, increased branching of the ligand alkyl R group lowers the adsorption free energy by 20.4 k_BT up to 85.0 k_BT when averaged across replicas, depending upon the ligand R group. The linear 11-C and 15-C R groups have mean adsorption free energies of -103.0 ± 13.5 k_BT and -68.6 ± 10.0 k_BT, respectively, while their double-branched and triple-branched counterparts have mean adsorption free energies of -161.6 ± 14.3 k_BT and -137.9 ± 20.2 k_BT, respectively. At very high log P, the double-branched 27-C ligand has a mean adsorption free energy of -30.3 ± 6.9 k_BT, while the triple-branched has a mean adsorption free energy of -115.3 ± 9.9 k_BT. Overall, the higher-branched R groups for these three pairs of ligands have over 50% more negative adsorption free energies when compared to

their lower-branched counterparts. The substantially lower adsorption free energies for the higher-branched ligands indicate that AuNPs functionalized with branched alkyl R groups adsorb more strongly to lipid bilayers in comparison to R groups with fewer branches despite similar log P values.

The adsorption free energies along with the simulation snapshots show that branching leads to a significantly different adsorbed state at large values of S that reflects the change in adsorption free energy. The simulation snapshots in Figure 3.7 reveal that AuNPs functionalized with the lower-branched ligands (top row) are stably bound to the outer leaflet of the bilayer. In this state, lipids are extracted into the ligand monolayer and ligands have their lipophilic R groups partition into the bilayer due to attractive interactions with lipid tails. However, for the higher-branched ligands, the AuNPs assume configurations in which the charged groups of the ligands fully cross the membrane and are now bound to the opposite leaflet, acting like "anchors", with their R groups partitioning towards the hydrophobic core of the bilayer and preventing the AuNP from desorbing. Such states, where AuNP-grafted ligands are distributed between both leaflets, have been identified to be metastable for negatively charged ligands.[37, 57, 74, 75] On the contrary, the linear and branched 19-C ligands show the smallest difference in adsorption free energy ($-20.4\ k_BT$) with mean values of $-63.8 \pm 5.2\ k_BT$ and $-84.2 \pm 9.1\ k_BT$, respectively. In this case, both AuNPs remain stably bound to the upper leaflet without any ligands having crossed the membrane core. Figure 3.7 thus shows that a change in chain architecture of alkyl R groups can lead to substantially increased AuNP adsorption and corresponding mechanistic changes. Furthermore, observing such favorable adsorption free energies for AuNPs in a partially inserted state suggests that these NPs should exhibit increased cellular entry, in line with prior experimental

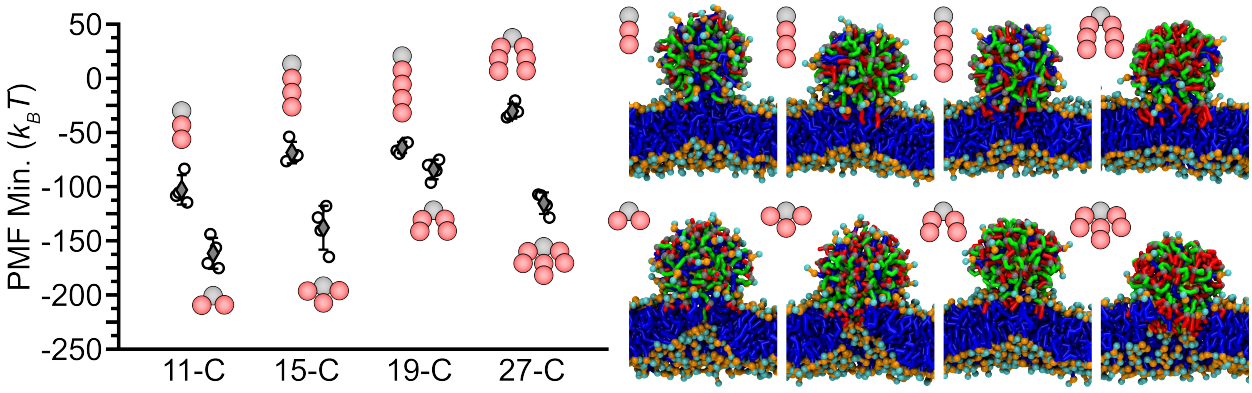


Figure 3.7: The plot shows replica values as white circles and mean values as gray diamonds. Error was computed as the standard deviation between four replicas. Simulation snapshots were taken from the replica with the adsorption free energy closest to the mean value, and from windows close to where the global free energy minimum is observed (as a function of S). All water beads, counterions, and lipids in the bilayer that are in front of the AuNP were removed for visual purposes. Colors follow Figure 3.1.

observations.[9]

Finally, Figure 3.7 also shows that increasing log P for either linear or branched ligand R groups increases the adsorption free energies (*i.e.*, more positive PMF Min.), which might seem counterintuitive as increased R group lipophilicity would be expected to increase favorable interactions with the hydrophobic lipid tails and thus decrease adsorption free energies. We attribute this trend to an interplay between the free volume of the ligand monolayer and lipid extraction. Shorter, less lipophilic R groups are exposed to water prior to adsorption, resulting in a large free volume within the ligand monolayer that also exposes hydrophobic ligand backbones to water; this behavior is more pronounced for branched ligands, as further discussed below. Upon adsorption, lipid extraction into the ligand monolayer permits hydrophobic interactions between lipid tails and ligand backbones to promote a highly favorable adsorption free energy. Increasing R group lipophilicity (log P), however, leads to R group backfolding into the ligand monolayer prior to adsorption due to hydrophobic interactions between the ligand R group and ligand backbones. Backfolding decreases the free volume with the ligand monolayer, and consequently adsorption is less favorable since lipid extraction is reduced and leads to fewer new hydrophobic interactions with ligand backbones. These observations reinforce our hypothesis that R group lipophilicity alone is insufficient to capture the complex set of ligand–ligand, ligand–lipid, and ligand–water interactions that collectively determine the thermodynamics of adsorption.

3.3.6 Surface exposure of lipophilic R groups influences adsorption free energies

We further investigated how ligand alkyl R group branching promotes adsorption by computing the solvent–accessible surface area (SASA) for the R group lipophilic beads of the AuNPs in solution and in a fully adsorbed state. We hypothesized that branching induces a steric effect that increases exposure of lipophilic groups to water, introducing a free energy penalty that is eliminated upon AuNP adsorption because this nonpolar surface area can be sequestered within the nonpolar environment of the membrane core. This hydrophobic driving force would be consistent with previous studies that show that lipophilic contacts are one of the main driving forces for NP adsorption to lipid bilayers[30, 31, 36, 37] and ligand–receptor binding.[76, 77] We thus computed the R group SASA for each pair of AuNPs in solution and for the AuNPs in the fully adsorbed state using the umbrella sampling trajectories corresponding to the adsorption free energies in Figure 3.7 to determine how R groups lead to a reduced SASA due to adsorption to the bilayer or lipid extraction.

Figure 3.8 shows that trends in the SASA for each pair of AuNPs in solution (white bars) agree with the trends observed for protrusions in Figure 3.5 and Table S2; the higher-

branched 11-C, 15-C, and 27-C R groups show significantly larger SASA than their lower-branched counterparts just as these exhibit significantly more protrusions. The difference in SASA between the linear and branched 19-C R group pair is minimal and this pair also exhibits the fewest protrusions. For AuNPs in their adsorbed state, these overall trends generally remain the same with higher-branched ligands having higher SASA. Comparing the difference in SASA between AuNPs in the solution and adsorbed states for each ligand pair generally shows that at fixed log P, the relative difference in SASA between lower- and higher-branched R groups agree with trends in the adsorption free energies in Figure 3.7. Lower-branched R groups exhibit a smaller decrease in SASA when transitioning from the solution to adsorbed states and have less favorable (less negative) adsorption free energies, whereas higher-branched R groups have a larger decrease in SASA when transition from solution to adsorbed states and have more favorable (more negative) adsorption free energies. Therefore, large relative changes in SASA between AuNPs in solution and adsorbed to the bilayers, as well as higher absolute SASA, are indicative of lower adsorption free energies, reflecting the hydrophobic driving force discussed above. We attribute this behavior primarily to the disruption of packing in the ligand monolayer by higher-branched R groups, which increases the SASA in solution and decreases the SASA upon adsorption by both promoting lipid extraction to shield exposed nonpolar surface area in the ligand monolayer and sequestering a large number of R groups within the hydrophobic core of the bilayer. The apparent exception is the 19-C R group pair, which has a small decrease in SASA for both the linear and branched groups and correspondingly similar adsorption free energies.

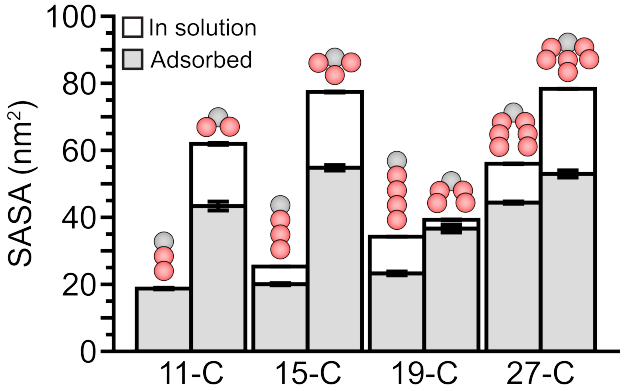


Figure 3.8: Decrease in R group solvent-accessible surface area (SASA) upon AuNP adsorption to lipid bilayers. The SASA was computed only for the lipophilic beads of the R groups. White bars correspond to the SASA calculated for AuNPs solvated in water without a bilayer. Grey bars correspond to the SASA calculated for AuNPs adsorbed to the bilayer using the trajectories from umbrella windows close to where the global free energy minimum is observed (as a function of S). SASA for the adsorbed 11-C linear R group AuNP overlaps the SASA of the AuNP in solution by 0.83 nm^2. Error was computed as the standard error between three replicas for the AuNPs in solution and between four replicas for the AuNPs adsorbed to the bilayer. The *gmx sasa*[78] tool was used to calculate the SASA with a probe radius of 0.26 nm and 4800 grid points.

3.3.7 Ligands with branched R groups exhibit lipid-like behaviors

The effects of alkyl chain architecture that we have described are consistent with similar studies based on structure–activity relationships between linear and branched alkyl moieties in a variety of contexts. For example, branching leads to increased stability for ligand-functionalized nanocrystals,[79] higher dispersibility of metal–oxide nanoparticles in hydrophobic solvents,[80] more potent antifungal activity for alkyl gallates,[81] improved intracellular delivery of mRNA-lipid nanoparticles,[82] and superior power conversion for small molecule-based organic solar cells.[83] Although these previous reports are based on other classes of materials, the main conclusion that chain architecture modulates different functions can be generalized to the NP–bilayer interactions studied here.

Perhaps most relevant are observations on the effect of branching on the properties of lipids through both computational[84] and experimental[82] methods. Shinoda and colleagues used MD simulations to compare DPPC and DPhPC lipid bilayers, where the latter only differs from the former by having four additional methyl groups as side chains in each tail.[84] They concluded that lipid tail branching in DPhPC bilayers disrupts lipid packing, but increases bilayer stability due to the entrapment of lipid tails between neighboring lipids. More recently, Hashiba and colleagues systematically studied the effects of lipid tail symmetry and total carbon number in lipid nanoparticles for mRNA delivery.[82] Through hemolysis assays, they discovered that increased packing disruption due to tail branching promotes endosomal escape. Similarly, in the AuNPs studied in this work, branching minimizes backfolding of ligand alkyl R groups by disrupting ligand monolayer packing (analogous to lipid packing in bilayers). Similar packing disruption increase the exposure of lipophilic groups to lipid tails through ligand intercalation, thus decreasing free energy barriers for adsorption. In analogy to lipid properties that influence bilayer structure, this comparison suggests avenues for exploring alternative variations to ligand properties, such as varying the degree of ligand saturation of bulkiness, to further disrupt monolayer packing as a means of influencing bilayer interactions.

3.4 Conclusions

In this work, we employed coarse-grained (CG) molecular dynamics simulations using the MARTINI force field to elucidate the thermodynamics and mechanisms of AuNP adsorption to zwitterionic DIPC lipid bilayers by expanding upon our previous computational framework.[30] to study AuNPs. We systematically studied a library of AuNPs grafted with cationic ligands and terminated with alkyl R groups in which we determined the effects of alkyl R group branching by selecting four pairs of R groups in which each pair had R groups of similar log P (*i.e.*, number of hydrophobic beads) but with different chain archi-

tectures (*i.e.*, number of alkyl branches). We show that, within pairs of AuNPs with ligands of similar log P, increased ligand alkyl R group branching reduces free energy barriers for adsorption. The branched chain architectures inhibit R group packing (backfolding) within the ligand monolayer and increase protrusions into solution. This effect alters the mechanism for adsorption by promoting favorable ligand intercalation within the bilayer, which minimizes bilayer disruption. Moreover, we show that for highly lipophilic and branched R groups, adsorption proceeds through a fusion-like mechanism where a lipid bridge forms at the AuNP–bilayer interface. For the same pairs of AuNPs, increased branching also leads to significantly more favorable adsorption free energies. The higher number of branches leads to an increased unfavorable exposure of nonpolar R groups to water, incurring in a free energy penalty. Adsorption to the lipid bilayer eliminates this energetic penalty as the R groups instead sequester nonpolar surface area within the membrane core.

This study provides significant and valuable insight into the effects that alkyl R group chain architecture of NP-grafted ligands can have on NP–bilayer interactions and show that using log P as a sole descriptor for AuNP adsorption to lipid bilayers may not be sufficient to predict cellular interactions. The impact of branching suggests design rules that can be leveraged in the engineering of nanomaterials for biomedical applications to improve cellular uptake and intracellular delivery while minimizing undesired membrane disruption that can lead to adverse effects such as cytotoxicity and hemolysis. Finally, an unexpected observation is that AuNPs with branched ligands can achieve partially inserted states in which some ligand charged groups cross the hydrophobic core of the bilayer to interact with the opposite leaflet even though the barrier for the crossing of a single charged ligand is approximately 10 k_BT in AA simulations[52] and 16[37] to 30[35]k_BT in CG simulations. Although the reaction coordinate we employ to describe adsorption does not capture free energy barriers for these crossing events, their observation suggests that these are energetically favorable configurations seemingly facilitated by the disruption of lipid tail packing within the membrane core by branched R groups. Future work will explore the thermodynamics of such ligand translocation processes to determine if branching can be employed to achieve direct AuNP translocation across the bilayer.

References

[1] R. Mout, D. F. Moyano, S. Rana, V. M. Rotello, "Surface functionalization of nanoparticles for nanomedicine", *Chemical Society Reviews* **2012**, *41*, 2539–2544.

[2] G. Sanità, B. Carrese, A. Lamberti, "Nanoparticle Surface Functionalization: How to Improve Biocompatibility and Cellular Internalization", *Frontiers in Molecular Biosciences* **2020**, *7*, DOI 10.3389/fmolb.2020.587012.

[3] Y. Kumar, A. S. K. Sinha, K. D. P. Nigam, D. Dwivedi, J. S. Sangwai, "Functionalized nanoparticles: Tailoring properties through surface energetics and coordination chemistry for advanced biomedical applications", *Nanoscale* **2023**, *15*, 6075–6104.

[4] D. P. Linklater, X. Le Guével, G. Bryant, V. A. Baulin, E. Pereiro, P. G. T. Perera, J. V. Wandiyanto, S. Juodkazis, E. P. Ivanova, "Lethal Interactions of Atomically Precise Gold Nanoclusters and Pseudomonas aeruginosa and Staphylococcus aureus Bacterial Cells", *ACS Applied Materials & Interfaces* **2022**, *14*, 32634–32645.

[5] S. Jiang, K. Y. Win, S. Liu, C. P. Teng, Y. Zheng, M.-Y. Han, "Surface-functionalized nanoparticles for biosensing and imaging-guided therapeutics", *Nanoscale* **2013**, *5*, 3127–3148.

[6] F. Ghaemi, A. Amiri, M. Y. Bajuri, N. Y. Yuhana, M. Ferrara, "Role of different types of nanomaterials against diagnosis, prevention and therapy of COVID-19", *Sustainable Cities and Society* **2021**, *72*, 103046.

[7] N. Kim, Y.-G. Jeong, S. Lee, J. Kang, Y. Kim, Y.-A. Choi, D. Khang, S.-H. Kim, "Ameliorated Skin Inflammation through the Synergistic Effect of Gold Nanorod–Dexamethasone and Photothermal Therapy", *ACS Applied Materials & Interfaces* **2024**, *16*, 12217–12231.

[8] R. Das, R. F. Landis, G. Y. Tonga, R. Cao-Milán, D. C. Luther, V. M. Rotello, "Control of Intra- versus Extracellular Bioorthogonal Catalysis Using Surface-Engineered Nanozymes", *ACS Nano* **2019**, *13*, 229–235.

[9] Y. Jiang, S. Huo, T. Mizuhara, R. Das, Y.-W. Lee, S. Hou, D. F. Moyano, B. Duncan, X.-J. Liang, V. M. Rotello, "The Interplay of Size and Surface Functionality on the Cellular Uptake of Sub-10 nm Gold Nanoparticles", *ACS Nano* **2015**, *9*, 9986–9993.

[10] X. Bai, S. Wang, X. Yan, H. Zhou, J. Zhan, S. Liu, V. K. Sharma, G. Jiang, H. Zhu, B. Yan, "Regulation of Cell Uptake and Cytotoxicity by Nanoparticle Core under the Controlled Shape, Size, and Surface Chemistries", *ACS Nano* **2020**, *14*, 289–302.

[11] Y. Xiao, W. Xu, Y. Komohara, Y. Fujiwara, H. Hirose, S. Futaki, T. Niidome, "Effect of Surface Modifications on Cellular Uptake of Gold Nanorods in Human Primary Cells and Established Cell Lines", *ACS Omega* **2020**, *5*, 32744–32752.

[12] D. F. Moyano, K. Saha, G. Prakash, B. Yan, H. Kong, M. Yazdani, V. M. Rotello, "Fabrication of Corona-Free Nanoparticles with Tunable Hydrophobicity", *ACS Nano* **2014**, *8*, 6748–6755.

[13] K. Saha, M. Rahimi, M. Yazdani, S. T. Kim, D. F. Moyano, S. Hou, R. Das, R. Mout, F. Rezaee, M. Mahmoudi, V. M. Rotello, "Regulation of Macrophage Recognition through the Interplay of Nanoparticle Surface Functionality and Protein Corona", *ACS Nano* **2016**, *10*, 4421–4430.

[14] C. M. Goodman, C. D. McCusker, T. Yilmaz, V. M. Rotello, "Toxicity of Gold Nanoparticles Functionalized with Cationic and Anionic Side Chains", *Bioconjugate Chemistry* **2004**, *15*, 897–900.

[15] K. Saha, D. F. Moyano, V. M. Rotello, "Protein coronas suppress the hemolytic activity of hydrophilic and hydrophobic nanoparticles", *Materials Horizons* **2013**, *1*, 102–105.

[16] B. D. Chithrani, A. A. Ghazani, W. C. W. Chan, "Determining the Size and Shape Dependence of Gold Nanoparticle Uptake into Mammalian Cells", *Nano Letters* **2006**, *6*, 662–668.

[17] B. Peter, N. Kanyo, K. D. Kovacs, V. Kovács, I. Szekacs, B. Pécz, K. Molnár, H. Nakanishi, I. Lagzi, R. Horvath, "Glycocalyx Components Detune the Cellular Uptake of Gold Nanoparticles in a Size- and Charge-Dependent Manner", *ACS Applied Bio Materials* **2023**, *6*, 64–73.

[18] D. Cheng, X. Li, G. Zhang, H. Shi, "Morphological effect of oscillating magnetic nanoparticles in killing tumor cells", *Nanoscale Research Letters* **2014**, *9*, 195.

[19] M. Siek, K. Kandere-Grzybowska, B. A. Grzybowski, "Mixed-Charge, pH-Responsive Nanoparticles for Selective Interactions with Cells, Organelles, and Bacteria", *Accounts of Materials Research* **2020**, *1*, 188–200.

[20] M. Epple, V. M. Rotello, K. Dawson, "The Why and How of Ultrasmall Nanoparticles", *Accounts of Chemical Research* **2023**, *56*, 3369–3378.

[21] A. Gupta, W. Ndugire, C.-M. Hirschbiegel, L. Grigely, V. M. Rotello, "Interfacing Nanomaterials with Biology through Ligand Engineering", *Accounts of Chemical Research* **2023**, *56*, 2151–2169.

[22] A. Verma, O. Uzun, Y. Hu, Y. Hu, H.-S. Han, N. Watson, S. Chen, D. J. Irvine, F. Stellacci, "Surface-structure-regulated cell-membrane penetration by monolayer-protected nanoparticles", *Nature Materials* **2008**, *7*, 588–595.

[23] Y.-S. S. Yang, P. U. Atukorale, K. D. Moynihan, A. Bekdemir, K. Rakhra, L. Tang, F. Stellacci, D. J. Irvine, "High-throughput quantitation of inorganic nanoparticle biodistribution at the single-cell level using mass cytometry", *Nature Communications* **2017**, *8*, 14069.

[24] P. Pengo, M. Şologan, L. Pasquato, F. Guida, S. Pacor, A. Tossi, F. Stellacci, D. Marson, S. Boccardo, S. Pricl, P. Posocco, "Gold nanoparticles with patterned surface monolayers for nanomedicine: current perspectives", *European Biophysics Journal* **2017**, *46*, 749–771.

[25] A. Chompoosor, K. Saha, P. S. Ghosh, D. J. Macarthy, O. R. Miranda, Z.-J. Zhu, K. F. Arcaro, V. M. Rotello, "The Role of Surface Functionality on Acute Cytotoxicity, ROS Generation and DNA Damage by Cationic Gold Nanoparticles", *Small* **2010**, *6*, 2246–2249.

[26] Z.-J. Zhu, T. Posati, D. F. Moyano, R. Tang, B. Yan, R. W. Vachet, V. M. Rotello, "The Interplay of Monolayer Structure and Serum Protein Interactions on the Cellular Uptake of Gold Nanoparticles", *Small* **2012**, *8*, 2659–2663.

[27] K. Saha, S. T. Kim, B. Yan, O. R. Miranda, F. S. Alfonso, D. Shlosman, V. M. Rotello, "Surface Functionality of Nanoparticles Determines Cellular Uptake Mechanisms in Mammalian Cells", *Small* **2013**, *9*, 300–305.

[28] A. K. Chew, B. C. Dallin, R. C. Van Lehn, "The Interplay of Ligand Properties and Core Size Dictates the Hydrophobicity of Monolayer-Protected Gold Nanoparticles", *ACS Nano* **2021**, *15*, 4534–4545.

[29] A. K. Chew, J. A. Pedersen, R. C. Van Lehn, "Predicting the Physicochemical Properties and Biological Activities of Monolayer-Protected Gold Nanoparticles Using Simulation-Derived Descriptors", *ACS Nano* **2022**, *16*, 6282–6292.

[30] C. A. Huang-Zhu, J. K. Sheavly, A. K. Chew, S. J. Patel, R. C. Van Lehn, "Ligand Lipophilicity Determines Molecular Mechanisms of Nanoparticle Adsorption to Lipid Bilayers", *ACS Nano* **2024**, *18*, 6424–6437.

[31] C. A. Lochbaum, A. K. Chew, X. Zhang, V. Rotello, R. C. Van Lehn, J. A. Pedersen, "Lipophilicity of Cationic Ligands Promotes Irreversible Adsorption of Nanoparticles to Lipid Bilayers", *ACS Nano* **2021**, *15*, 6562–6572.

[32] A. Marzouq, L. Morgenstein, C. A. Huang-Zhu, S. Yudovich, A. Atkins, A. Grupi, R. C. Van Lehn, S. Weiss, "Long-Chain Lipids Facilitate Insertion of Large Nanoparticles into Membranes of Small Unilamellar Vesicles", *Langmuir* **2024**, *40*, 10477–10485.

[33] B. Cao, M. Hu, Y. Cheng, P. Jing, B. Liu, B. Zhou, X. Wang, R. Gao, X. Sun, Y. Du, J. Zhang, "Tailoring the d-band center of N-doped carbon nanotube arrays with Co4N nanoparticles and single-atom Co for a superior hydrogen evolution reaction", *NPG Asia Materials* **2021**, *13*, 1.

[34] G. Rossi, L. Monticelli, "Gold nanoparticles in model biological membranes: A computational perspective", *Biochimica et Biophysica Acta (BBA) - Biomembranes*, Biosimulations of lipid membranes coupled to experiments **2016**, *1858*, 2380–2389.

[35] E. Canepa, S. Salassi, F. Simonelli, R. Ferrando, R. Rolandi, C. Lambruschini, F. Canepa, S. Dante, A. Relini, G. Rossi, "Non-disruptive uptake of anionic and cationic gold nanoparticles in neutral zwitterionic membranes", *Scientific Reports* **2021**, *11*, 1256.

[36] R. C. Van Lehn, M. Ricci, P. H. J. Silva, P. Andreozzi, J. Reguera, K. Voïtchovsky, F. Stellacci, A. Alexander-Katz, "Lipid tail protrusions mediate the insertion of nanoparticles into model cell membranes", *Nature Communications* **2014**, *5*, 4482.

[37] F. Simonelli, D. Bochicchio, R. Ferrando, G. Rossi, "Monolayer-Protected Anionic Au Nanoparticles Walk into Lipid Membranes Step by Step", *The Journal of Physical Chemistry Letters* **2015**, *6*, 3175–3179.

[38] Y. Cao, J. Zhu, J. Kou, D. P. Tieleman, Q. Liang, "Unveiling Interactions of Tumor-Targeting Nanoparticles with Lipid Bilayers Using a Titratable Martini Model", *Journal of Chemical Theory and Computation* **2024**, *20*, 4045–4053.

[39] Y. Oh, Q. Cui, "Non-equilibrium transport of nanoparticles across the lipid membrane", *Nanoscale* **2023**, *15*, 12307–12318.

[40] M. Wang, S.-D. Ni, Y.-W. Yin, Y.-Q. Ma, H.-M. Ding, "Molecular Modeling of the Fluorination Effect on the Penetration of Nanoparticles across Lipid Bilayers", *Langmuir* **2024**, *40*, 1295–1304.

[41] X. Chen, D. P. Tieleman, Q. Liang, "Modulating interactions between ligand-coated nanoparticles and phase-separated lipid bilayers by varying the ligand density and the surface charge", *Nanoscale* **2018**, *10*, 2481–2491.

[42] S. Franco-Ulloa, D. Guarnieri, L. Riccardi, P. P. Pompa, M. De Vivo, "Association Mechanism of Peptide-Coated Metal Nanoparticles with Model Membranes: A Coarse-Grained Study", *Journal of Chemical Theory and Computation* **2021**, *17*, 4512–4523.

[43] M. Das, U. Dahal, O. Mesele, D. Liang, Q. Cui, "Molecular Dynamics Simulation of Interaction between Functionalized Nanoparticles with Lipid Membranes: Analysis of Coarse-Grained Models", *The Journal of Physical Chemistry B* **2019**, *123*, 10547–10561.

[44] F. Lolicato, L. Joly, H. Martinez-Seara, G. Fragneto, E. Scoppola, F. Baldelli Bombelli, I. Vattulainen, J. Akola, M. Maccarini, "The Role of Temperature and Lipid Charge on Intake/Uptake of Cationic Gold Nanoparticles into Lipid Bilayers", *Small* **2019**, *15*, 1805046.

[45] H.-m. Ding, W.-d. Tian, Y.-q. Ma, "Designing Nanoparticle Translocation through Membranes by Computer Simulations", *ACS Nano* **2012**, *6*, 1230–1238.

[46] L.-y. Huang, Y.-s. Yu, X. Lu, H.-m. Ding, Y.-q. Ma, "Designing a nanoparticle-containing polymeric substrate for detecting cancer cells by computer simulations", *Nanoscale* **2019**, *11*, 2170–2178.

[47] H. Nakamura, K. Sezawa, M. Hata, S. Ohsaki, S. Watano, "Direct translocation of nanoparticles across a model cell membrane by nanoparticle-induced local enhancement of membrane potential", *Physical Chemistry Chemical Physics* **2019**, *21*, 18830–18838.

[48] K. Shimizu, H. Nakamura, S. Watano, "MD simulation study of direct permeation of a nanoparticle across the cell membrane under an external electric field", *Nanoscale* **2016**, *8*, 11897–11906.

[49] Y. Ikeda, H. Nakamura, S. Ohsaki, S. Watano, "Direct translocation of a negatively charged nanoparticle across a negatively charged model cell membrane", *Physical Chemistry Chemical Physics* **2021**, *23*, 10591–10599.

[50] D. Nguyen, J. Wu, P. Corrigan, Y. Li, "Computational investigation on lipid bilayer disruption induced by amphiphilic Janus nanoparticles: combined effect of Janus balance and charged lipid concentration", *Nanoscale* **2023**, *15*, 16112–16130.

[51] Y.-Q. Chen, M.-D. Xue, J.-L. Li, D. Huo, H.-M. Ding, Y. Ma, "Uncovering the Importance of Ligand Mobility on Cellular Uptake of Nanoparticles: Insights from Experimental, Computational, and Theoretical Investigations", *ACS Nano* **2024**, *18*, 6463–6476.

[52] R. C. V. Lehn, A. Alexander-Katz, "Energy landscape for the insertion of amphiphilic nanoparticles into lipid membranes: A computational study", *PLOS ONE* **2019**, *14*, e0209492.

[53] R. C. Van Lehn, A. Alexander-Katz, "Fusion of Ligand-Coated Nanoparticles with Lipid Bilayers: Effect of Ligand Flexibility", *The Journal of Physical Chemistry A* **2014**, *118*, 5848–5856.

[54] R. C. V. Lehn, A. Alexander-Katz, "Pathway for insertion of amphiphilic nanoparticles into defect-free lipid bilayers from atomistic molecular dynamics simulations", *Soft Matter* **2015**, *11*, 3165–3175.

[55] J. K. Sheavly, J. A. Pedersen, R. C. V. Lehn, "Curvature-driven adsorption of cationic nanoparticles to phase boundaries in multicomponent lipid bilayers", *Nanoscale* **2019**, *11*, 2767–2778.

[56] J. K. Sheavly, R. C. Van Lehn, "Bilayer-mediated assembly of cationic nanoparticles adsorbed to lipid bilayers: Insights from molecular simulations", *AIChE Journal* **2020**, *66*, e16993.

[57] P. Gkeka, P. Angelikopoulos, L. Sarkisov, Z. Cournia, "Membrane Partitioning of Anionic, Ligand-Coated Nanoparticles Is Accompanied by Ligand Snorkeling, Local Disordering, and Cholesterol Depletion", *PLOS Computational Biology* **2014**, *10*, e1003917.

[58] S. J. Patel, R. C. Van Lehn, "Analysis of Charged Peptide Loop-Flipping across a Lipid Bilayer Using the String Method with Swarms of Trajectories", *The Journal of Physical Chemistry B* **2021**, *125*, 5862–5873.

[59] A. C. Pan, D. Sezer, B. Roux, "Finding Transition Pathways Using the String Method with Swarms of Trajectories", *The Journal of Physical Chemistry B* **2008**, *112*, 3432–3440.

[60] L. Maragliano, B. Roux, E. Vanden-Eijnden, "Comparison between Mean Forces and Swarms-of-Trajectories String Methods", *Journal of Chemical Theory and Computation* **2014**, *10*, 524–533.

[61] D. Branduardi, F. L. Gervasio, M. Parrinello, "From A to B in free energy space", *The Journal of Chemical Physics* **2007**, *126*, 054103.

[62] A. K. Ghose, G. M. Crippen, "Atomic physicochemical parameters for three-dimensional-structure-directed quantitative structure-activity relationships. 2. Modeling dispersive and hydrophobic interactions", *Journal of Chemical Information and Computer Sciences* **1987**, *27*, 21–35.

[63] W. Humphrey, A. Dalke, K. Schulten, "VMD: Visual molecular dynamics", *Journal of Molecular Graphics* **1996**, *14*, 33–38.

[64] D. Van Der Spoel, E. Lindahl, B. Hess, G. Groenhof, A. E. Mark, H. J. C. Berendsen, "GROMACS: Fast, flexible, and free", *Journal of Computational Chemistry* **2005**, *26*, 1701–1718.

[65] G. A. Tribello, M. Bonomi, D. Branduardi, C. Camilloni, G. Bussi, "PLUMED 2: New feathers for an old bird", *Computer Physics Communications* **2014**, *185*, 604–613.

[66] H. M. Khan, P. C. T. Souza, S. Thallmair, J. Barnoud, A. H. de Vries, S. J. Marrink, N. Reuter, "Capturing Choline–Aromatics Cation− Interactions in the MARTINI Force Field", *Journal of Chemical Theory and Computation* **2020**, *16*, 2550–2560.

[67] D. H. de Jong, G. Singh, W. F. D. Bennett, C. Arnarez, T. A. Wassenaar, L. V. Schäfer, X. Periole, D. P. Tieleman, S. J. Marrink, "Improved Parameters for the Martini Coarse-Grained Protein Force Field", *Journal of Chemical Theory and Computation* **2013**, *9*, 687–697.

[68] S. O. Yesylevskyy, L. V. Schäfer, D. Sengupta, S. J. Marrink, "Polarizable Water Model for the Coarse-Grained MARTINI Force Field", *PLOS Computational Biology* **2010**, *6*, e1000810.

[69] J. Michalowsky, L. V. Schäfer, C. Holm, J. Smiatek, "A refined polarizable water model for the coarse-grained MARTINI force field with long-range electrostatic interactions", *The Journal of Chemical Physics* **2017**, *146*, 054501.

[70] T. A. Wassenaar, H. I. Ingólfsson, R. A. Böckmann, D. P. Tieleman, S. J. Marrink, "Computational Lipidomics with insane: A Versatile Tool for Generating Custom Membranes for Molecular Simulations", *Journal of Chemical Theory and Computation* **2015**, *11*, 2144–2155.

[71] F. Grunewald, G. Rossi, A. H. de Vries, S. J. Marrink, L. Monticelli, "Transferable MARTINI Model of Poly(ethylene Oxide)", *The Journal of Physical Chemistry B* **2018**, *122*, 7436–7449.

[72] J. Huang, A. D. MacKerell Jr, "CHARMM36 all-atom additive protein force field: Validation based on comparison to NMR data", *Journal of Computational Chemistry* **2013**, *34*, 2135–2145.

[73] A. Grossfield, "WHAM: The Weighted Histogram Analysis Method, 2.0.11", **2013**.

[74] R. C. Van Lehn, A. Alexander-Katz, "Membrane-Embedded Nanoparticles Induce Lipid Rearrangements Similar to Those Exhibited by Biological Membrane Proteins", *The Journal of Physical Chemistry B* **2014**, *118*, 12586–12598.

[75] S. Salassi, F. Simonelli, D. Bochicchio, R. Ferrando, G. Rossi, "Au Nanoparticles in Lipid Bilayers: A Comparison between Atomistic and Coarse-Grained Models", *The Journal of Physical Chemistry C* **2017**, *121*, 10927–10935.

[76] R. Patil, S. Das, A. Stanley, L. Yadav, A. Sudhakar, A. K. Varma, "Optimized Hydrophobic Interactions and Hydrogen Bonding at the Target-Ligand Interface Leads the Pathways of Drug-Designing", *PLOS ONE* **2010**, *5*, e12029.

[77] J. Payandeh, M. Volgraf, "Ligand binding at the protein–lipid interface: strategic considerations for drug design", *Nature Reviews Drug Discovery* **2021**, *20*, 710–722.

[78] F. Eisenhaber, P. Lijnzaad, P. Argos, C. Sander, M. Scharf, "The double cubic lattice method: Efficient approaches to numerical integration of surface area and volume and to dot surface contouring of molecular assemblies", *Journal of Computational Chemistry* **1995**, *16*, 273–284.

[79] O. Elimelech, O. Aviv, M. Oded, X. Peng, D. Harries, U. Banin, "Entropy of Branching Out: Linear versus Branched Alkylthiols Ligands on CdSe Nanocrystals", *ACS Nano* **2022**, *16*, 4308–4321.

[80] S. Yamashita, Y. Ito, H. Kamiya, Y. Okada, "Surface coverage can control the dispersibility of TiO2 and ZrO2 nanoparticles in hydrophobic solvents: Comparison of linear and branched ligands", *Advanced Powder Technology* **2024**, *35*, 104277.

[81] S. Ito, Y. Nakagawa, S. Yazawa, Y. Sasaki, S. Yajima, "Antifungal activity of alkyl gallates against plant pathogenic fungi", *Bioorganic & Medicinal Chemistry Letters* **2014**, *24*, 1812–1814.

[82] K. Hashiba, Y. Sato, M. Taguchi, S. Sakamoto, A. Otsu, Y. Maeda, T. Shishido, M. Murakawa, A. Okazaki, H. Harashima, "Branching Ionizable Lipids Can Enhance the Stability, Fusogenicity, and Functional Delivery of mRNA", *Small Science* **2023**, *3*, 2200071.

[83] D. Kim, D. W. Kim, H.-K. Lim, J. Jeon, H. Kim, H.-T. Jung, H. Lee, "Inhibited phase behavior of gas hydrates in graphene oxide: influences of surface and geometric constraints", *Physical Chemistry Chemical Physics* **2014**, *16*, 22717–22722.

[84] W. Shinoda, M. Mikami, T. Baba, M. Hato, "Molecular Dynamics Study on the Effect of Chain Branching on the Physical Properties of Lipid Bilayers: Structural Stability", *The Journal of Physical Chemistry B* **2003**, *107*, 14030–14035.

Chapter 4

Membrane mechanics influence ligand flipping between leaflets[1]

4.1 Introduction

The design and engineering of synthetic and biomedically-relevant soft materials has been a longstanding challenge, especially when many of them face the critical challenge of permeating across lipid membranes.[1] For example, the development of cyclic peptide drugs is hindered by poor membrane permeability and underexplored permeation mechanisms.[2, 3] This challenge is often interpreted in terms of thermodynamic barriers that lead to slow kinetics for membrane-crossing solutes and has thus posed a long-standing bottleneck for molecular simulations by diminishing sampling efficiency and statistical convergence.[4–8] Studies of inorganic NP permeation are similarly hindered, and while design rules for surface functionalization using organic ligands are not well-established, it has been widely accepted that physicochemical properties such as size, shape, hydrophobicity, and charge play a key role.[9]

Theoretical studies using classical MD simulations have typically used intermolecular distances (*e.g.*, COM distance between the NP and the lipid bilayer) to elucidate NP penetration into lipid membranes. However, it has been demonstrated that this singular collective variable poorly describes subsequent insertion into the core of the bilayer after initial adsorption, oftentimes leading to hysteresis and hidden energy barriers.[4, 5, 10–13] Instead of direct penetration into lipid membranes, a passive diffusion mechanism has also been proposed for ligand-functionalized NPs that are stably adsorbed to the outer leaflet of the bilayer. In this case, thermal fluctuations result in individual ligands stochastically flipping between

[1]This chapter is adapted with permission from Huang-Zhu and Van Lehn, Membrane mechanics influence ligand flipping between leaflets, manuscript in preparation. Supporting Information (SI) referenced will be available in the forthcoming publication.

leaflets[14–16]; however, protonation ability of ligands[16] and cholesterol presence[15] can also influence these flipping events.

Herein, we investigate potential descriptors that influence NP translocation across lipid bilayers assuming a passive diffusion mechanism where ligands iterative flip to achieve full insertion. The insertion of the ligand-coated AuNP was based on individual ligands flipping from the upper leaflet to the lower leaflet of the bilayer (ligand and lipid models shown in Figure 4.1A). Using coarse-grained (CG) models, we employed replica-exchange simulations to compute the free energy for flipping a single ligand. We focused on a series of AuNPs coated with ligands of different lipophilicities (log P), shown in Figure 4.1B, and at three different stages of insertion based on the ligand distribution between leaflets, shown in Figure 4.1C. The flipping of an individual ligand was determined using the distance along the z-axis (D_z) between its quaternary ammonium and the bilayer midplane, as shown in Figure 4.1D. We demonstrate that log P can influence the thermodynamics of ligand flipping, but that the degree of insertion dominates this event. We further show that ligand flipping is mediated by the coordination of polar or charged groups and that lipid membrane mechanics will drive ligand and lipid organization that facilitates this process. Our results suggest that the role of ligand end group chemistry becomes less significant after initial NP adsorption. Instead, lipid membrane mechanics dominate the NP translocation process by accommodating the NP and ligands into conformations that enable cooperative effects by polar species (*e.g.*, promoting a polar crossing pathway within the hydrophobic bulk of the bilayer for charged end groups). The computational workflow employed here is shown to alleviate some of the challenges associated with sampling permeation events of solutes into lipid membranes, and the findings discussed reveal important design rules that will support the future development of ligand-functionalized NPs.

4.2 Methods

4.2.1 Simulation parameters

Classical molecular dynamics (MD) simulations were performed using a leapfrog integrator with a timestep of 20 fs at a constant temperature of 300 K and 1 bar. The temperature was kept constant using a velocity-rescale thermostat with a time constant of 1.0 ps. The pressure was kept constant with semi-isotropic pressure coupling and a compressibility of 3 $\times$ 10^{-4} bar^{-1} in both the xy and z directions. The neighbor list was updated every 20 steps using the Verlet algorithm with a cutoff of 1.1 nm. Van der Waals interactions were modeled using a cutoff scheme with the potential shifted to zero at 1.1 nm. Electrostatic interactions were modeled using the Particle-Mesh-Ewald with the potential shifted to zero at 1.1 nm, a 4^{th} order interpolation, and a Fourier spacing of 0.12 nm. The dielectric constant was set to 2.5. All simulations were performed using GROMACS 2021.5[18] patched with PLUMED

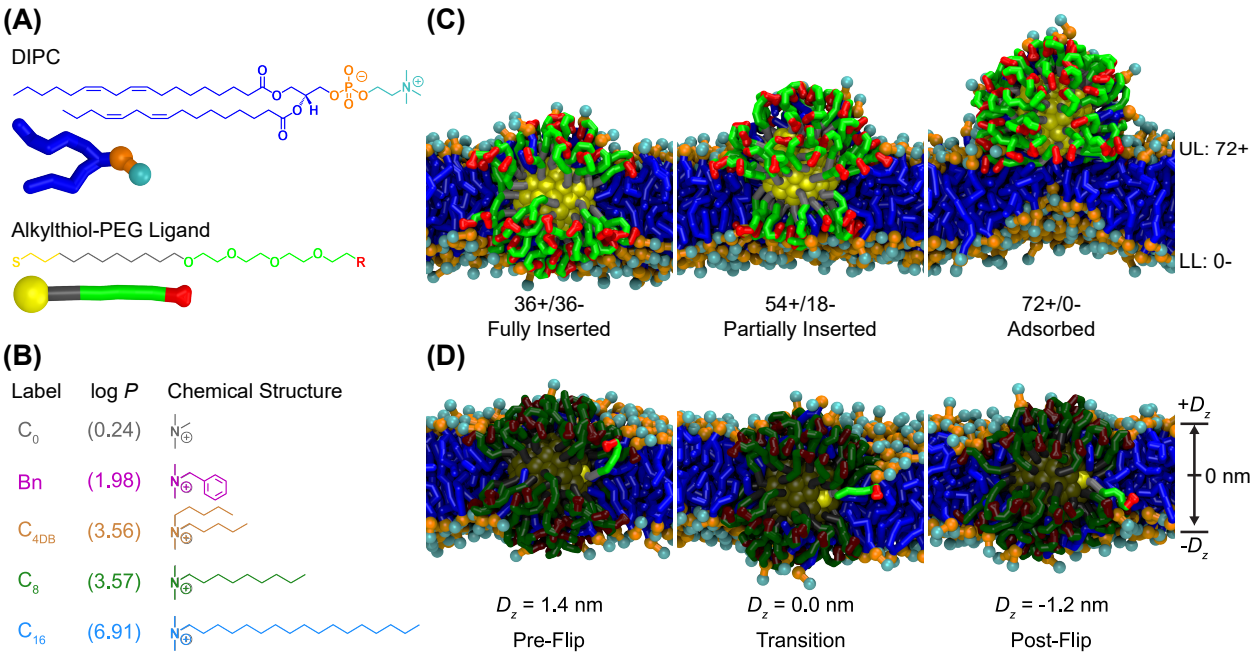


Figure 4.1: Description of systems and reaction coordinate. (A) Chemical structure and CG model of the zwitterionic 1,2-dilinoleoyl-*sn-glycero*-3-phosphocoline lipid and ligand used. (B) Summary of ligand end groups, or R groups, used for ligand-coated AuNPs. The log P values were extracted from ChemDraw version 21.0.0 using Crippen's method[17]. (C) Representative simulation snapshots for the three stages of insertion where the 72 ligands of the self-assembled monolayer are distributed between leaflets. The numbers accompanied by the + and - signs denote the number of ligands on the upper (UL) and lower (LL) leaflets, respectively. A fully inserted NP will have 36 ligands on the upper leaflet and 36 on the lower leaflet, whereas an adsorbed NP will have all 72 ligands on the upper leaflet and 0 on the lower leaflet. (D) Reaction coordinate for ligand flipping where D_z corresponds to the z-distance between the quaternary ammonium of the biased ligand and the bilayer midplane.

2.8.0[19]. All interactions were modeled using version 2.3 of the MARTINI force field[20–22] with the refined polarizable water model[23].

4.2.2 Description of systems

The coarse-grained models of the AuNPs were taken from our previous works.[24, 25] Briefly, each AuNP was modeled using a hollow gold core and a 72-ligand monolayer. The ligand is modeled after a 1-undecanethiol backbone (C5 beads) with a tetra(ethylene glycol) chain (EO beads[26]) and an end group based on a cationic quaternary amine (Q0 beads and additional based on substituent). Each AuNP was parameterized individually using a bottom-up approach; refer to our previous work for details.[24] The model membrane was modeled as a 16 nm × 16 nm bilayer composed of zwitterionic 1,2-dilinoleoyl-*sn-glycero*-3-phosphocoline (DIPC) lipids in a 20 nm tall box. See SI for more details.

4.2.3 System preparation and equilibration

To obtain the initial configurations corresponding to the adsorbed, partially inserted, and fully inserted states, we began by generating the desired ligand distribution on the NP in vacuum using steered MD simulations. For example, to achieve the 36+/36- configuration, the center-of-mass (COM) of the topmost 36 ligands was pulled upwards while the COM of the bottom 36 was pulled downwards with the NP core (S1 beads of the ligands) restrained using a 50 $\text{kJ} \cdot \text{mol}^{-1} \cdot \text{nm}^{-2}$ force constant. To ensure numerical stability, the steering was performed for 100,000 steps with a timestep of 5 fs (500 ps in total) using a force constant of 3,000 $\text{kJ} \cdot \text{mol}^{-1} \cdot \text{nm}^{-2}$ that was linearly interpolated (*i.e.*, stepwise increase from zero).

The AuNP was then positioned at a variable distance from the center of the membrane according to the ligand distribution: $\left(1 - \frac{\#LL\ ligands}{36\ ligands}\right) \times 4\ nm + 1.5 \times 0.47\ nm$. We used the *insane.py* script[27] to solvate the AuNP and the membrane. After solvation, the heterogeneity of the pre-configured ligand distribution led to asymmetric bilayer leaflets which we addressed by randomly selecting lipids from the leaflet with the largest number of lipids and deleting them.

To equilibrate the system in the *NPT* ensemble we used a Berendsen barostat with a time constant of 5.0 ps. We performed 20 stepwise simulations of 5,000 steps in which we gradually increased the timestep and released position restraints on the NP core and quaternary ammonium groups. We started with a timestep of 1 fs and a 1,000 $\text{kJ} \cdot \text{mol}^{-1} \cdot \text{nm}^{-2}$ force constant applied to the coordinates of the beads of the gold core and charged quaternary ammonium. At every iteration, we increased the timestep by 1 fs and decreased the position restraints by 50 $\text{kJ} \cdot \text{mol}^{-1} \cdot \text{nm}^{-2}$. Finally, a 150 ns simulation was performed without any restraints.

4.2.4 Defining the collective variable

From the final configuration of the equilibrated system, we identified a single ligand to bias based on a geometric criterion. We reasoned that from a physical perspective, the ligand most prone to flipping from the upper to the lower leaflet would be the one with its anchoring point (on the NP) closest to the membrane midplane. Thus, from the ligands distributed on the upper leaflet, we chose to bias the ligand whose S1 bead had the lowest value for its z-coordinate. We defined our collective variable, D_z, as the COM distance between the charged group of the biased ligand and the bilayer midplane. To calculate D_z using PLUMED, we computed the averaged z-distance from the quaternary amine to the phosphate head groups of the lipids that were outside of a cylinder with a 5 nm radius centered at the COM of the AuNP at any given timestep (*i.e.*, dynamic selection).

4.2.5 Ligand flipping steered molecular dynamics

After equilibration, ligand flipping between the upper and lower leaflets was simulated using four steered MD simulations. In the first steered MD simulation, D_z was restrained at its equilibrium value for 5 ns while the force constant was gradually increased from 0 to 2,500 $\text{kJ} \cdot \text{mol}^{-1} \cdot \text{nm}^{-2}$ and held constant. Immediately after, D_z was steered upwards to 3.5 nm. This was repeated during the second steered simulation but instead D_z was steered downwards to –3.5 nm. These two simulations represent the "forward pull". The final configuration of the second steered simulation was then used to perform a 10 ns unbiased simulation to relax the lipid membrane. After which the first two steered MD simulations were repeated, effectively simulating the same ligand flipping back and representing the "backward pull". The pull rate for these four steered MD simulations was 10,000 $\text{ps} \cdot \text{nm}^{-1}$ and configurations were sampled every 500 ps – simulation times for each individual simulation varied.

4.2.6 Replica-exchange umbrella sampling

We implemented a replica-exchange approach combined with umbrella sampling to compute the free energy for ligand flipping. Unlike traditional umbrella sampling methodologies that rely only on configurations generated from a forward steered simulation, replica-exchange improves sampling efficiency by incorporating a mix of configurations generated from both forward and backward pulling simulations to ensure continuity along the reaction coordinate and minimize hysteresis. Rather than attempting to exchange replicas based on the Hamiltonian or temperature of each independent window, we attempt exchanges based on their potential energy.[28]

Here, we first define 56 windows along our reaction coordinate, each with D_z spaced 0.1 nm apart. Rather than selecting the initial configuration for each window only from the forward pull, we instead alternate between forward and backward pulling simulations. This means that we choose the first window with $D_z = 3.5$ nm will be initialized with a configuration from the forward pull, but the next window with $D_z = 3.4$ nm will use a configuration from the backward pull, and so on. Alternating between forward and backward pulling simulations is essential for this replica-exchange methodology to work effectively, particularly for when the AuNP is an adsorbed state due to the strong asymmetry in ligand distribution. For example, in a 72+/0- state, during the forward pull, as the ligand crosses the transmembrane region (D_z decreases) it remains bound to the upper leaflet until it detaches near the midplane. In contrast, during the backward pull, the ligand will cross back to the upper leaflet (D_z increases) while remaining bound to the lower leaflet and will not detach even after crossing back the midplane. Replica-exchange thus alleviates this by exchanging the high-energy states along the reaction coordinate. This also addresses sampling near the

free energy barrier – at the midplane ($D_z = 0$), the biased ligand can, in theory, be bound to either leaflet and replica-exchange allows us to sample these alternating configurations that have been traditionally difficult to sample without assuming leaflet connectivity[29].

Production simulations were performed in the NPT ensemble with a Parrinello-Rahman barostat and a time constant of 12.0 ps while restraining D_z with a force constant of 500 $\mathrm{kJ \cdot mol^{-1} \cdot nm^{-2}}$. An initial 30 ns simulation, without exchange attempts, was performed as equilibration and excluded from the analyses. Subsequently, a 50 ns sampling simulation, with exchange attempts every 100 steps and a sampling frequency of 50 steps, was performed – the initial 5 ns were discarded, and the last 45 ns were used for analyses. We used the weighted histogram analysis method (WHAM)[30] to resolve the free energy as a function of D_z. To address error propagation when calculating the uncertainty for the free energy profiles, we computed statistical uncertainty using the standard deviation of the numerical derivatives of the free energy curves.[31]

The calculations for the isolated ligand (Figure 4.2) were based on the corresponding AuNP. We equilibrated the AuNP and then removed the rest of the AuNP leaving only the ligand chosen to be biased. Topology files were adjusted accordingly, and the REUS workflow was performed as described previously starting with NPT equilibration. Analogously, the calculations for the isolated end group (Figure 4.2) were based on the corresponding isolated ligand. We performed the same steps as for the isolated ligand, this time removing the ligand backbone to obtain solely the charged end group.

4.3 Results and Discussion

4.3.1 Nanoparticle core induces asymmetry in charged group translocation

We began this work by establishing a replica-exchange simulation workflow to address previously reported challenges related to the translocation of charged species across lipid bilayers.[29, 32–35] Briefly, using steered MD simulations to move a charged molecule from one leaflet to another can lead to asymmetric free energy profiles in thermodynamic calculations as the molecule remains electrostatically bound to the originating leaflet. Unbinding or detachment can occur deep within the nonpolar region of the lipid bilayer (*i.e.*, lipid tails) upon which immediate binding or attachment to the opposite leaflet takes place, the latter taking place at much faster time scales than the former. Sufficient bilayer relaxation time is thus needed for statistical convergence and is strongly coupled to solute permeation. We sought to alleviate bilayer relaxation by using replica-exchange simulations as they have been used to improve sampling efficiency in studies for peptide translocation[35], solute permeation[36], and membrane protein loop flipping[37]. While replica-exchange simulations are typically based on replicas with different temperatures or Hamiltonians, here we alternate configu-

rations taken from forward and backward steered MD simulations. With this approach, we primarily target statistical convergence and sampling efficiency near the transition state where we expect equal sampling of states in which the charged quaternary ammonium is bound to either the upper leaflet or lower leaflet.

We first tested the robustness of our methods by performing replica-exchange simulations combined with umbrella sampling (REUS) to compute the free energy of translocation for an isolated R group, a singular free ligand, and an individual ligand of a fully inserted AuNP (36+/36- from Figure 4.1C). Since we rationalize ligand design and NP engineering in terms of building blocks, we concluded that simulating the translocation of the isolated R group and a singular free ligand were reasonable control simulations to compare against. Mainly, they are simpler geometries that still allow us to probe end group effects while minimizing the bias introduced by a NP embedded within the bilayer core. In Figure 4.2 we show the computed free energy profiles for the C_0, Bn, C_8, and C_{16} end group chemistries.

We show that the free energy profiles are generally symmetric with free energy barriers close to the bilayer midplane ($D_z = 0.0$ nm). While most free energy profiles were consistent across all replicas within each of the end group chemistries and each of the systems, we observed a few outliers primarily for the NP systems. Specifically, we observed larger variation in symmetry that is potentially attributed to the challenges we discussed previously with regard to the leaflet connectivity of the translocating group. As D_z decreases to negative values (past the midplane) without detaching from the upper leaflet, the free energy barrier for translocation increases. This is thermodynamically consistent since the charged head groups of coordinated lipids are pulled into a nonpolar region while inducing local membrane deformations. The translocation free energy (*i.e.*, the free energy difference between the two local minima) is then more prone to error due to longer timescales required for the bilayer to relax, we thus focus the rest of this discussion on the free energy barriers for translocation. This challenge can be addressed in conventional umbrella sampling by choosing configurations a

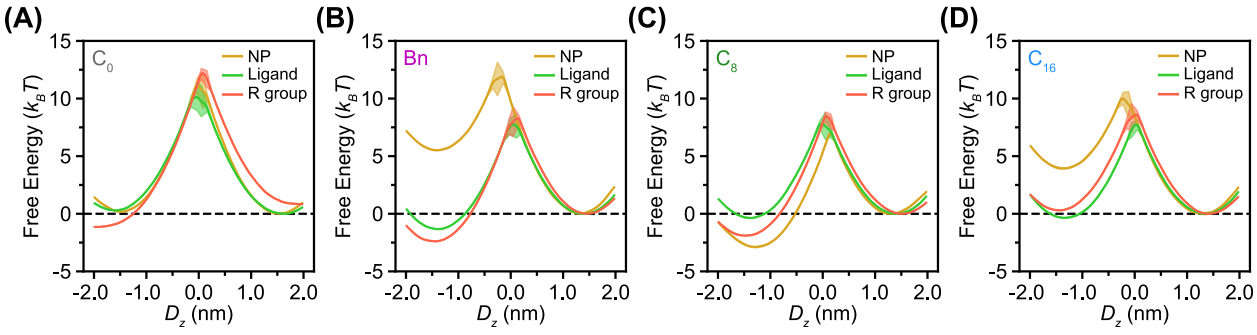


Figure 4.2: Free energy profiles for the translocation of (A) C_0, (B) Bn, (C) C_8, (D) C_{16} chemical motifs across the lipid bilayer.

priori that satisfy the perceived ligand connectivity (*i.e.*, detachment from the upper leaflet at the midplane and attachment to the lower leaflet past it).[32] However, this approach introduces bias by making assumptions about the translocation mechanism.

The fact that we observe higher symmetry in free energy profiles for simpler geometries (*i.e.*, isolated R group and singular individual ligand) suggests that the REUS approach implemented here can be used effectively to study the translocation of charged species across lipid membranes. Furthermore, this methodological framework does not assume ligand connectivity at the transition state, relying instead on the Hamiltonian along neighboring windows of the chosen collective variable. In general, the variations observed for the NP systems demonstrate that ligand-coated NPs can potentially diffuse passively across lipid membranes through ligand flipping mechanisms, and with reasonable thermodynamic barriers, but also suggest that additional driving forces play a role in full NP translocation.

The data in Figure 4.2 also reveal differences in translocation free energies between different R groups. For the most lipophilic R groups (Bn, C_8, and C_{16}), the translocation barriers relative to each other are statistically equivalent. The only notable difference is the C_0 R group, which we expected to be the one with the highest free energy barriers due to the fully exposed charge. In contrast, the remaining R groups have higher log P due to the lipophilic alkyl groups which support the partitioning into the hydrophobic bulk of the bilayer which reduces the free energy barrier for translocation.[38] These relative differences are consistent with the partitioning free energies for amino acid side chains.[38] For example, the free energy for a lysine side chain to partition into a DOPC bilayer is ∼20 kJ/mol lower compared to glutamic acid (less bulky and more hydrophilic) and ∼10 kJ/mol lower compared to arginine (more hydrophilic).[38] Neutral isoleucine and phenylalanine side chains also exhibit similar partitioning free energies (∼18 kJ/mol), although the latter being bulkier and more lipophilic shows a local minimum closer to the headgroup region of the bilayer.[38] While these values are reported for simulations with DOPC bilayers and the regular MARTINI water model (non-polarizable), the trends are expected to remain the same even though numerical values can change.

4.3.2 Ligand leaflet distribution influences free energies of ligand flipping

Since the free energy barriers for translocation across end group chemistry were within error of each other, revealing that it plays a weaker role in NP translocation, we hypothesized that the degree of insertion of the NP could modulate the thermodynamics of this process. We rationalized this hypothesis on previous works that report large free energy barriers for the translocation of anionic ligands across lipid bilayers computed from metadynamics simulations[14–16] and long-timescale unbiased simulations where these ligands flip spontaneously

and do not flip back[14], suggesting irreversible NP translocation. To probe this question, we generated three initial configurations of the NPs at different insertion stages – determined by the distribution of ligands across the upper and lower leaflets of the lipid membrane as shown in Figure 4.1C. We performed REUS to compute the free energy of flipping a single ligand for the C_0, Bn, C_8, and C_{16} end group chemistries with the NP in adsorbed, partially inserted, and fully inserted states.

The resulting free energy profiles are shown in Figure 4.3 and reveal that the degree of NP insertion indeed modulates the thermodynamics of single ligand flipping. Specifically, the free energy barrier for translocating a single ligand increases with the degree of NP insertion with the end group chemistry having a weaker effect in modulating the thermodynamics. However, among these data, the translocation of a single ligand with a Bn R group when the NP is fully adsorbed (*i.e.*, 72+/0- ligand distribution) stands out as a seemingly barrierless process in contrast to the C_0, C_8, and C_{16} ligands (Figure 4.1A). A barrierless transition, particularly for the first ligand flipping event, implies that we should observe it in unbiased simulations, which we did not. We thus focused our subsequent analyses on this case, specifically comparing it to the C_0 ligand as our reference control due to its fully exposed charge. Notably, the free energy barrier for translocating the C_8 ligand is similar regardless of NP insertion degree ($\sim$5 k_BT) while the barrier for the C_{16} ligand increases with NP insertion degree, similarly to the C_0 ligand. An energetic barrier that remains the same, as opposed to increasing or decreasing, for subsequent ligand flipping events as the NP crosses the lipid membrane, suggests that such NP would have a higher probability of translocating into the cytosolic environment of cells. These thermodynamic trends, where the free energy barrier for C_0, Bn, and C_{16} ligand translocation increases with NP insertion degree but remains constant for the C_8 ligand, are not dissimilar to previous studies where medium-

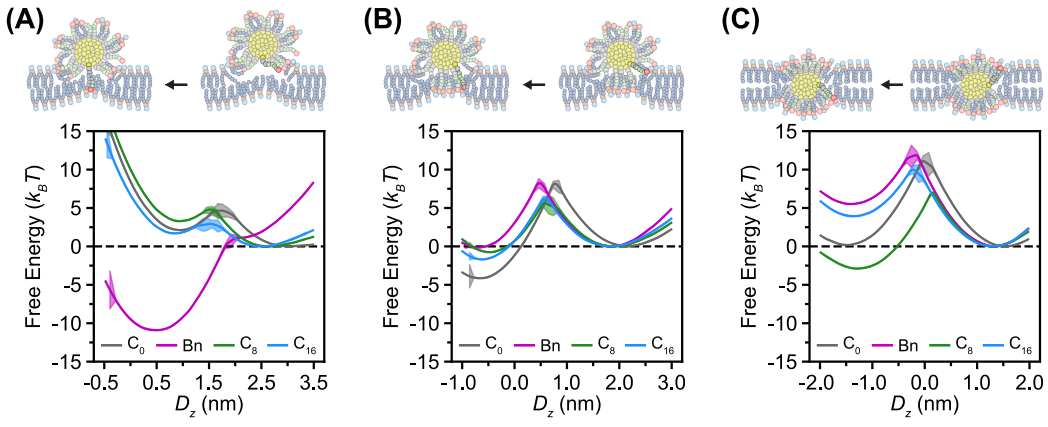


Figure 4.3: Free energy profiles for the translocation of a single ligand across the lipid bilayer for AuNPs in (A) adsorbed, (B) partially inserted, and (C) fully inserted states. Uncertainty was computed as described in the Methods section.

chain lipid-conjugated fluoresceins exhibited higher cellular uptake versus fluoresceins with short-chain, long-chain, or aromatic conjugates.[39]

4.3.3 Transmembrane polar pathways facilitate charged group translocation

Since the chemical nature of the translocating species does not appear to strongly modulate the ligand flipping process (with the exception of the Bn end group), we investigated the coordination of the translocating charged group with other species (N_{coord}). In Figure 4.4 we quantify N_{coord} for water, the lipids' phosphate head group, and chloride ions along at three key stages of the reaction coordinate (pre-flip, transition, and post-flip) when the NP is at different stages of insertion (adsorbed, partially inserted, and fully inserted). Here, the pre-flip state corresponds to the local free energy minimum before the ligand is flipped, the transition state corresponds to the free energy barrier, and the post-flip state corresponds to the local free energy minimum after the ligand is flipped. We describe two key observations that support the hypothesis that ligand flipping is facilitated by cooperative effects between the translocating species and its local environment, supporting the hypothesis that full NP translocation across lipid membranes is not necessarily a single step process. First, we show that water coordination appears to drive the translocation process, and second, we argue that subsequent ligand flipping for NP translocation is enabled by the formation of a charged pathway within the nonpolar region of lipid membranes.

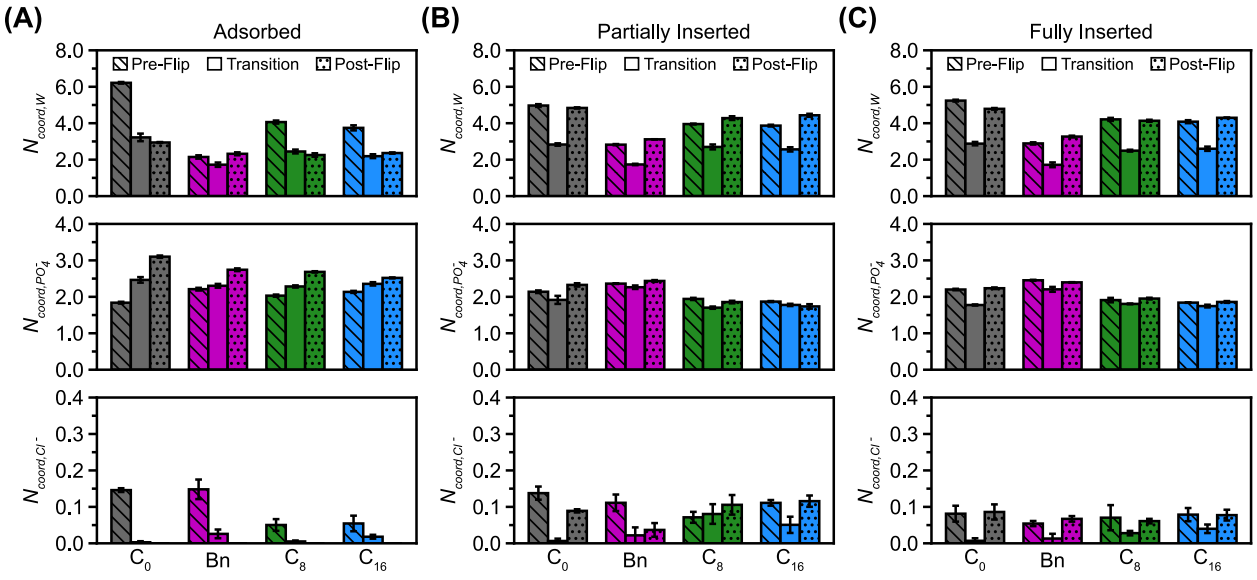


Figure 4.4: Coordination of cationic quaternary ammonium with water and negatively charged species for AuNPs in (A) adsorbed, (B) partially inserted, and (C) fully inserted states. Uncertainty was computed as the standard error between three replicates.

When the NP is adsorbed to the outer leaflet (Figure 4.4A), with no ligand having crossed the hydrophobic bulk of the lipid bilayer, the biased charged group is highly coordinated with water. For the C_0, C_8, and C_{16} ligands, the number of coordinated water decreases by approximately 50% at the transition state (*i.e.*, charged group crossing the midplane). The solvation shell of the charged group is not restored as observed by the post-flip values of $N_{coord,W}$. In contrast, the Bn ligand shows that (1) its charged group is significantly less hydrated than the other ligands in its pre-flip state, (2) water coordination only decreases slightly at the transition state, and (3) its solvation shell is only weakly disrupted and is restored post-flip. Similarly, for the Bn ligand charged group, the change in N_{coord,PO_4^-} between the pre-flip and transition states is negligible relative to that of the C_0, C_8, and C_{16} ligands. Surprisingly, while the Bn ligand shows the lowest charged group hydration, it has high chloride ion coordination on the same level as the C_0 ligand (highest charged group hydration) whereas the charged group of the C_8 and C_{16} ligands have N_{coord,Cl^-} values of less than half of those of the Bn and C_0 ligands. Such low values for the C_8 and C_{16} ligands are attributed to the charged groups being buried deeper in the lipid tail region due to the more lipophilic end groups whereas the Bn ligand coordinates to the lipid head groups through choline- interactions[21] and the C_0 ligand partitions strongly into solvent due to its fully exposed charge. Surprisingly, Figures 4B and 4C reveal that water coordination to the translocating charged group is invariant to the NP being partially inserted or fully inserted in the bilayer, suggesting that water cooperativity diminishes after a few initial ligands flip. We interpret these changes, or lack thereof, to the Bn ligand being in a lower free energy conformation due to a lower hydration which results in smaller dehydration free energies as the charged group crosses the nonpolar region of the lipid bilayer, which is consistent with the apparent barrierless flipping in Figure 4.3A, although probably underestimated due to the coarse-grained nature of the force field used.

With water becoming a weaker driving force along the NP translocation pathway, we hypothesized that coordination with oppositely charged species (*i.e.*, the ligand's cationic quaternary ammonium with either lipid phosphate head groups or chloride ions) may provide insight into how N_{coord} influences the ligand translocation process at later stages of NP insertion. While partial insertion or full insertion does not significantly influence N_{coord,PO_4^-} (Figures 4B and 4C), the coordination of chloride ions N_{coord,Cl^-} appears to mediate the transition state. Specifically, the C_8 and C_{16} ligands show their charged group coordinated with chloride ions at the transition state while the C_0 and Bn ligands show almost no chloride ion coordination. We relate this coordination to the formation of a charged pathway in which the C_8 and C_{16} ligands induce local bilayer defects and lipid reorganization that increase the ability of chloride ions to reach the vicinity of the translocating charged group and stabilize the ionic repulsions of the lipid head groups. This charge-neutralizing effect then lowers the free energy penalty for the charged group to unbind from the upper leaflet, cross the lipid

membrane, and restore its coordination with negatively charged groups. We note that these observations, although clear for the partially inserted state (Figure 4.4B), they are less so for the fully inserted state (Figure 4.4C) potentially due to a more relaxed bilayer where localized defects and ionic effects are better distributed across the whole membrane. These observations are comparable to some observations in recent work that employed transition path sampling guided by artificial intelligence for molecular mechanism discovery.[40] In this study, lipid flip-flop was studied and one mechanism, at the all-atom scale, was found to result in water nanowires forming within the transmembrane region and then collapsing into nanodroplets that establish a passageway for the flip-flop. However, at the coarse-grained scale, a dry lipid flip-flop mechanism predominates.

4.3.4 Ligand splaying induce lipid reorganization

As we computed the coordination of different groups, we qualitatively monitored lipid membrane mechanics, mainly for the REUS windows corresponding to the pre-flip and post-flip states (*i.e.*, local minima). We identified a characteristic adsorbed state for the Bn AuNP where the interfacial ligands (*i.e.*, ligands in the lower half of the NP and in contact with transmembrane lipids) were splayed radially promoting lateral diffusion of lipids within the upper leaflet. This lipid reorganization then forced lipids from the lower leaflet to come into contact with the NP core, pulling the NP into the transmembrane region and inducing a local thinning effect on the bilayer. Such behavior was not observed in the other AuNPs; the C_0, C_8, and C_{16} ligands assumed conformations with a more spherical distribution forcing a high-energy lipid bridge that connects the AuNP and the transmembrane region of the bilayer[24]. We show representative simulation snapshots of these states in Figure 4.5, in addition to number density plots for the AuNPs and the lipids. The number density plot for the AuNP in Figure 4.5B confirms the splayed conformations that the Bn ligands assume in the pre-flip state, which contrasts with the number density plots in Figures 5A, 5C, and 5D that show ligands assuming more spherical distributions minimizing exposure of the AuNP core to the bilayer transmembrane region. The number density plots for the lipids show that the Bn AuNP indeed thins out the lipid membrane at the AuNP-membrane interface, specifically right below the AuNP core (*i.e.*, radial distances smaller than 2.0 nm), as expected from our qualitative observations. Interestingly, as the alkyl chain length increases, lipids are excluded from the AuNP-membrane interface without any thinning effect. Instead, the longer alkyl chains replace the excluded lipids in this region with the C_{16} ligands inducing a stronger effect as they significantly minimize the hydrophobic mismatch (*i.e.*, similar length as the lipid tails) present with the C_8 ligands (*i.e.*, shorter length than the lipid tails). These data show that chemical descriptors, such as the log P of ligand end groups, do not modulate AuNP translocation through iterative ligand flipping to a meaningful extent and

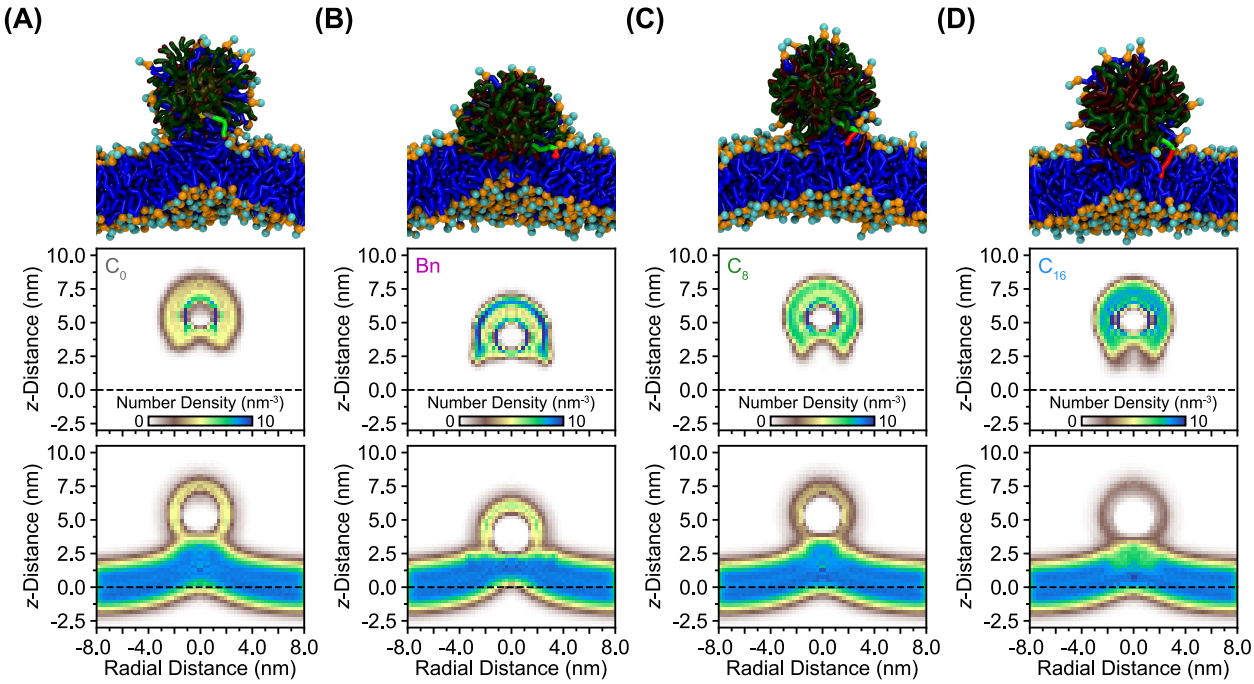


Figure 4.5: Number density for (A) C_0, (B) Bn, (C) C_8, (D) C_{16} AuNPs and lipids in an adsorbed and pre-flip state. 2D histograms are mirrored for negative values of the radial distance for visual purposes. Bins were 0.26 nm tall and 0.26 nm wide.

that instead, lipid membrane mechanics, such as lipid reorganization, will accommodate the AuNP such that its ligand charged groups can reach the opposite leaflet with weaker repulsive forces. Moreover, the number density of the lipids reveals different degrees of lipid extraction for each AuNP which is also expected to influence the thermodynamics for subsequent NP internalization and inevitably affects the mechanical structure of the lipid membrane. This mechanistic insight explains the seemingly barrierless translocation of the Bn ligand charged group in addition to why it is less hydrated, and how its local environment is minimally perturbed along the reaction coordinate relative to the C_0, C_8, and C_{16} ligands.

4.3.5 Metastability with local membrane thinning minimizes increase in post-flip deformation

The mechanics of cell membranes are of extreme relevance in cellular transport of small molecules, particularly in processes that are dominated by membrane fusion. While most studies have focused on the NP as the active participant in NP-membrane interactions, a few have sought to elucidate how membrane properties influence nano–bio interactions[41, 42]. To further show that lipid membrane mechanics influence the translocation of individual ligands, we sought to quantify the extent to which local lipid membrane deformation influences individual ligand translocation. We achieved this by computing local curvature

for each leaflet independently. While a lipid bilayer membrane is more commonly approximated as a single thin sheet, such approximations would lead to inaccurate descriptions of membrane curvature at a molecular scale due to lipid extraction as the NP enters the transmembrane region. Furthermore, since the translocation of the NP naturally induces mechanical asymmetry on the entrance leaflet, analyzing each leaflet independently of each other leads to more physically relevant interpretations.

In Figure 4.6 we show number density plots of the lipid phosphate head groups for the C_0 and Bn AuNPs in their pre-flip and post-flip states. Each leaflet was fitted individually using a stretched exponential fit to derive a functional form that describes curvature.[43, 44] These data show that the C_0 AuNP, in a pre-flip state , fluctuates along the normal of the bilayer since we observe segregated densities within a radial distance of 2 nm from the center of the NP. Such fluctuations are consistent with previously observed desorption mechanisms of cationic ligand-coated AuNPs through metadynamics.[24] The first ligand flipping event then induces a highly localized deformation at the NP-membrane interface with an increased density of phosphate head groups. The flipped ligand acts as an anchor that pinches the lower leaflet and increases the insertion degree of the NP into the lipid membrane. In the case of the Bn AuNP, the features of the histograms between the pre-flip and post-flip states are equivalent with only a slightly increased density at the NP-membrane interface after the first ligand flips. Therefore, in the metastable pre-flip state, the Bn ligands will have increased exposure to the lower leaflet, in contrast to the C_0 ligands, due to a thermodynamically favorable deformation that sinks the NP core deeper into the transmembrane region. This

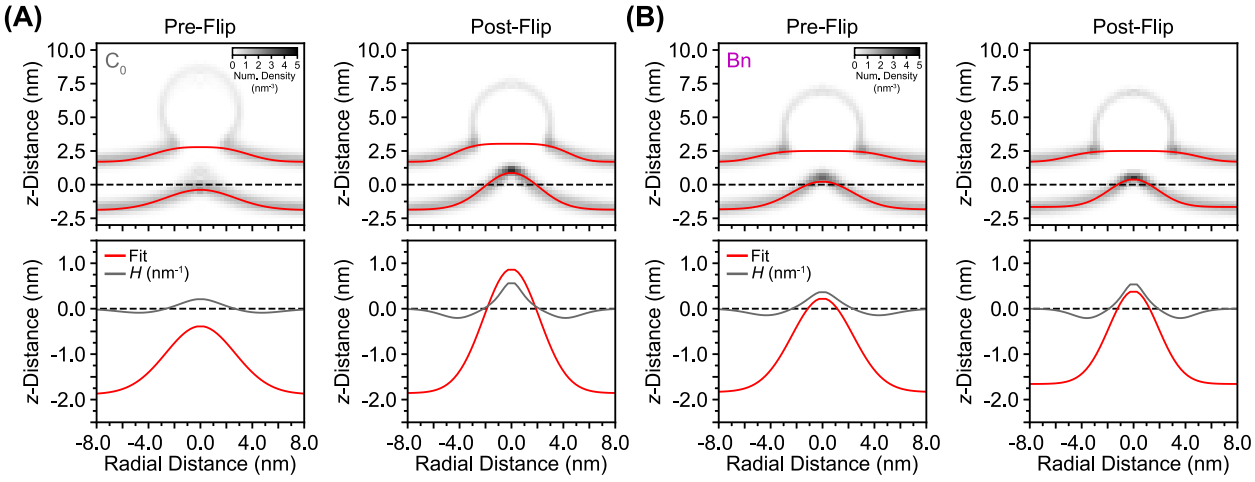


Figure 4.6: Ligand flipping perturbs leaflet curvature after flipping for the (A) C_0 and (B) Bn AuNPs. Number densities correspond to the lipid phosphate head groups as representations of each leaflet and are mirrored for negative values of the radial distance for visual purposes. Bins were 0.26 nm tall and 0.26 nm wide. The maximum number density data of each bin was used to fit a stretched exponential curve with data mirrored on x-axis.

state is thermodynamically unfavorable for the C_0 AuNP because the ligands are unable to displace lipids from the upper leaflet laterally and thus remain at the NP-membrane interface acting as an additional barrier that ligands must cross to become anchored to the lower leaflet.

Using the analytical expressions derived for each leaflet, we then quantified the local mean curvature, H, for the lower leaflet and show that the Bn AuNP only shows a 47% increase in maximum curvature compared to the C_0 AuNP with a 168% increase. These differences further suggest that lipid reorganization and thus membrane mechanics play an important role in the NP internalization process. That is, the lateral diffusion of lipids forces a deeper inclusion of the NP in the transmembrane region and minimizes localized membrane deformations.

To further investigate molecular-scale interactions in relation to membrane curvature we computed approximations of leaflet-resolved bending energies following Helfrich theory constrained solely to local mean curvature (*i.e.*, no spontaneous curvature or Gaussian curvature). In Figure 4.7A and 7B we computed the bending energy of each leaflet using their local mean curvature (see SI for additional details).[42] Quantifying the bending energies for each leaflet in their pre-flip and post-flip states further shows negligible differences after the translocation of the first ligand for the Bn AuNP. In contrast, the C_0, C_8, and C_{16} AuNPs show an increase in bending energies in their post-flip states for both leaflets.

We then computed the fold-change in bending energy for each leaflet in Figure 4.7C to show that only the Bn ligand end group does not lead to an increase in bending energies, and that the C_0, C_8, and C_{16} ligands induce lipid reorganization in both leaflets that increase their bending energy. We interpret these data as the energetic penalty associated with the first ligand flipping since the bending energy is related to how strongly each leaflet is

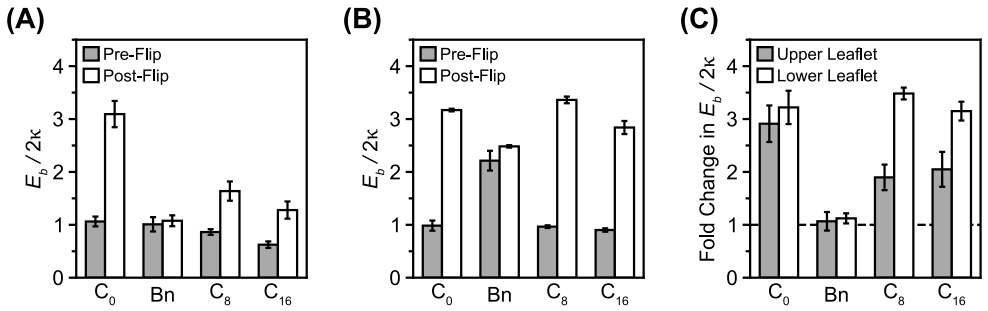


Figure 4.7: Leaflet-resolved bending energies for the (A) upper leaflet and (B) lower leaflet. Uncertainty was computed as the standard error between three replicates. Note that values were computed by integrating only the positive values of the radial distances. The fold-change in (C) was computed by normalizing post-flip values by pre-flip value for each leaflet. Uncertainty was computed by error propagation. A fold-change value of unity suggests that bending energy is invariant to ligand flipping.

deformed. While these bending energies are not explicitly related to free energy barriers for ligand translocation, they support the hypothesis that lipid membrane mechanics can dominate these events over chemical properties of ligand end groups.

4.3.6 Branched ligand end groups influence membrane mechanics

Based on our observations, we hypothesized that AuNPs capable of inducing lateral diffusion of lipids that alter the mechanical structure of the lipid membrane to incorporate the NP core within the transmembrane region can have ligands that flip with lower energetic barriers. In our previous work, we demonstrated that alkyl chain architecture can lower free energy barriers to adsorption by disrupting the ligand monolayer and increasing ligand end group protrusions.[25] Thus, we selected AuNPs coated with ligands whose alkyl end groups are highly branched and that, in a fully adsorbed state, exhibit qualitative features consistent with those of the Bn AuNP (*i.e.*, ligands splayed and NP core embedded deep enough to come into contact with lower leaflet lipids).

To test our hypothesis, we applied our methods to two AuNPs whose ligands have quaternary amines with three alkyl chains (*i.e.*, triple-branched). However, during equilibration we observed unbiased ligand translocation (see SI) after lipids diffused laterally and allowed the NP to embed deeper into the transmembrane region. These observations agree with our hypothesis but limited further analyses on these AuNPs. Instead, we selected the AuNP whose ligand end group is composed of two butyl chains in a branched architecture labeled as C_{4DB} in Figure 4.1B. We chose this ligand because its lipophilicity is similar to the C_8 AuNP and allows for a more direct comparison.

Figure 4.8 shows the free energy profiles for flipping a single ligand for the Bn, C_{4DB}, and C_8 AuNPs in the adsorbed, partially inserted, and fully inserted states. More specifically, we observe that the C_{4DB} AuNP shows lower free energy barriers for flipping a single ligand compared to the C_8 AuNP with similar lipophilicity. While the mechanical features of the C_{4DB} AuNP, specifically how deeply the NP is embedded into the membrane core, are more comparable to the C_8 AuNP, it shows a higher density of lipids on the ligand monolayer for the adsorbed state (see SI). This lipid reorganization leading lower free energy barriers is not surprising since it points to a decrease in the free energy as it minimizes exposure of nonpolar groups to water. Altogether, these data demonstrate that ligand end group chemistry, while critical for initial NP adsorption to lipid membranes, are weaker driving forces for subsequent internalization into the cytosol and that membrane mechanics will modulate the translocation of cationic ligands across the lipid bilayer.

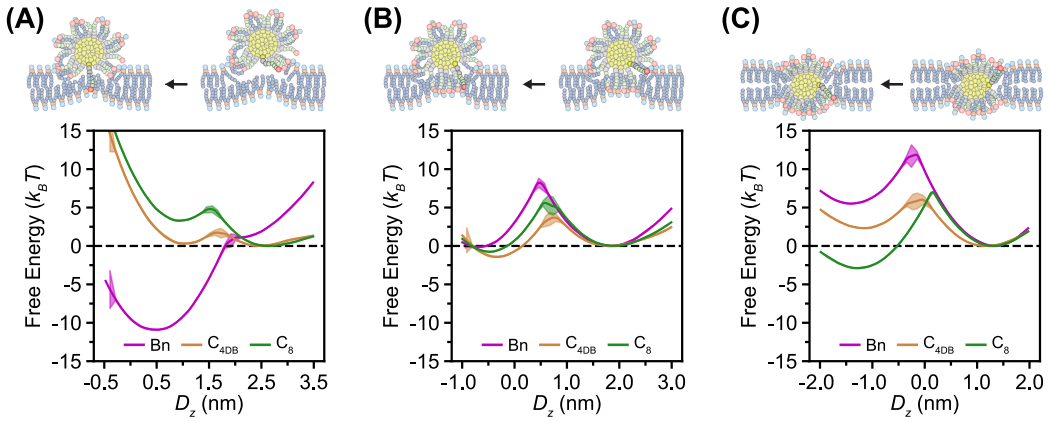


Figure 4.8: Effects of alkyl end group branching on the free energies of translocation for AuNPs in (A) adsorbed, (B) partially inserted, and (C) fully inserted states. Uncertainty was computed as described in the Methods section. Data for Bn and C_8 AuNPs are the same as in Figure 4.3 and are plotted against data for the C4DB AuNP for comparison.

4.4 Conclusions

In this work, we systematically studied ligand end group translocation of cationic AuNPs across lipid membranes using coarse-grained simulations. By implementing replica-exchange methods, we address sampling challenges that arise when modeling the permeation of hydrophilic solute through nonpolar environments, especially for ligands coated on NP surfaces. While ligand chemistry has been shown to be a strong driving force for the initial NP adsorption to biomembranes, its relevance in subsequent internalization is less well-understood. Assuming that AuNP translocation occurs through iterative ligand flipping events, our results demonstrate that lipid membrane mechanics and ligand distribution between leaflets dominate the thermodynamics of this process over chemical descriptors, such as log P. Instead, lipid rearrangement within the lipid membrane and lipid extraction can cause AuNPs to become embedded deeper within the lipid bilayer hydrophobic core while facilitating polar or electrostatically charged pathways through which positively charged ligand end groups can cross with lower free energy barriers. We also validate our initial hypotheses by performing additional calculations using AuNPs coated ligands that have branched alkyl end groups. At similar end group lipophilicities, the branched ligands will cross the lipid bilayer with lower free energy barriers, or even spontaneously for triple-branched motifs, while showing significant differences in lipid organization within the membrane and lipid extraction onto the surface of the AuNP. The methods presented and results discussed here provide a computational framework to study the mechanisms and thermodynamics of membrane permeation of solutes while addressing sampling challenges. Furthermore, they pave the way for future studies using multicomponent lipid bilayers as more biologically relevant systems since such models will exhibit different membrane mechanical properties (*e.g.*, leaflet asymmetry, lipid

composition, different phases). In future work, we will perform additional simulations instead focusing on the lipids as active participants by elucidating the effects of lipid properties such as tail length, tail saturation, and head group charge while making improvements on the replica-exchange algorithm to maximize sampling efficiency. Overall, this study highlights the importance of designing membrane-active materials that are not only effective in adsorbing to the surface of lipid membranes, but that are also capable to cross the hydrophobic transmembrane region.

References

[1] Y. Kumar, A. S. K. Sinha, K. D. P. Nigam, D. Dwivedi, J. S. Sangwai, "Functionalized nanoparticles: Tailoring properties through surface energetics and coordination chemistry for advanced biomedical applications", *Nanoscale* **2023**, *15*, 6075–6104.

[2] M. Sugita, S. Sugiyama, T. Fujie, Y. Yoshikawa, K. Yanagisawa, M. Ohue, Y. Akiyama, "Large-Scale Membrane Permeability Prediction of Cyclic Peptides Crossing a Lipid Bilayer Based on Enhanced Sampling Molecular Dynamics Simulations", *Journal of Chemical Information and Modeling* **2021**, *61*, 3681–3695.

[3] M. Sugita, T. Fujie, K. Yanagisawa, M. Ohue, Y. Akiyama, "Lipid Composition Is Critical for Accurate Membrane Permeability Prediction of Cyclic Peptides by Molecular Dynamics Simulations", *Journal of Chemical Information and Modeling* **2022**, *62*, 4549–4560.

[4] C. Neale, W. F. D. Bennett, D. P. Tieleman, R. Pomès, "Statistical Convergence of Equilibrium Properties in Simulations of Molecular Solutes Embedded in Lipid Bilayers", *Journal of Chemical Theory and Computation* **2011**, *7*, 4175–4188.

[5] H. A. L. Filipe, M. J. Moreno, T. Róg, I. Vattulainen, L. M. S. Loura, "How To Tackle the Issues in Free Energy Simulations of Long Amphiphiles Interacting with Lipid Membranes: Convergence and Local Membrane Deformations", *The Journal of Physical Chemistry B* **2014**, *118*, 3572–3581.

[6] D. P. Tieleman, S.-J. Marrink, "Lipids Out of Equilibrium: Energetics of Desorption and Pore Mediated Flip-Flop", *Journal of the American Chemical Society* **2006**, *128*, 12462–12467.

[7] W. F. D. Bennett, J. L. MacCallum, D. P. Tieleman, "Thermodynamic Analysis of the Effect of Cholesterol on Dipalmitoylphosphatidylcholine Lipid Membranes", *Journal of the American Chemical Society* **2009**, *131*, 1972–1978.

[8] N. Sapay, W. F. D. Bennett, D. P. Tieleman, "Thermodynamics of flip-flop and desorption for a systematic series of phosphatidylcholine lipids", *Soft Matter* **2009**, *5*, 3295–3302.

[9] X. Zhang, G. Ma, W. Wei, "Simulation of nanoparticles interacting with a cell membrane: probing the structural basis and potential biomedical application", *NPG Asia Materials* **2021**, *13*, 52.

[10] F. Lolicato, L. Joly, H. Martinez-Seara, G. Fragneto, E. Scoppola, F. Baldelli Bombelli, I. Vattulainen, J. Akola, M. Maccarini, "The Role of Temperature and Lipid Charge on Intake/Uptake of Cationic Gold Nanoparticles into Lipid Bilayers", *Small* **2019**, *15*, 1805046.

[11] C. A. Lochbaum, A. K. Chew, X. Zhang, V. Rotello, R. C. Van Lehn, J. A. Pedersen, "Lipophilicity of Cationic Ligands Promotes Irreversible Adsorption of Nanoparticles to Lipid Bilayers", *ACS Nano* **2021**, *15*, 6562–6572.

[12] P. Gkeka, P. Angelikopoulos, L. Sarkisov, Z. Cournia, "Membrane Partitioning of Anionic, Ligand-Coated Nanoparticles Is Accompanied by Ligand Snorkeling, Local Disordering, and Cholesterol Depletion", *PLOS Computational Biology* **2014**, *10*, e1003917.

[13] S. Franco-Ulloa, D. Guarnieri, L. Riccardi, P. P. Pompa, M. De Vivo, "Association Mechanism of Peptide-Coated Metal Nanoparticles with Model Membranes: A Coarse-Grained Study", *Journal of Chemical Theory and Computation* **2021**, *17*, 4512–4523.

[14] F. Simonelli, D. Bochicchio, R. Ferrando, G. Rossi, "Monolayer-Protected Anionic Au Nanoparticles Walk into Lipid Membranes Step by Step", *The Journal of Physical Chemistry Letters* **2015**, *6*, 3175–3179.

[15] E. Canepa, S. Salassi, F. Simonelli, R. Ferrando, R. Rolandi, C. Lambruschini, F. Canepa, S. Dante, A. Relini, G. Rossi, "Non-disruptive uptake of anionic and cationic gold nanoparticles in neutral zwitterionic membranes", *Scientific Reports* **2021**, *11*, 1256.

[16] S. Salassi, E. Canepa, R. Ferrando, G. Rossi, "Anionic nanoparticle-lipid membrane interactions: the protonation of anionic ligands at the membrane surface reduces membrane disruption", *RSC Advances* **2019**, *9*, 13992–13997.

[17] A. K. Ghose, G. M. Crippen, "Atomic physicochemical parameters for three-dimensional-structure-directed quantitative structure-activity relationships. 2. Modeling dispersive and hydrophobic interactions", *Journal of Chemical Information and Computer Sciences* **1987**, *27*, 21–35.

[18] D. Van Der Spoel, E. Lindahl, B. Hess, G. Groenhof, A. E. Mark, H. J. C. Berendsen, "GROMACS: Fast, flexible, and free", *Journal of Computational Chemistry* **2005**, *26*, 1701–1718.

[19] G. A. Tribello, M. Bonomi, D. Branduardi, C. Camilloni, G. Bussi, "PLUMED 2: New feathers for an old bird", *Computer Physics Communications* **2014**, *185*, 604–613.

[20] S. J. Marrink, H. J. Risselada, S. Yefimov, D. P. Tieleman, A. H. de Vries, "The MARTINI Force Field: Coarse Grained Model for Biomolecular Simulations", *The Journal of Physical Chemistry B* **2007**, *111*, 7812–7824.

[21] H. M. Khan, P. C. T. Souza, S. Thallmair, J. Barnoud, A. H. de Vries, S. J. Marrink, N. Reuter, "Capturing Choline–Aromatics Cation− Interactions in the MARTINI Force Field", *Journal of Chemical Theory and Computation* **2020**, *16*, 2550–2560.

[22] D. H. de Jong, G. Singh, W. F. D. Bennett, C. Arnarez, T. A. Wassenaar, L. V. Schäfer, X. Periole, D. P. Tieleman, S. J. Marrink, "Improved Parameters for the Martini Coarse-Grained Protein Force Field", *Journal of Chemical Theory and Computation* **2013**, *9*, 687–697.

[23] J. Michalowsky, L. V. Schäfer, C. Holm, J. Smiatek, "A refined polarizable water model for the coarse-grained MARTINI force field with long-range electrostatic interactions", *The Journal of Chemical Physics* **2017**, *146*, 054501.

[24] C. A. Huang-Zhu, J. K. Sheavly, A. K. Chew, S. J. Patel, R. C. Van Lehn, "Ligand Lipophilicity Determines Molecular Mechanisms of Nanoparticle Adsorption to Lipid Bilayers", *ACS Nano* **2024**, *18*, 6424–6437.

[25] C. A. Huang-Zhu, R. C. V. Lehn, "Influence of branched ligand architectures on nanoparticle interactions with lipid bilayers", *Nanoscale* **2025**, *17*, 1659–1672.

[26] F. Grunewald, G. Rossi, A. H. de Vries, S. J. Marrink, L. Monticelli, "Transferable MARTINI Model of Poly(ethylene Oxide)", *The Journal of Physical Chemistry B* **2018**, *122*, 7436–7449.

[27] T. A. Wassenaar, H. I. Ingólfsson, R. A. Böckmann, D. P. Tieleman, S. J. Marrink, "Computational Lipidomics with insane: A Versatile Tool for Generating Custom Membranes for Molecular Simulations", *Journal of Chemical Theory and Computation* **2015**, *11*, 2144–2155.

[28] S. Park, T. Kim, W. Im, "Transmembrane Helix Assembly by Window Exchange Umbrella Sampling", *Physical Review Letters* **2012**, *108*, 108102.

[29] R. C. Van Lehn, A. Alexander-Katz, "Grafting Charged Species to Membrane-Embedded Scaffolds Dramatically Increases the Rate of Bilayer Flipping", *ACS Central Science* **2017**, *3*, 186–195.

[30] J. S. Hub, B. L. De Groot, D. Van Der Spoel, "G-Whams-a Free Weighted Histogram Analysis Implementation Including Robust Error and Autocorrelation Estimates", *J. Chem. Theory Comput* **2010**, *6*, 3713.

[31] L. G. Smith, Z. Tan, A. Spasic, D. Dutta, L. A. Salas-Estrada, A. Grossfield, D. H. Mathews, "Chemically Accurate Relative Folding Stability of RNA Hairpins from Molecular Simulations", *Journal of Chemical Theory and Computation* **2018**, *14*, 6598–6612.

[32] R. C. Van Lehn, A. Alexander-Katz, "Energy landscape for the insertion of amphiphilic nanoparticles into lipid membranes: A computational study", *PLOS ONE* **2019**, *14*, e0209492.

[33] L. Li, I. Vorobyov, T. W. Allen, "Potential of Mean Force and pKa Profile Calculation for a Lipid Membrane-Exposed Arginine Side Chain", *The Journal of Physical Chemistry B* **2008**, *112*, 9574–9587.

[34] C. Neale, C. Madill, S. Rauscher, R. Pomès, "Accelerating Convergence in Molecular Dynamics Simulations of Solutes in Lipid Membranes by Conducting a Random Walk along the Bilayer Normal", *Journal of Chemical Theory and Computation* **2013**, *9*, 3686–3703.

[35] I. Kabelka, R. Brožek, R. Vácha, "Selecting Collective Variables and Free-Energy Methods for Peptide Translocation across Membranes", *Journal of Chemical Information and Modeling* **2021**, *61*, 819–830.

[36] N. Pokhrel, L. Maibaum, "Free Energy Calculations of Membrane Permeation: Challenges Due to Strong Headgroup–Solute Interactions", *Journal of Chemical Theory and Computation* **2018**, *14*, 1762–1771.

[37] B. Park, R. C. V. Lehn, "Bioinspired design rules for flipping across the lipid bilayer from systematic simulations of membrane protein segments", *Molecular Systems Design & Engineering* **2025**, *10*, 567–584.

[38] L. Monticelli, S. K. Kandasamy, X. Periole, R. G. Larson, D. P. Tieleman, S.-J. Marrink, "The MARTINI Coarse-Grained Force Field: Extension to Proteins", *Journal of Chemical Theory and Computation* **2008**, *4*, 819–834.

[39] J. Morstein, A. Capecchi, K. Hinnah, B. Park, J. Petit-Jacques, R. C. Van Lehn, J.-L. Reymond, D. Trauner, "Medium-Chain Lipid Conjugation Facilitates Cell-Permeability and Bioactivity", *Journal of the American Chemical Society* **2022**, *144*, 18532–18544.

[40] M. Post, G. Hummer, "AI-guided transition path sampling of lipid flip-flop and membrane nanoporation", *Nature Communications* **2025**, *17*, 224.

[41] L. Ou, H. Chen, B. Yuan, K. Yang, "Membrane-Specific Binding of 4 nm Lipid Nanoparticles Mediated by an Entropy-Driven Interaction Mechanism", *ACS Nano* **2022**, *16*, 18090–18100.

[42] S. Li, Z. Yan, F. Huang, X. Zhang, T. Yue, "How a lipid bilayer membrane responds to an oscillating nanoparticle: Promoted membrane undulation and directional wave propagation", *Colloids and Surfaces B: Biointerfaces* **2020**, *187*, 110651.

[43] R. Goetz, G. Gompper, R. Lipowsky, "Mobility and Elasticity of Self-Assembled Membranes", *Physical Review Letters* **1999**, *82*, 221–224.

[44] E. G. Brandt, O. Edholm, "Stretched exponential dynamics in lipid bilayer simulations", *The Journal of Chemical Physics* **2010**, *133*, 115101.

Chapter 5

Long-Chain Lipids Facilitate Insertion of Large Nanoparticles into Membranes of Small Unilamellar Vesicles[1]

5.1 Introduction

In recent years, synthesis methods for the production of high-quality nanoparticles (NPs) have greatly improved, allowing for increased control over their size, shape, and chemical and physical properties. This, in turn, enables the fabrication of sophisticated metallic, magnetic, dielectric, and semiconducting heterostructured NPs with desirable photophysical and chemical properties.[1–4] This precise control allows the engineering of excited-state wave functions,[5–7] charge confinement, and spatiotemporal control of charge-separated states.[8] Hence, NPs (and in particular semiconducting NPs) have proved to be very useful in diverse applications such as in optoelectronics,[9, 10] biological imaging,[11] sensing,[12–14] catalysis,[15] energy harvesting,[16] biomedicine, and cell surface engineering.[17–20]

While these sophisticated inorganic nanomaterials require advanced synthesis methods, their integration with biological macromolecules and machineries requires additional functionalization steps. Current approaches typically target NPs to interact with the cell membrane's surface or to undergo cellular uptake. Less effort has been invested in the functionalization of NPs that could be targeted, incorporated into, and retained in the membrane

[1]This chapter is adapted with permission from Marzouq, Morgenstein, Huang-Zhu, Yudovich, Atkins, Grupi, Van Lehn, and Weiss, *Langmuir*, 40:10477-10485, 2024. Copyright 2024 American Chemical Society. Supporting Information (SI) referenced is available at DOI:`https://doi.org/10.1021/acs.langmuir.3c03471`.

bilayer core itself.[21] Such membrane-inserted NPs could expand the repertoire of desired cellular functions while taking advantage of the superior inorganic materials' properties.[22, 23] Once inserted into the membrane, such NPs could, for example, introduce orthogonal (to native signaling) ways to communicate with the cell's interior, introduce de novo or enhance native enzymatic/catalytic activities, sense the membrane potential, or be used as antennas for light harvesting and vision restoration.[4, 24, 25]

The underlying obstacle for stable insertion of large NPs into lipid membranes is that in many cases, the surfaces of as-synthesized NPs are decorated with a mixture of highly hydrophobic ligands and are insoluble in biologically relevant aqueous media. Therefore, without any surface modification, these hydrophobic NPs must be efficiently incorporated into synthetic vesicle membranes between the two leaflets. Since phospholipid bilayers are typically 4–5 nm thick,[26, 27] successful membrane insertion has been achieved only for small NPs with sizes 5 nm.[28–30] Inclusion of larger hydrophobic NPs is thermodynamically unfavorable due to the energetic penalty associated with the protrusion of hydrophobic ligands into the surrounding polar solvent[30] or due to the deformation of the bilayer to minimize such protrusion.[31–33] This limitation practically excludes higher-order structures and functionalities that could be beneficial in terms of signal or actuation strength.

We hypothesized that the addition of long-chain lipids should promote the insertion of larger NPs than previously accomplished. The thickness of the phospholipid membrane can be increased by the incorporation of lipids with a long alkane chain and by the addition of cholesterol (CHOL), which aligns and stretches alkane chains into a packed and thick membrane.[26] To test this hypothesis, we prepared small unilamellar lipid vesicles incorporating 1,2-dinervonoylsn-glycero-3-phosphocholine (PC24), an unsaturated zwitterionic phospholipid with 24 carbon alkane chains. This lipid has been previously used in the preparation of multilamellar liposome (MLV) formulations with protein or peptide drugs, and in the formation of planar bilayer lipid membranes.[34] In biological systems, it is a component of lipid rafts and microdomains.[35]

Compared to typical PC18 lipids, which form membranes of 4–5 nm thickness, lipid bilayers consisting of 25% PC24 are expected to lead to a 20% increase in membrane thickness, *i.e.*, up to 6 nm. To test our hypothesis, we evaluated the membrane-insertion efficiency of inorganic NPs in the size range of 5–11 nm in diameter into the lipid bilayer of small unilamellar vesicles (SUVs) containing various molar fractions of PC24 during the formation of lipid vesicles. Initial attempts to incorporate even small NPs into SUVs prepared by the hydration method[36] were unsuccessful. After testing several other SUV preparation protocols for NP insertion that failed, we identified in the literature a protocol that was previously used to encapsulate hydrophobic drugs into liposomes' membranes[37] but never applied for

membrane incorporation of nanoparticles. This approach proved to be highly efficient for the membrane insertion of small NPs. A critical step in this protocol is the addition of a lipid detergent to an organic solution containing both lipids and NPs. With the addition of PC24 to the lipid mixture,[34] we found that NPs with diameters of up to 11 nm were successfully incorporated into SUV membranes.

Here, we present a detailed protocol for the incorporation of large NPs (up to 11 nm in diameter) into the lipid membrane of SUVs with optimized lipid composition, detergent, organic solvents, and the NP/lipid ratio. Cryogenic electron microscopy (cryo-EM) imaging of these membrane-inserted NPs is used for the characterization of their mode of interaction with the membrane, indicating their insertion to the midplane of the membrane. To determine the role of PC24 in facilitating insertion, we further performed coarse-grained molecular dynamics simulations to interrogate the lipid structural organization around membrane-embedded NPs. The simulations show that the longer PC24 lipids accumulate near membrane-inserted NPs to reduce the degree of membrane disruption and minimize exposure of the hydrophobic area to solvent, thereby modulating the insertion efficiency of large NPs even without substantial changes in overall membrane thickness.

5.2 Methods

5.2.1 Chemicals

All chemicals of the highest purity available were purchased and were used without further purifications; buffer solutions and sodium cholate were purchased from Sigma-Aldrich. 1-Palmitoyl-2-oleoyl-glycero-3-phosphocholine (POPC), 1,2-dioleoyl-3-trimethylammonium-propane (chloride salt) (DOTAP), cholesterol, and 1,2-dinervonoylsn-glycero-3-phosphocholine (PC24) were purchased from Avanti Polar Lipids. The as-synthesized 5 nm QDs were purchased from Cytodiagnostics (Burlington, Canada), and 7 and 11 nm QDs were purchased from ocean nanotech (San Diego, USA).

5.2.2 TEM Imaging

Carbon type A grid (Ted Pella Inc., Redding, USA) was glow discharged with a EmiTech K100 machine (Emitech Group, France), and then 3 L of NP was loaded on the grid. After 1 min the sample was blotted and access material was removed then air-dried. The sample was then inspected with a Tecnai G2 microscope (FEI, Teramo fisher, Massachusetts, USA) with an acceleration voltage of 120 kV. Images were taken using Digital Micrograph with a MultiScan Camera model 794 (Gatan, Inc., Pleasanton, United States) in different resolutions.

5.2.3 Absorbance Spectroscopy

The absorbance spectra of NPs were obtained with an Ocean Optics USB4000 spectrophotometer (Ostfildern, Germany). The spectra of NPs were obtained at a scan rate of 1200 nm/min with a 1 cm path length in a quartz cuvette.

5.2.4 Preparation of NP Embedded SUVs

In a typical preparation of SUV/NP constructs, 7 mol of total lipids (Table 5.1) were mixed with NPs (10 L of 5 M stock solution in chloroform) and dissolved in 30 L methanol:methylene chloride:chloroform (1:1:1; v:v:v). Next, 13 mg of the detergent sodium cholate was added to the organic solution giving 50 mM final concentration. In the next step, the organic solutions were evaporated for 1 h at 45 °C using a vacuum evaporator. Afterward, the dry film was resuspended with 0.5 mL of 20 mM phosphate buffer pH 7.2, giving the final lipid concentration of 18 mM, and the solution was equilibrated at 45 °C for 1 h.

Detergent was removed by controlled dialysis of the mixture against 3 of 20 mM phosphate buffer pH 7.2 (volume ratio = 1–1000) at 45 °C (using GeBAflex-tube 8KDa MWCO), and the mixture was extruded through 100 nm pore membrane 11 times at 45 °C using the LiposoFast instrument (Avanti polar lipids, Inc.)

5.2.5 Dynamic Light Scattering

Dynamic light scattering data were collected using the Zetasizer Nano ZS instrument (Malvern Instruments, Great Britain) operating at 25 °C with a laser wavelength λ of 620 nm and a scattering angle of 173°. Measurements were made using polystyrene low-volume microcuvettes (BrandTech Scientific, Inc. USA). Cuvettes were filled with 100 L of vesicle dispersion for DLS characterization. DLS data is shown in Figure S1.

5.2.6 Cryo-EM Imaging

For the cryo-EM measurement, 3 L of SUV/NP samples were loaded on a glow discharged (EmiTech K100 machine) Quantifoil grid or lacey grid that was blotted and plunged into liquid ethane using a Gatan CP3 automated plunger and stored in liquid nitrogen until use. Frozen specimens (samples with vesicles embedded in vitreous ice) were transferred to a Gatan 914 cryo-holder and maintained at temperatures below −176 °C inside the microscope. Samples were inspected with a Tecnai G2 microscope with an acceleration voltage of 120 kV, which is equipped with a cryobox decontaminator. Images were taken using a Digital Micrograph with a MultiScan Camera model 794 in different resolutions.

5.2.7 Data Analysis for Insertion Efficiency

The efficiency of NP- membrane incorporation was evaluated by calculation of the fraction of NPs that inserted the SUV lipid membrane. Three different experiments were conducted for each condition for every NP except for the 7 nm NP with "native" membrane SUVs where only 2 experiments were made. The insertion efficiency was calculated as # membrane inserted NPs/total # NPs in a frame and the complementary noninserted NPs as # noninserted NPs/total # NPs in a frame. Error bars represent the standard deviation of the number of inserted or noninserted particles observed between repetitions of each vesicle preparation.

5.2.8 Simulation Methods

We used GROMACS 2021.5[38, 39] to perform all simulations using a leapfrog integrator with a time step of 20 fs. The MARTINI [40] force field, version 2.3P, [41, 42] with the refined polarizable water model,[43] was used to model the interactions. Energy minimization, equilibration, and production simulation parameters were the same for all of the systems. Energy minimization was performed for 5,000 steps or until the maximum force was below 1,000 kJ/mol·nm. System equilibration and production runs were performed in the *NPT* ensemble. The temperature was controlled at 300 K using a velocity-rescale thermostat with a time constant of 1 ps. During equilibration runs, the pressure was controlled at 1 bar using the Berendsen barostat with semi-isotropic pressure coupling with a time constant of 5 ps and compressibility of 3×10^4 bar^1. A 5 ns equilibration was performed with a time step of 10 fs, followed by a 15 ns equilibration with a time step of 15 fs, and a final 25 ns equilibration with a time step of 20 fs, for a total of 45 ns of equilibration. Production runs were performed using the same parameters as the equilibration runs with the exception of the barostat, which was switched to a Parrinello–Rahman barostat with a time constant of 12 ps. We used the Visual Molecular Dynamics (VMD)[44] software, release 1.9.4a55, to generate all simulation snapshots.

5.2.9 System Setup for Coarse-Grained MD Simulations

We modeled the 5, 7, and 11 nm spherical CdSe/ZnS QDs as hollow shells coated with hydrophobic octadecylamine ligands. We coated the QD surface at a grafting density of 3.9 ligands/nm^2 based on the literature of similar CdSe/ZnS QDs.[45–47] Details on the coarse-grained models[48] are included in the Supporting Information (Figure S4 and Table S3).

Lipids were modeled according to their standard topologies in MARTINI with PC24 modeled as DNPC. The MARTINI topology for DOTAP was added to this script. All

bilayer lipid mixtures were generated using the *insane.py* script.[49] Pure (*i.e.*, without inserted QDs) native and thick bilayers were simulated in 15 × 15 × 10 nm simulation boxes for 100 ns to quantify their bulk properties; the last 50 ns were used for analyses (Figure S9). For the QD/bilayer systems, the QD was placed in the middle of the bilayer and solvated with polarizable water. We neutralized the system by adding a number of Cl^- ions equal to the number of DOTAP lipids using the gmx genion tool. The box size was 36 × 36 × 16 nm for the 5 nm QD, 38 × 38 × 16 nm for the 7 nm QD, and 42 × 42 × 20 nm for the 11 nm QD. We specified an initial area per lipid of 0.7 nm^2/lipid to ensure system stability. The total numbers of molecules for all systems are listed in Table S4 and Table S5.

We performed production simulations of 200 ns for the systems with the 5 and 7 nm QDs and 400 ns for the system with the 11 nm QD, sampling every 0.2 ns. System convergence was assessed by plotting the area per lipid (nm^2) throughout the production run (Figure S5). As the QD size increases, longer equilibration times were required. The last 100 ns of simulation time for all QD/bilayer systems were deemed as converged and used for subsequent analyses.

5.3 Results and Discussion

In order to insert NPs efficiently into the lipid bilayer of SUVs, we adopted a detergent dialysis-based vesicle preparation method that was previously optimized for membrane incorporation of small hydrophobic drugs.[37] This procedure was modified to allow for the insertion of NPs into SUV membranes. Two different mixtures of lipids were used for SUV preparation: a "native membrane" mixture with POPC, CHOL, and DOTAP (central column in Table 5.1), and a "thick membrane" mixture with POPC, CHOL, DOTAP, and a very long-chain phospholipid (PC24). Insertion efficiency was tested for four different sizes of NPs: 5, 7, and 11 nm diameter spherical CdSe/ZnS quantum dots (QDs; sizes determined by TEM; Table S1). Cryo-EM imaging was used to assess the mode of NP interaction/insertion with/into the SUVs' membrane. As described in the Supporting Information, the yield of NP insertion into the membrane was evaluated by examining the cryo-EM images and counting membrane-inserted NPs, membrane-adsorbed NPs, and encapsulated NPs. We excluded all NPs that were either interacting with the carbon grid or aggregated. Multiple experiments on different days were conducted for each condition (NP size and "native" or "thick" membrane). Preparations were repeated for each condition, and multiple field-of-views (FOVs) were collected from each grid. Insertion efficiency was defined as the ratio between the number of membrane-inserted NPs and the total number of NPs in a frame. Results from all analyzed frames per condition were averaged. We note that the surfaces of the QDs are coated with hydrophobic ligands as prepared, facilitating their favorable interaction with the membrane core.

Table 5.1: Five Different Lipid Composition Used for the Liposome Studies with [PC24] Increasing from 0 mol % (Sample 1) to 100 mol % (Sample 5)

	composition			
sample	PC24 (mol %)	POPC (mol %)	CHOL (mol %)	DOTAP (mol %)
1	0	70	20	10
2	25	51	14	10
3	50	31	9	10
4	75	12	3	10
5	100	0	0	0

In order to find a suitable working concentration of PC24 to be added to the "thick membrane" mixture, we first tested five preparations of SUVs using different relative concentrations of PC24 and evaluated the effect of PC24 concentration (Table S2). SUVs were prepared as described in the Supporting Information. Each preparation was imaged by cryo-EM in order to assess the morphology and uniformity of different SUV composition. Based on cryo-EM imaging, we found that a relative molar concentration of [PC24] = 25 mol % resulted in relatively uniform and spherical SUVs, while concentrations above [PC24] = 25 mol % resulted in polygonal SUV formation, with SUVs' morphology being less spherical and more polygonal as [PC24] increased (Figure S2). Furthermore, [PC24] = 50% showed remarkably decreased SUV formation yields, and a negligible number of SUVs were observed via cryo-EM imaging. The nonspherical, polygonal SUV shapes can be attributed to the membrane's gel phase behavior, since PC24 has a transition temperature of 26 °C,[50–52] which is higher than the transition temperature of POPC (−2 °C). Assuming uniform lipid mixing and distribution and given the transition temperature of each lipid component, it is reasonable to assert that using a high component fraction of PC24 lipids in the SUV composition, which were exposed in this work to room temperature prior to cryo-EM imaging, will result in solid/gel phase lipid bilayer behavior that will interfere with both spherical SUV formation and the incorporation of nanoparticles into the bilayer.

Figure 5.1 shows the cryo-EM images of selected examples of successful insertion of the different size/type of NPs into SUVs created from the "thick" membrane mixture. The morphologies of the SUVs at different PC24 concentrations are shown in Figure S2 and raw images are deposited.[52] The blue and red bars on the right columns indicate the fractions of inserted and noninserted particles, respectively, out of all counted particles, excluding aggregates and carbon-interacting particles.

As expected, insertion efficiency was inversely proportional to the NP size for native membranes due to the NP size, whereas the long lipid addition had a significant effect on the larger particle as a result of the addition of long-chain lipids. Interestingly, while the insertion efficiency for the largest QDs (11 nm) was 7.1% in the native membrane lacking

PC24, it increased to 76.5% when inserted into the "thick" membrane containing [PC24] = 25 mol %. For other NPs, we saw an increase from 46% to 70% for the 5 nm QDs and 40% to 48% for the 7 nm QDs.

We note the low number of observed membrane-inserted QDs, especially for the sample preparation conditions expected to have a lower incorporation yield, such as in the case of membranes lacking long-chain PC24 lipids. Observing membrane incorporation in such low-yield samples via cryo-EM imaging, which has an inherently low throughput, is challenging in terms of attaining statistically significant data. However, our observations provide strong evidence of the increased insertion efficiency of large quantum dots into PC24-containing vesicles. This evidence is most significant for 11 nm QDs, where membrane incorporation is

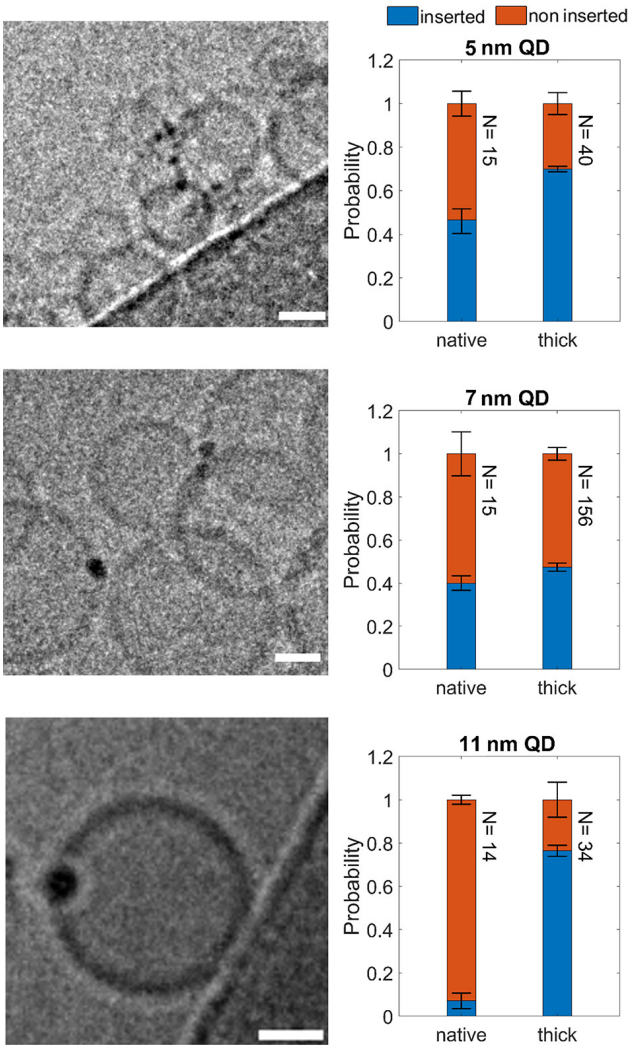


Figure 5.1: Incorporation of NPs into thick SUV membranes. Left column: cryo-EM images showing examples for insertion of 5, 7, and 11 nm QDs (from top to bottom) into thick SUV membranes. Right column: corresponding insertion efficiencies of NPs in native and thick membranes, while N is the total number of counted particles. Lipid composition for native and thick membranes is described in Table S2. Scale bars: 20 nm.

essentially unattainable for “thin” membranes, and does occur for “thick” PC24-containing vesicles. In addition, while the ratio between inserted and noninserted 7 nm QDs in “native” and “thick” membranes is similar, it is worth noting that the total number of both inserted and noninserted 7 nm QDs was significantly higher for the case of ‘thick’ PC24-containing vesicles. The higher number of SUVs associated with QDs can indicate that while full membrane insertion of 7 nm QDs is not more stable with the presence of PC24 lipids, their transient incorporation is more likely, resulting in a higher frequency of SUVs interacting with QDs at the moment of sample plunge freezing.

We further evaluated the degree of insertion for the 11 nm QDs by localizing the position of QDs relative to the SUVs’ membranes using home-written software, as described in the Supporting Information. Figure 5.2d shows a histogram of these distances: positive distances represent locations in the outer SUV leaflet and outward from center of the SUV, and negative distances represent locations in the inner SUV leaflet and inward toward the center of the SUV. The histogram shows that these large NPs are most likely to be located near the center of the membrane. Figure 5.2a–c shows three examples of analyzed FOVs, representing QDs that are located inward the SUV, the bilayer midline, and outward the SUV, respectively.

We next performed molecular dynamics simulations to simulate the spherical QDs in their membrane-inserted states and characterize the role of PC24 in modulating lipid organization and structural properties to promote insertion efficiency. Due to the large size of these systems, we performed coarse-grained molecular dynamics simulations using the MARTINI[40] force field, version 2.3P,[41, 42] with the refined polarizable water model,[43] see the Materials and Methods section for molecular dynamics simulations. Details on the CG models, simulation parameters, and simulation convergence are included in the Supporting Information (Tables S3–S5 and Figures S4,S5). Since the same trends were observed across

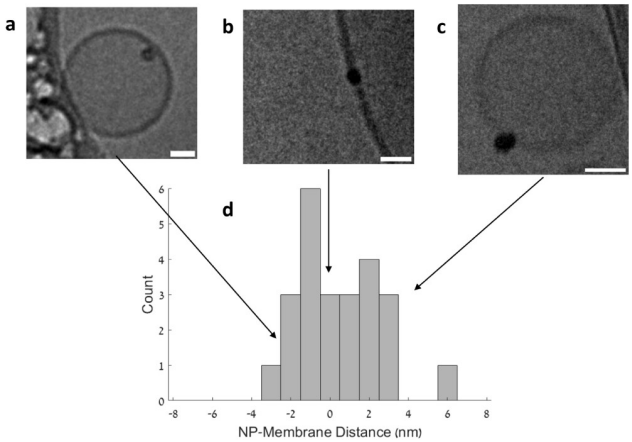


Figure 5.2: (a—c) Cryo-EM images showing 11 nm QDs inserted into thick SUVs. (d) Position distribution of QDs interacting with thick membrane SUVs. Only QDs that were in the vicinity of an SUV, but not in the vicinity of other QDs, were counted (24 QDs in total). Scale bars: 20 nm.

the three QDs, we only show data for the intermediate 7 nm QD here; data for the 5 and 11 nm QDs are included in Figures S10–S16.

Figure 5.3 shows snapshots of final configurations of the 7 nm QDs in the native and thick membranes. The accompanying histograms show the volumetric density of headgroups (lipids/nm^3) for each lipid species normalized by the volumetric density of the same headgroups in a bilayer without the inserted QD. These histograms provide information about the enrichment of each species compared to the bulk bilayer. Several observations are apparent from these data. First, comparing the POPC histograms at radial distances far from the QD reveals no significant increase in the average bilayer thickness in the thick membrane compared to the native membrane, likely because the fraction of PC24 (25 mol %) is small compared to POPC (45 mol %). Second, lipids extract from the membrane and onto the surface of the QD to shield the hydrophobic QD surface and ligands from water. At equilibrium, the inserted QDs are fully enveloped by lipids, in agreement with similar reports in the literature.[53, 54] This behavior leads to substantial deformation of the extracted lipids due to the high curvature of the NP surface, which is expected to be unfavorable. Third, the simulation snapshots demonstrate the formation of bundles of hydrophobic ligands with voids between bundles;[55] these voids are filled with lipid tails (not visible in Figure 5.3 but shown in Figures S17–S19).

A key distinction between the native and thick membranes is that PC24 is enriched in the region near the QD in the thick membranes (observed from the dark color for PC24 in Figure 5.3). This preferential enrichment results in an interfacial region around the QD that has a different lipid composition than that of the bulk bilayer. We further quantified enrichment by computing the area density of lipids (lipids/nm^2) at fixed radial distances from the center of the QD. Figure 5.4a,b reveals peaks in these area densities that corroborate the lipid enrichment and depletion at defined radial distances. Specifically, in both the native and thick membranes the POPC and DOTAP densities are maximized at a radial distance of 5–7 nm from the center of the QD, which we define as the QD-membrane interfacial region. We also observed that in thick membranes the area density for POPC and DOTAP decreases in this interfacial region while the area density of PC24 increases. Both observations are in agreement with their corresponding 2D histograms in Figure 5.3 and indicate that PC24 preferentially accumulates in the QD-membrane interfacial region, primarily displacing POPC.

We hypothesized that the preferential enrichment of PC24 lipids in the QD-membrane interfacial region could stabilize QD insertion by reducing the extent of bilayer disruption. To test this hypothesis, we computed the P_2 lipid tail order parameter of the lipid acyl chain tails,[56] which is defined as

$$P_2 = \frac{1}{2}\langle 3\cos^2\theta - 1\rangle$$

where θ denotes the angle between the vector connecting two consecutive lipid tail beads and the local vector normal to the monolayer containing that lipid. For each lipid, P_2 was computed for vectors connecting every consecutive tail bead (from the last hydrophobic bead to the glycerol bead). Details on how the local normal vectors and P_2 were computed are

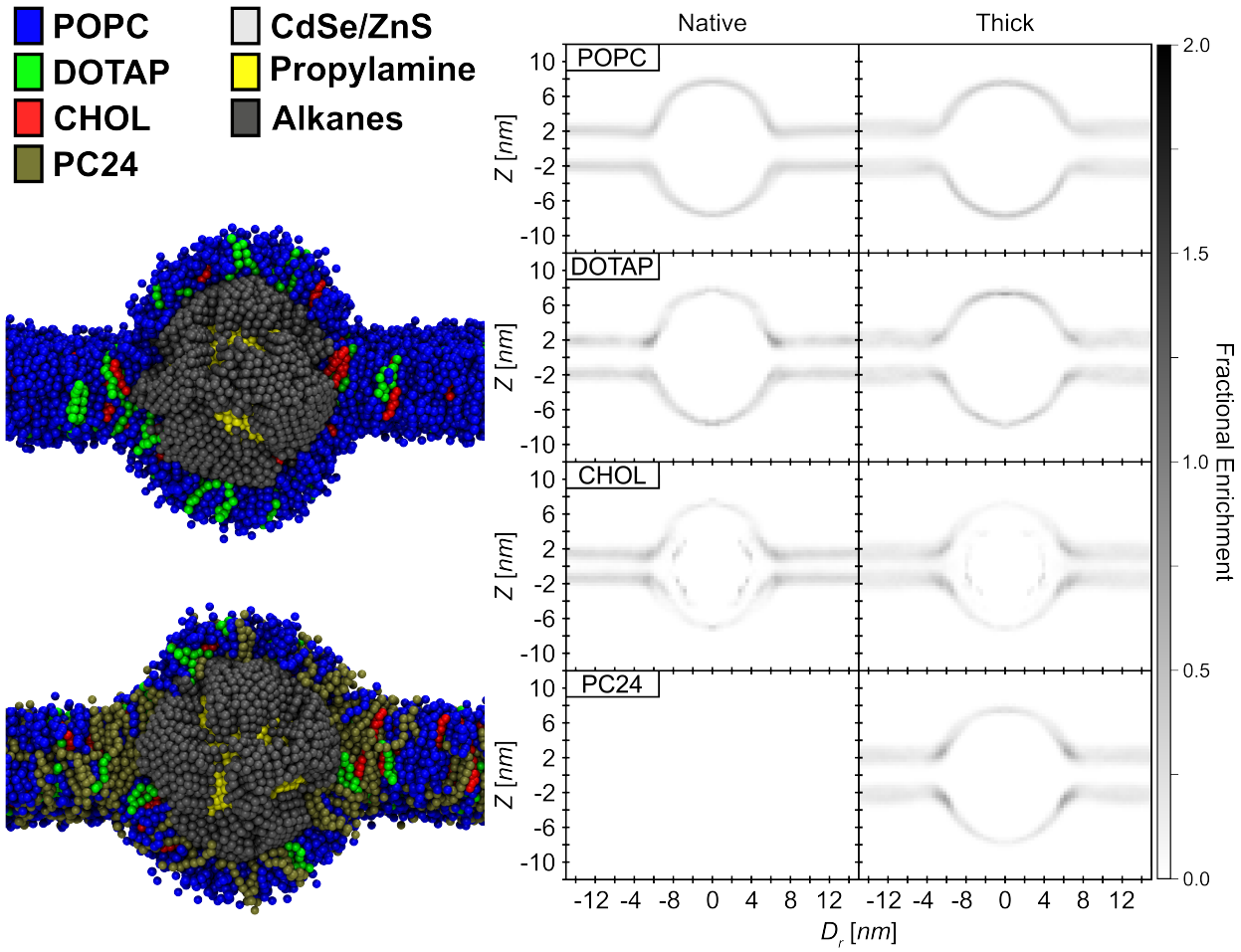


Figure 5.3: Simulation snapshots and 2D histograms of lipid headgroups for the 7 nm QD. Snapshots show the side view of the inserted QD with all water molecules, counterions, and half of the lipids in the y-axis with respect to the center of mass of the QD removed for visual purposes. The native membrane is shown at the top and thick membrane at the bottom. For the 2D histograms, Z is the distance along the z-axis, and Dr is the radial distance from the center of the QD in the xy-plane. The lipid headgroups selected for analysis were the phosphate group for POPC and PC24, the choline group for DOTAP, and the hydroxyl group for CHOL; they were binned radially in 0.375 nm wide by 0.375 nm tall bins and normalized by the volume of each bin and the number of configurations sampled. The color bar represents the fractional enrichment defined as the volumetric density of the lipid headgroups (lipids/nm^3) normalized by the volumetric density of the lipid headgroups in the corresponding pure bilayer system.

included in the Supporting Information. This parameter measures the structural orientation between consecutive tail beads with respect to the local bilayer normal; aligned lipid tails increase the P_2, indicating increased tail order. Figure 5.4c compares values of P_2 (reported as an average over values of P_2 computed for all consecutive tail bead vectors in both tails) for lipids near the QD to values of P_2 for lipids far from the QD in both the native and thick membranes to quantify QD-driven membrane disruption (indicated by lower values of P_2). Figure 5.4c shows that compared to its bulk value in the native membrane, P_2 substantially decreases for the POPC lipids in the QD-membrane interfacial region where the area density of POPC reaches a maximum (Figure 5.4a). This observation is consistent with the energetically unfavorable disruption of the lipid order in this interfacial region due to the presence of the QD. P_2 increases for lipids extracted onto the QD to achieve values similar to those of the bulk values. Similar behavior is observed for POPC in the thick membrane. Conversely, for the long-chain PC24 lipids, P_2 peaks near its density maximum but then decreases to a lesser degree in the QD-membrane interfacial region relative to values of P_2 in the bulk. The similarity of P_2 to the bulk value indicates less disruption of these lipids compared with the shorter-chain POPC lipids.

We further computed P_2 values as a function of tail bead number for all consecutive tail beads in the CG simulations, which we refer to as segmental P_2 values (Figure S8). Comparing segmental P_2 values for lipids in the QD-membrane interfacial region to lipids in the bulk again confirms that POPC lipids exhibit decreased ordering consistent with membrane disruption in both native and thick membranes but disruption occurs to a lesser extent in the thick membrane. Moreover, PC24 shows almost no change in the lipid tail order between bulk and interface lipids, further suggesting that long-chain lipids effectively decrease membrane disruption to allow higher NP insertion efficiency. Together, the data in Figures 4 and S8 indicate that in the thick membrane PC24 lipids preferentially accumulate in the QD-membrane interfacial region to reduce overall membrane disruption compared with the native membrane.

A second distinction between the native and thick membranes relates to the voids between ligand bundles observable in Figure 5.4; these voids are filled with lipid tails to minimize contact between hydrophobic ligand backbones and water. In the thick membrane, PC24 lipids preferentially partition into these void regions and exclude POPC lipids (Figures S17−S19), similar to the exclusion of POPC lipids from the QD-membrane interfacial region. These results suggest that the PC24 tails can more favorably partition into the void spaces given their longer length than the POPC tails, providing another mechanism to minimize overall bilayer disruption in the thick membranes.

Previous works have shown that only very small QDs (<4 nm)[27–29] can be incorporated into SUV membranes during their formation using electro-swelling, sonication, and other de-

tergent removal protocols.[37] Here, we used a different approach that relied on a previously published protocol for membrane incorporation of small hydrophobic drug molecules.[33] In this approach, a dialysis-based detergent removal step was performed during the preparation of the vesicles. This improved protocol was sufficient for the insertion of larger (>5 nm) particles into SUVs with membranes composed of POPC and CHOL, although at low efficiency. The addition of 25 mol % of a long-chain phospholipid, PC24, significantly improved the insertion of large particles into SUV membranes, and facilitated the insertion of large QDs (11 nm) at high efficiency. Combining both approaches, NPs as large as 11 nm QDs were successfully inserted into SUVs.

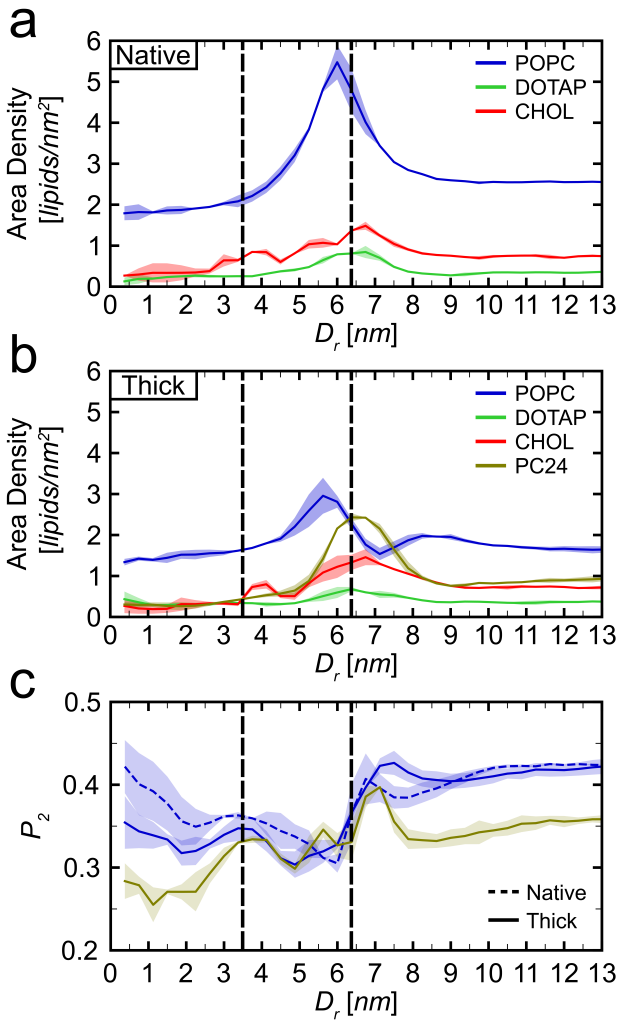


Figure 5.4: Lipid properties were computed for the 7 nm QD. D_r is the radial distance from the center of the QD in the xy-plane, and parameters are calculated in radial bins with a width of 0.375 nm. The lipid headgroups selected for analysis were the phosphate group for POPC and PC24, the choline group for DOTAP, and the hydroxyl group for CHOL lipid area density (lipids/nm^2) for each type of lipid in the native (A) and thick (B) membranes. (C) Lipid tail order parameter, P_2, computed for POPC and PC24 in both native and thick membranes. The left vertical dashed line corresponds to the QD radius, and the right vertical dashed line corresponds to the radial distance corresponding to the maximum area density of PC24. The error was calculated as the standard deviation between the two replicas.

Coarse-grained molecular simulations suggest two key factors for why long-chain lipids facilitate the insertion of large CdSe/ZnS QDs coated with octadecylamine ligands, as schematically illustrated in Figure 5.5. First, long-chain lipids preferentially accumulate in the interfacial region at the QD-membrane interface, displacing POPC. The thicker interfacial region results in less disruption of the bilayer compared to that of the native membrane, which is energetically favorable and thermodynamically stabilizes QD insertion. PC24 thus acts similarly to a linactant,[57] a molecule that decreases the line tension between lipid domains. In this case, the line tension at the interface between lipids on the QD and lipids on the bulk bilayer is decreased, potentially increasing insertion efficiency for large NPs. Second, PC24 preferentially fills voids in the ligand monolayer that arise due to the formation of ligand bundles, again displacing POPC. The longer PC24 tails can more effectively pack against the long octadecylamine ligand backbones to again minimize bilayer disruption. These factors point to PC24-induced changes to lipid structural organization as facilitating QD insertion, even without substantial changes in the overall membrane thickness.

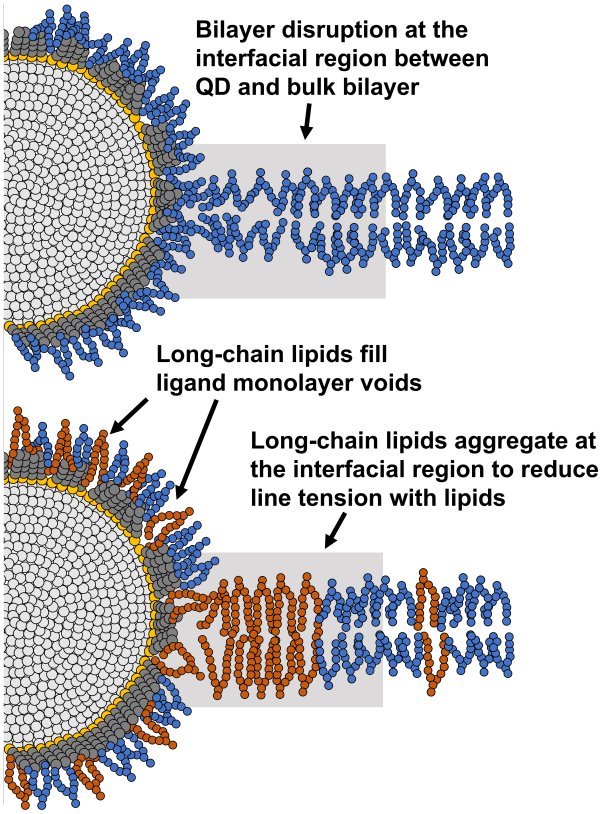


Figure 5.5: Schematic illustration of the long-chain lipid aggregation and increased lipid tail order in the interfacial region between the QD and the bulk bilayer (shaded region). Long-chain lipids (PC24) are colored orange. Medium-chain lipids (POPC and DOTAP) are colored blue. The QD shell is colored light gray, the amine group of the ligands are colored yellow, and the ligand hydrophobic groups are colored gray.

5.4 Conclusions

In summary, we developed a lipid composition and SUV preparation protocol that promotes the integration of large inorganic hydrophobic particles into membranes. It is well-accepted that membrane thickness varies with acyl chain length and the presence of cholesterol. We found that adding long-chain phospholipids (C24:1) to the vesicle formulation is crucial for the incorporation of NPs with diameters much larger than those reported for typical lipid composition. Molecular dynamics simulations indicate that the long-chain lipids act like linactants that stabilize membrane-inserted QDs. Although the main obstacle for NP incorporation into SUVs is their size, the effect of the hydrophobic capping ligand layer and the particle geometry on insertion into SUVs is a matter of future study. These SUVs could be made fusogenic to allow the delivery of NPs into the cellular membranes. The technology developed here could be applied to diagnostic technologies, therapeutic applications, and as a research tool for studying membrane properties. The computational approach in this work can also be potentially applied to other classes of nanomaterials and more biologically relevant membrane models to analyze the insertion efficiency. By enabling these predictions, we can explore a wider range of materials as biomedical agents.

References

[1] Z. A. Peng, X. Peng, "Nearly Monodisperse and Shape-Controlled CdSe Nanocrystals via Alternative Routes: Nucleation and Growth", *J. Am. Chem. Soc.* **2002**, *124*, 3343.

[2] X. Peng, L. Manna, W. Yang, J. Wickham, E. Scher, A. Kadavanich, A. P. Alivisatos, "Shape Control of CdSe Nanocrystals", *Nature* **2000**, *404*, 59.

[3] L. Manna, E. C. Scher, A. P. Alivisatos, "Synthesis of Soluble and Processable Rod-, Arrow-, Teardrop-, and Tetrapod-Shaped CdSe Nanocrystals", *J. Am. Chem. Soc.* **2000**, *122*, 12700.

[4] V. De Leo, L. Catucci, A. Falqui, R. Marotta, M. Striccoli, A. Agostiano, R. Comparelli, F. Milano, "Hybrid Assemblies of Fluorescent Nanocrystals and Membrane Proteins in Liposomes", *Langmuir* **2014**, *30*, 1599.

[5] N. N. Hewa-Kasakarage, M. Kirsanova, A. Nemchinov, N. Schmall, P. Z. El-Khoury, A. N. Tarnovsky, M. Zamkov, "Radiative Recombination of Spatially Extended Excitons in (ZnSe/CdS)/CdS Heterostructured Nanorods", *J. Am. Chem. Soc.* **2009**, *131*, 1328.

[6] J. Müller, J. M. Lupton, A. L. Rogach, J. Feldmann, D. V. Talapin, H. Weller, "Monitoring Surface Charge Migration in the Spectral Dynamics of Single CdSe CdS Nanodot/Nanorod Heterostructures", *Phys. Rev. B* **2005**, *72*, 205339.

[7] D. V. Talapin, J. H. Nelson, E. V. Shevchenko, S. Aloni, B. Sadtler, A. P. Alivisatos, "Seeded Growth of Highly Luminescent CdSe/CdS Nanoheterostructures with Rod and Tetrapod Morphologies", *Nano Lett.* **2007**, *7*, 2951.

[8] J. Müller, J. M. Lupton, P. G. Lagoudakis, F. Schindler, R. Koeppe, A. L. Rogach, J. Feldmann, D. V. Talapin, H. Weller, "Wave Function Engineering in Elongated Semiconductor Nanocrystals with Heterogeneous Carrier Confinement", *Nano Lett.* **2005**, *5*, 2044.

[9] T. H. Kim, K. S. Cho, E. K. Lee, S. J. Lee, J. Chae, J. W. Kim, D. H. Kim, J. Y. Kwon, G. Amaratunga, S. Y. Lee, "Full-Colour Quantum Dot Displays Fabricated by Transfer Printing", *Nat. Photonics* **2011**, *5*, 176.

[10] V. I. Klimov, S. A. Ivanov, J. Nanda, M. Achermann, I. Bezel, J. A. McGuire, A. Piryatinski, "Single-Exciton Optical Gain in Semiconductor Nanocrystals", *Nature* **2007**, *447*, 441.

[11] X. Michalet, F. F. Pinaud, L. A. Bentolila, J. M. Tsay, S. Doose, J. J. Li, G. Sundaresan, A. M. Wu, S. S. Gambhir, S. Weiss, "Quantum Dots for Live Cells, in Vivo Imaging, and Diagnostics", *Science* **2005**, *307*, 538.

[12] S. Li, K. Zhang, J. M. Yang, L. Lin, H. Yang, "Single Quantum Dots as Local Temperature Markers", *Nano Lett.* **2007**, *7*, 3102.

[13] M. J. Ruedas-Rama, E. A. H. Hall, "Azamacrocycle Activated Quantum Dot for Zinc Ion Detection", *Anal. Chem.* **2008**, *80*, 8260.

[14] H. Aouani, S. Itzhakov, D. Gachet, E. Devaux, T. W. Ebbesen, H. Rigneault, D. Oron, J. Wenger, "Colloidal Quantum Dots as Probes of Excitation Field Enhancement in Photonic Antennas", *ACS Nano* **2010**, *4*, 4571.

[15] H. Zhu, N. Song, H. Lv, C. L. Hill, T. Lian, "Near Unity Quantum Yield of Light-Driven Redox Mediator Reduction and Efficient H2 Generation Using Colloidal Nanorod Heterostructures", *J. Am. Chem. Soc.* **2012**, *134*, 11701.

[16] I. Mora-Seró, J. Bisquert, "Breakthroughs in the Development of Semiconductor-Sensitized Solar Cells", *J. Phys. Chem. Lett.* **2010**, *1*, 3046.

[17] R. F. Fakhrullin, A. I. Zamaleeva, R. T. Minullina, S. A. Konnova, V. N. Paunov, "Cyborg Cells: Functionalisation of Living Cells with Polymers and Nanomaterials", *Chem. Soc. Rev.* **2012**, *41*, 4189.

[18] J. Z. Wang, Z. Q. Ding, F. Zhang, W. B. Ye, "Recent Development in Cell Encapsulations and Their Therapeutic Applications", *Mater. Sci. Eng.* **2017**, *77*, 1247.

[19] B. J. Kim, H. Cho, J. H. Park, J. F. Mano, I. S. Choi, "Strategic Advances in Formation of Cell-in-Shell Structures: From Syntheses to Applications", *Adv. Mater.* **2018**, *30*, 1706063.

[20] T. Liu, Y. Wang, W. Zhong, B. Li, K. Mequanint, G. Luo, M. Xing, "Biomedical Applications of Layer-by-Layer Self-Assembly for Cell Encapsulation: Current Status and Future Perspectives", *Adv. Healthcare Mater.* **2019**, *8*, 1800939.

[21] R. C. Van Lehn, P. U. Atukorale, R. P. Carney, Y. S. Yang, F. Stellacci, D. J. Irvine, A. Alexander-Katz, "Effect of Particle Diameter and Surface Composition on the Spontaneous Fusion of Monolayer-Protected Gold Nanoparticles with Lipid Bilayers", *Nano Lett.* **2013**, *13*, 4060.

[22] P. Pandey, S. P. Singh, S. K. Arya, V. Gupta, M. Datta, S. Singh, B. D. Malhotra, "Application of Thiolated Gold Nanoparticles for the Enhancement of Glucose Oxidase Activity", *Langmuir* **2007**, *23*, 3333.

[23] G. Tikhomirov, S. Hoogland, P. E. Lee, A. Fischer, E. H. Sargent, S. O. Kelley, "DNA-Based Programming of Quantum Dot Valency, Self-Assembly and Luminescence", *Nature* **2011**, *6*, 485.

[24] M. E. Åkerman, W. C. W. Chan, P. Laakkonen, S. N. Bhatia, E. Ruoslahti, "Nanocrystal Targeting in Vivo", *Proc. Natl. Acad. Sci. U. S. A.* **2002**, *99*, 12617.

[25] A. M. Derfus, W. C. W. Chan, S. N. Bhatia, "Intracellular Delivery of Quantum Dots for Live Cell Labeling and Organelle Tracking", *Adv. Mater.* **2004**, *16*, 961.

[26] K. Cathcart, A. Patel, H. Dies, M. C. Rheinstädter, C. Fradin, "Effect of Cholesterol on the Structure of a Five-Component Mitochondria-Like Phospholipid Membrane", *Membranes* **2015**, *5*, 664.

[27] S. Tharad, Ö. Üzülmez, B. Promdonkoy, J. L. Toca-Herrera, "Cholesterol Increases Lipid Binding Rate and Changes Binding Behavior of Bacillus Thuringiensis Cytolytic Protein", *Int. J. Mol. Sci.* **2018**, *19*, 3819.

[28] V. De Leo, F. Milano, A. Paiano, R. Bramato, L. Giotta, R. Comparelli, S. Ruscigno, A. Agostiano, C. Bucci, L. Catucci, "Luminescent CdSe@ZnS Nanocrystals Embedded in Liposomes: A Cytotoxicity Study in HeLa Cells", *Toxicol Res.* **2017**, *6*, 947.

[29] G. Gopalakrishnan, C. Danelon, P. Izewska, M. Prummer, P. Y. Bolinger, I. Geissbühler, D. Demurtas, J. Dubochet, H. Vogel, "Multifunctional Lipid/Quantum Dot Hybrid Nanocontainers for Controlled Targeting of Live Cells", *Angew. Chem. Int. Ed.* **2006**, *45*, 5478.

[30] X. Guo, Y. Zhang, J. Liu, X. Yang, J. Huang, L. Li, L. Wan, K. Wang, "Red Blood Cell Membrane-Mediated Fusion of Hydrophobic Quantum Dots with Living Cell Membranes for Cell Imaging", *J. Mater. Chem. B* **2016**, *4*, 4191.

[31] R. C. Van Lehn, A. Alexander-Katz, "Membrane-Embedded Nanoparticles Induce Lipid Rearrangements Similar to Those Exhibited by Biological Membrane Proteins", *J. Phys. Chem. B* **2014**, *118*, 12586.

[32] J. H. Lorent, B. Diaz-Rohrer, X. Lin, K. Spring, A. A. Gorfe, K. R. Levental, I. Levental, "Structural Determinants and Functional Consequences of Protein Affinity for Membrane Rafts", *Nat. Commun.* **2017**, *8*, 1219.

[33] O. G. Mouritsen, M. Bloom, "Mattress Model of Lipid-Protein Interactions in Membranes", *Biophys. J.* **1984**, *46*, 141.

[34] A. Lazzarini, A. Macchiarulo, A. Floridi, A. Coletti, S. Cataldi, M. Codini, R. Lazzarini, E. Bartoccini, G. Cascianelli, F. S. Ambesi-Impiombato, "Very-Long-Chain Fatty Acid Sphingomyelin in Nuclear Lipid Microdomains of Hepatocytes and Hepatoma Cells: Can the Exchange from C24: 0 to C16: 0 Affect Signal Proteins and Vitamin D Receptor?", *Mol. Biol. Cell* **2015**, *26*, 2418.

[35] K. C. Courtney, W. Pezeshkian, R. Raghupathy, C. Zhang, A. Darbyson, J. H. Ipsen, D. A. Ford, H. Khandelia, J. F. Presley, X. Zha, "C24 Sphingolipids Govern the Transbilayer Asymmetry of Cholesterol and Lateral Organization of Model and Live-Cell Plasma Membranes", *Cell Rep.* **2018**, *24*, 1037.

[36] H. Zhang, *Methods in Molecular Biology*, *Vol. 1522*, **2017**.

[37] R. A. Schwendener, "Liposomes as Vaccine Delivery Systems: A Review of the Recent Advances", *Ther. Adv. Vaccines* **2014**, *2*, 159.

[38] D. Van Der Spoel, E. Lindahl, B. Hess, G. Groenhof, A. E. Mark, H. J. C. Berendsen, "GROMACS: Fast, Flexible, and Free", *J. Comput. Chem.* **2005**, *26*, 1701.

[39] E. Lindahl, M. Abraham, B. Hess, D. van der Spoel, *GROMACS 2021.5 Source code*, **2022**.

[40] S. J. Marrink, H. J. Risselada, S. Yefimov, D. P. Tieleman, A. H. De Vries, "The MARTINI Force Field: Coarse Grained Model for Biomolecular Simulations", *J. Phys. Chem. B* **2007**, *111*, 7812.

[41] H. M. Khan, P. C. T. Souza, S. Thallmair, J. Barnoud, A. H. De Vries, S. J. Marrink, N. Reuter, "Capturing Choline-Aromatics Cation-IIInteractions in the MARTINI Force Field", *J. Chem. Theory Comput.* **2020**, *16*, 2550.

[42] D. H. De Jong, G. Singh, W. F. D. Bennett, C. Arnarez, T. A. Wassenaar, L. V. Schäfer, X. Periole, D. P. Tieleman, S. J. Marrink, "Improved Parameters for the Martini Coarse-Grained Protein Force Field", *J. Chem. Theory Comput.* **2013**, *9*, 687.

[43] J. Michalowsky, L. V. Schäfer, C. Holm, J. Smiatek, "A Refined Polarizable Water Model for the Coarse-Grained MARTINI Force Field with Long-Range Electrostatic Interactions", *J. Chem. Phys.* **2017**, *146*, 054501.

[44] W. Humphrey, A. Dalke, K. Schulten, "VMD: Visual Molecular Dynamics", *J. Mol. Graphics* **1996**, *14*, 33.

[45] B. R. Watson, Y. Z. Ma, J. F. Cahill, B. Doughty, T. R. Calhoun, "Probing Ligand Removal and Ordering at Quantum Dot Surfaces Using Vibrational Sum Frequency Generation Spectroscopy", *J. Colloid Interface Sci.* **2019**, *537*, 389.

[46] M. J. Turo, X. Shen, N. K. Brandon, S. Castillo, A. M. Fall, S. T. Pantelides, J. E. Macdonald, "Dual-Mode Crystal-Bound and X-Type Passivation of Quantum Dots", *Chem. Commun.* **2016**, *52*, 12214.

[47] J. H. Dunlap, N. P. Jayaweera, P. J. Pellechia, A. B. Greytak, "Competitive Anionic Exchange of Thiolate Ligands onto Aqueous Phosphonate-Capped Quantum Dots", *J. Phys. Chem. C* **2022**, *126*, 17635.

[48] C. A. Huang-Zhu, J. K. Sheavly, A. K. Chew, S. J. Patel, R. C. Van Lehn, "Ligand Lipophilicity Determines Molecular Mechanisms of Nanoparticle Adsorption to Lipid Bilayers", *ACS Nano* **2024**, *18*, 6424.

[49] T. A. Wassenaar, H. I. Ingólfsson, R. A. Böckmann, D. P. Tieleman, S. J. Marrink, "Computational Lipidomics with Insane: A Versatile Tool for Generating Custom Membranes for Molecular Simulations", *J. Chem. Theory Comput.* **2015**, *11*, 2144.

[50] A. J. Metso, H. Zhao, I. Tuunainen, P. K. J. Kinnunen, "Observation of the Main Phase Transition of Dinervonoylphosphocholine Giant Liposomes by Fluorescence Microscopy", *Biochim. Biophys. Acta Biomembr.* **2005**, *1713*, 83.

[51] I. Reviakine, M. Gallego, D. Johannsmann, E. Tellechea, "Adsorbed Liposome Deformation Studied with Quartz Crystal Microbalance", *J. Chem. Phys.* **2012**, *136*, 84702.

[52] A. Adan, M. Lion, C. A. Huang-Zhu, S. Yudovich, A. Ayelet, G. Asaf, R. C. Van Lehn, W. Shimon, "Long-chain lipids facilitate insertion of large nanoparticles into membranes of small unilamellar vesicles", *bioRxiv* **2024**.

[53] P. Gkeka, P. Angelikopoulos, L. Sarkisov, Z. Cournia, "Membrane Partitioning of Anionic, Ligand-Coated Nanoparticles Is Accompanied by Ligand Snorkeling, Local Disordering, and Cholesterol Depletion", *PLoS Comput. Biol.* **2014**, *10*, e1003917.

[54] F. Lolicato, L. Joly, H. Martinez-Seara, G. Fragneto, E. Scoppola, F. Baldelli Bombelli, I. Vattulainen, J. Akola, M. Maccarini, "The Role of Temperature and Lipid Charge on Intake/Uptake of Cationic Gold Nanoparticles into Lipid Bilayers", *Small* **2019**, *15*, 1805046.

[55] A. K. Chew, R. C. Van Lehn, "Effect of Core Morphology on the Structural Asymmetry of Alkanethiol Monolayer-Protected Gold Nanoparticles", *J. Phys. Chem. C* **2018**, *122*, 26288.

[56] T. J. Piggot, J. R. Allison, R. B. Sessions, J. W. Essex, "On the Calculation of Acyl Chain Order Parameters from Lipid Simulations", *J. Chem. Theory Comput.* **2017**, *13*, 5683.

[57] S. Trabelsi, S. Zhang, T. R. Lee, D. K. Schwartz, "Linactants: Surfactant Analogues in Two Dimensions", *Phys. Rev. Lett.* **2008**, *100*, 037802.

Chapter 6

Tunable electrostatic interactions of lipid-coated quantum dots with biological membranes[1]

6.1 Introduction

Quantum dots (QDs) are semiconductor nanocrystals that are widely employed in biological research as fluorescence imaging tools due to their unique optical properties[1–4].

QDs exhibit several significant advantages over organic dyes. Their tunable core sizes (1–10 nm) allow for a wide range of fluorescence emission peaks with symmetric and narrow spectra. QDs exhibit very broad absorption spectrums, which make them ideal for multiplexed biosensing applications – multiple color QDs can be excited at a single wavelength. Also, QDs can be efficiently excited far from their emission spectra, reducing background and scattering contributions. Moreover, QDs have far greater extinction coefficient, quantum yield, and photostability as compared to their organic dyes counterparts[5].

Although QDs have many advantages as probes for bioimaging, a drawback is their surface hydrophobicity, which is imparted by nonpolar capping ligands used during synthesis. As a result, QDs need to be functionalized by additional steps in order to render them water-soluble. Multiple functionalization approaches for improved aqueous solubility and colloidal stability have been introduced[6, 7]. One such approach involves ligand exchange, in which the hydrophobic capping surface ligands are replaced by hydrophilic bi-functional ligands[2, 4, 5, 8, 9]. However, ligand exchange should not compromise their optical capabilities: after

[1]This chapter is adapted with permission from Morgenstein, Huang-Zhu, Van Lehn, and Weiss, Tunable electrostatic interactions of lipid-coated quantum dots with biological membranes, manuscript in preparation. Supporting Information (SI) referenced will be available in the forthcoming publication.

ligand exchange, QDs need to maintain high photostability as well as enhanced brightness. This is a difficult task since ligand exchange can permanently modify QD surfaces, thereby altering their photophysical properties.

Another functionalization approach involves adsorption of amphiphilic molecules such as block copolymers or phospholipid micelles[10–13] while maintaining the original hydrophobic as-synthesized ligands on the surface. In both approaches (ligand exchange or adsorption), further steps could involve bioconjugation of molecular recognition molecules (such as antibodies, Streptavidin, or other proteins) suitable for fluorescent labeling; such functionalized water-soluble QDs constructs are widely available commercially.

Efficient incorporation of QDs into biological membranes can offer unique possibilities for cell membrane engineering. One application of membrane-inserted nanocrystals is for optical observation of membrane potential. Voltage-sensitive semiconductor nanoparticles (NPs), displaying the quantum-confined stark effect (QCSE)[14], offer superior properties as membrane potential sensors. Analogous to the atomic Stark effect, the bandgap of semiconductor nanocrystals may be altered as a result of local electric fields inside polarized biological membranes during an action potential, which in turn translates into changes in fluorescence quantum yield, lifetime, and peak emission wavelength[15, 16]. Such QDs could potentially function as a membrane potential sensor[14]. Recently, rod-shaped nanocrystals termed nanorods (NRs) have been used as optical probes for membrane potential[17], Ludwig, et al.[18]. When compared to contemporary organic voltage sensitive dyes (VSDs), voltage sensitive QDs have superior characteristics as membrane potential sensors. They (1) have substantially higher voltage sensitivity, (2) are very bright and afford single molecule detection, (3) display a large spectral shift as function of voltage, (4) have a very fast response, and (5) do not bleach, allowing them to be used at very low concentration. Delivery of voltage sensitive QDs into the cell membrane is a fundamental prerequisite for the successful application of these nanoparticles as membrane potential sensors in biological applications.

Here, we developed a lipid coating technology that controls QD surface properties to promote QD adsorption to the cell membrane. In order to control the particle interaction with the membrane, we optimized the lipid-coated QDs (lcQDs) by controlling lipid composition; lipids vary by their hydrophobic alkane chain, which affects their phase transition and fluidity, and their head group, which affects their charge. We chose 1,2-dimyristoyl-*sn-glycero*-3-phosphocholine (DMPC) as the zwitterionic component and 1,2-dioleoyl-3-trimethylammonium-propane (DOTAP) as the cationic component for simplicity and to allow for better lcQD colloidal stability[7, 19]. We prepared lcQD constructs with varying compositions of lipids per QD particle to control the lcQDs' effective surface charge through lipid self-assembly. Fluorescence activated cell sorting (FACS) experiments revealed that the strength of interaction between positively charged lcQDs and HEK cells correlates to the initial DOTAP

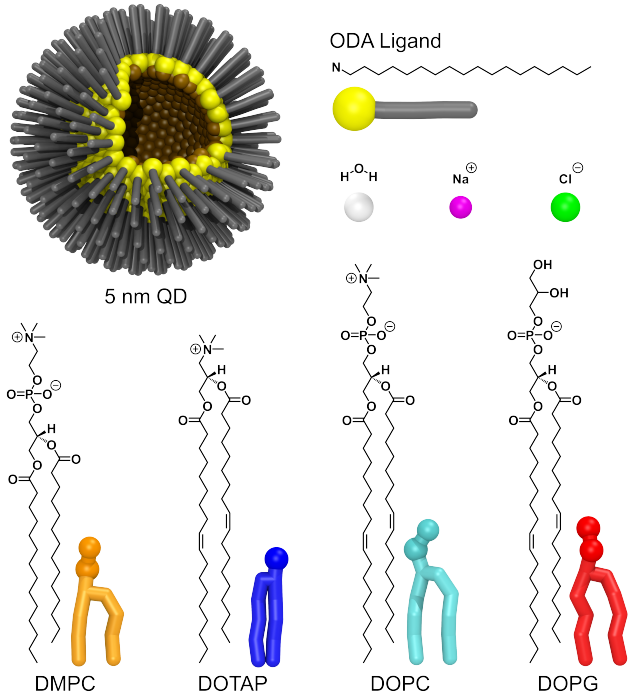


Figure 6.1: Molecular models used in this study. The CdSe/ZnS QDs capped with octadecylamine (ODA) ligands are colored as follows: CdSe/ZnS shell – tan, ODA propylamine – yellow, ODA alkyl – grey; a portion of the ligands were omitted to show the hollow shell. Lipids are colored as follows: DMPC modeled as DLPC in the Martini force field – orange, DOTAP – blue, DOPC – cyan, DOPG – red. Water, sodium, and chloride are colored white, purple, and green, respectively. This color scheme is used throughout the rest of this manuscript.

concentration during lcQD preparation. Finally, we used classical molecular dynamics (MD) simulations to show that positively charged lcQDs adsorb to a negatively charged model membrane composed of 1,2-dioleoyl-*sn-glycero*-3-phosphocholine (DOPC) and 1,2-dioleoyl-*sn-glycero*-3-phosphoglycerol (DOPG) through a local enrichment of anionic lipids and the displacement of salt ions at the NP-membrane interface. Chemical structures and molecular models of the QD and lipids used are shown in Figure 6.1.

6.2 Methods

6.2.1 Preparation of lcQDs for electrostatic interaction estimation

A series of lcQDs with different compositions of surface lipids were prepared and characterized for hydrodynamic size by dynamic light scattering (DLS), surface charge by ζ-potential, and relative normalized brightness by absorption and emission spectrums (SI). To study the electrostatic effect on the interaction of lcQDs with a biological membrane, a series of lcQDs with the same total amount of lipids per particle but with different percentage of a cationic lipid (with respect to total lipid amount) were prepared. Members of this series spanned ζ-potentials from +7mV to +37mV. DOTAP was the used as the charged lipid component in

the lipids mixture to grant a positive charge to the lcQDs and enable adsorption to negatively charged biological membranes.

6.2.2 Studying lcQDs-membrane interactions by FACS

For FACS studies, the membrane of human embryonic kidney 293 cells (HEKs) cells was chosen as a model system. FACS was chosen as a screening / evaluation tool to estimate, by fluorescence brightness, the amount of lcQDs interacting with the membrane. All experiments were conducted with a fixed concentration and volume of lcQDs. HEK cells were stained with same concentrations and volumes of these lcQDs and analyzed by FACS to quantify the staining efficiency.

6.2.3 Electrostatic interactions

To quantify electrostatic interactions, lcQDs of the series mentioned Section 2, with same amount of total lipids at full encapsulation but different ratios of DMPC/DOTAP were prepared. We were able to keep the lcQDs water soluble for $0.1 <$ DOTAP/total lipids < 0.5, yielding overall positive ζ-potentials in the range of +7mV to +37mV, while keeping the same number of lipids per particle. This ensures that the hydrophobic interaction is the same for the series, and hence differences in levels of staining are only due to electrostatic interactions (positively charged lcQDs with negatively charged membrane).

Figure B shows that the level of staining is directly proportional to the DOTAP/total lipids ratio: the higher the (positive) ζ-potential is, the higher the cell staining of the particles. The surface charge of a particle influences its solubility and colloidal stability, and can promote membrane adsorption followed by insertion. However, membrane fusion may be hindered by the strong electrostatic interactions of highly charged polar ligands on the particle surface.

The results described above could be further corrected for relative brightness changes due to charged lipids quenching the QDs fluorescence. Indeed, relative brightness measurements (normalized Fl/O.D. values for the brightest construct, a least positive constructs, Fl – integral of total emission spectrum, O.D. optical density of at the excitation wavelength) exhibited reduced QY per particle as function of increased DOTAP/total lipids ratio. This quenching, due to electron transfer, is a well-known phenomena[20, 21]. Fig. S2 show the results of 1A with this correction. Considering the reduction in emission for high zeta QDs the actual 'membrane labeling' is higher, this correction allows for even better separation of FACS histograms based on surface charge.

6.2.4 Simulations of lipid self-assembly on QDs

We simulated the self-assembly of lipids on the surface of QDs using coarse-grained (CG) simulations with the Dry Martini[22] force field. This force field builds upon the explicit solvent version of Martini[23–27] by recalibrating the original interaction matrix of Lennard Jones (LJ) potentials to forego the need to model water explicitly and speed up simulations by up to two orders of magnitude. Since Dry Martini excels at reproducing lipid properties and modeling events primarily driven by the hydrophobic effect, we found it suitable to use for our lipid self-assembly protocol with large (5 nm diameter) QDs. A leap-frog stochastic dynamics integrator with a timestep of 20 fs was used with the neighbor list constructed every 10 steps using the Verlet scheme and a cutoff of 1.4 nm. Van der Waals interactions were modeled using a cutoff scheme with the force switched to zero from 0.9 nm to 1.2 nm. Electrostatic interactions were modeled using a cutoff scheme with the potential shifted to zero at 1.2 nm. The dielectric constant was set to 15. Simulations were performed in the *NVT* ensemble at 300 K. The CG models for the QDs and DOTAP were taken from our previous work[28]. DMPC was represented with the DLPC Martini model. Molecular dynamics (MD) simulations were performed with the GROMACS package, version 2023.[29]

A single QD was centered in a 50 nm × 50 nm × 50 nm box and lipids were inserted in random positions. The system was neutralized by inserting the corresponding number of counterions. Due to the stochastic nature of lipid self-assembly, convergence assessment was non-trivial; we therefore performed simulations for 3,000 ns – a total simulation time that yielded consistent behavior across multiple systems after several trial runs. Configurations were saved every 1 ns. At the end of each simulation, we observed the lcQD along with a few lipid vesicles; the lcQD was subsequently extracted for further analyses and excess lipids were removed. Four replicates were performed for each system for statistics. The solvent-accessible surface area (SASA)[30] and the total number of adsorbed lipids were calculated and used as a proxy for convergence. A schematic of this procedure and detailed information on the topology of each system and replicate are provided in the SI. This protocol was performed for 2 nm and 5 nm diameter QDs.

6.2.5 Simulations of lcQD-membrane interactions

We used the explicit solvent CG force field Martini[26], version 2.3[23] with the refined polarizable water model[24] to study the interactions between positively charged lcQDs and negatively charged lipid membranes. All explicit solvent simulations were performed with a leap-frog integrator and a timestep of 20 fs. The neighbor list was constructed every 20 steps using a Verlet scheme with a cutoff of 1.225 nm. Van der Waals interactions were modeled using a cutoff scheme with the potential shifted to zero at 1.1 nm. Electrostatic interactions

were modeled using the smooth Particle-Mesh-Ewald with the potential shifted from to zero at 1.1 nm, 4^{th} order interpolation, and a Fourier spacing of 0.12 nm. The dielectric constant was set to 2.5. The temperature was controlled at 300 K using the velocity-rescale thermostat coupling every 1 ps. Equilibration simulations in the *NPT* ensemble were performed with semi-isotropic pressure coupling using the Berendsen barostat coupling the pressure every 5 ps. For production simulations, we switched to the Parrinello-Rahman barostat coupling the pressure every 12 ps. MD simulations were performed with the GROMACS package, version 2023.[29]

Out of the four replicates performed for the self-assembly simulations with $\chi_{DOTAP,overall}$ of 50%, the replicate that showed full encapsulation with the largest number of adsorbed lipids was selected for these sets of simulations. The replicates selected from the simulations with $\chi_{DOTAP,overall}$ of 10% and 90% were the ones that showed full encapsulation and the number of adsorbed lipids closest to that of the 50% DOTAP lcQD. We solvated the extracted 2 nm diameter lcQDs with an 18 nm × 18 nm membrane in a 24 nm tall box with approximately 50,000 polarizable water molecules[24], 150 mM NaCl, and counterions to neutralize the charged lipid coating. The lcQD was randomly oriented and positioned so that the minimum distance between the surface of the lipid coating and the surface of the membrane was approximately 2 nm. The three coordinates of all beads that compose the QD core were restrained with a 1,000 $kJ{\cdot}mol^{-1}{\cdot}nm^2$ during equilibration simulations to prevent translation. The energy of the system was minimized and followed by a 1 ns *NVT* simulation to equilibrate the solvent. Subsequently, a 10 ns NPT simulation was performed to allow the lipid membrane to relax. After equilibration, the position restraints were released and a 50 ns production simulation was performed, sampling every 50 ps. A total of 16 independent replicates were performed for each of the 10%, 50%, and 90% DOTAP lcQDs, with each replicate having unique initial configurations and velocities.

6.3 Results and Discussion

6.3.1 Lipid mixture composition controls electrostatic properties of lcQDs

We began our study by tuning the initial lipid composition using lcQD preparation to identify the optimum concentration that achieves full encapsulation of QDs. Briefly, we mixed commercial 5 nm and 11 nm diameter octadecylamine-capped CdSe/ZnS QDs into a 1:1 solution of DMPC:DOTAP at various initial lipid concentrations (*i.e.*, to control the total number of lipids in solution). An excess of cholate surfactant was added to solubilize the lipids. We measured the ζ-potential of the resulting lcQDs (Figure 6.2) to assess their colloidal stability. For both QD sizes, we found that the ζ-potential plateaus above size-dependent lipid-to-particle ratios. We interpreted this plateau as indicating full encapsulation of the

QDs and resulting saturation of the QD surface charge since incorporation of additional lipids into the ligand monolayer would reflect a change in the ζ-potential. Based on the conclusions of our previous work,[28] where we demonstrated that lipids intercalate into the ligand monolayer to fill free volume, and on the fact that here we add an excess of cholate as a detergent, we assume that multilayered lipid structures[31, 32] are not formed on the QD surface nor over the self-assembled lipid monolayer. After determining the lipid concentrations that yield full encapsulation of the QDs, we further screened to see if the initial concentration of DOTAP, χ_{DOTAP}, had any effect on the lcQDs' effective surface charge. We again prepared lcQD constructs, but this time varied χ_{DOTAP} from 0.1 to 0.5 and measured their ζ-potential. Figure 6.2 shows that increasing the initial concentration of cationic lipids increases the ζ-potential of the lcQDs, indicating increased positive surface charge and increased stability in solution.

6.3.2 Self-assembly simulations reveal structures of lipid coatings

To investigate how χ_{DOTAP} influences the self-assembled lipid coating on the QD, we performed coarse-grained MD simulations. To achieve system sizes needed to model lipid self-assembly onto the QD surface, we modeled the lipid self-assembly process using the Dry Martini force field.[22] Dry Martini is an implicit solvent force field that has interactions parameterized to capture the hydrophobic effect, and has been shown to reproduce related processes such as vesicle self-assembly and fusion, in food agreement with more detailed models. Since our experiments showed similar trends for the 5 nm and 11 nm diameter QDs, albeit with a larger magnitude for the larger QDs, we chose to model lipid self-assembly on the 5 nm QD to minimize computational expense. The coarse-grained model for the ODA-capped CdSe/ZnS QD was taken from our previous work[28]. The computational workflow mimicked experimental protocols by adding DMPC and DOTAP in a 1:1 ratio into the simulation box to identify the lipid concentration that yields fully encapsulated lcQDs.

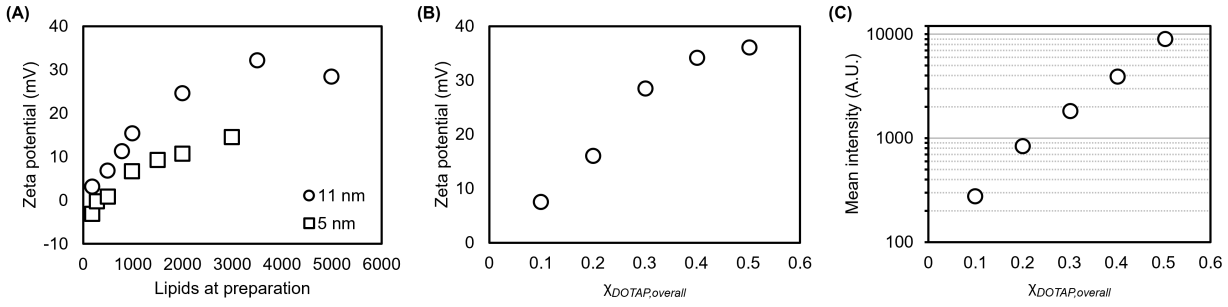


Figure 6.2: (A) ζ-potential as a function of total lipids at preparation (B) ζ-potential of 11 nm QDs as a function of DOTAP/total lipids ratio (C) Mean intensity for 11 nm lcQDs

We then performed simulations with the optimal lipid concentration but varying the initial concentration of DOTAP ($\chi_{DOTAP,overall}$). Additional details are provided in the Methods seection.

For simplicity and to eliminate NP self-aggregation effects, we assumed maximum solubility of the QDs and modeled a single QD in the simulation box. The cholate surfactant was not included in the simulations, which is similar to previous molecular simulations that investigated the interactions between lipid-coated NPs and biological membranes under the assumption of a surfactant-free lipid monolayer (i.e., purely trimethylammonium lipids or phospholipids) and by defining a number of adsorbed lipids *a priori*.[33] Experimentally, the lcQDs are washed after preparation which is expected to readily remove cholate due to its surfactant nature and small molecular size, leaving surfactant-free lipid coatings. To support this assumption, Thermogravimetric Analysis-Mass Spectrometry was performed to measure the surfactant concentration and showed unmeasurable trace amounts.

Figure 6.3A shows that the concentration of DOTAP in the simulated surface lipid coating ($\chi_{DOTAP,surface}$) does not change as the initial lipid concentration increases (total lipids in the mixture during preparation). This invariance suggests that the initial concentration of cationic lipids indeed determines the effective surface charge of the lcQDs. We show that adding 500 total lipids yields partially encapsulated lcQDs, while fully encapsulated particles are observed at 1,500 total lipids and above. Encapsulation was assessed by quantifying the total number of lipids that composed the lipid coating along with the solvent-accessible surface area (SASA) of the QD (see SI). Even though the QD's average SASA decreased as we increased the total number of lipids, indicating encapsulation, at significantly high initial lipid concentrations, inconsistent lipid coatings were observed (simulation snapshots in Figure 6.3A). When the self-assembly process was initiated with at least 2,000 total lipids, we obtained lcQDs coated with multilayer lipid structures. Visual inspection (see SI) revealed that the multilayer structures are similar to vesicle hemifusion states[31, 32] where the lipid coating partly fuses with a vesicle only through the outer leaflet and forms a hydrophilic pocket. These structures are expected to be high energy states because of the hydrophilic pocket and the lipid line tension formed by the irregular lipid arrangement. Further visual inspection revealed that the first step leading to the formation of these multilayer structures is the fusion of a vesicle that self-assmebles in solution with the lcQD; the size of the vesicle and the number of lipids in the self-assembled lipid monolayer then dictates the shape of the lcQD construct (*e.g.*, large vesicles lead to the lcQD from the 4,000 total lipids simulation). These structures are not surprising since they are consistent with observations during the initial stages of the experimental protocol. However, during the experiments, the formation of multilayer structures was addressed and eliminated with the addition of cholate to solubilize self-assembled vesicles and a filtration step to remove any multilayer structure that may have

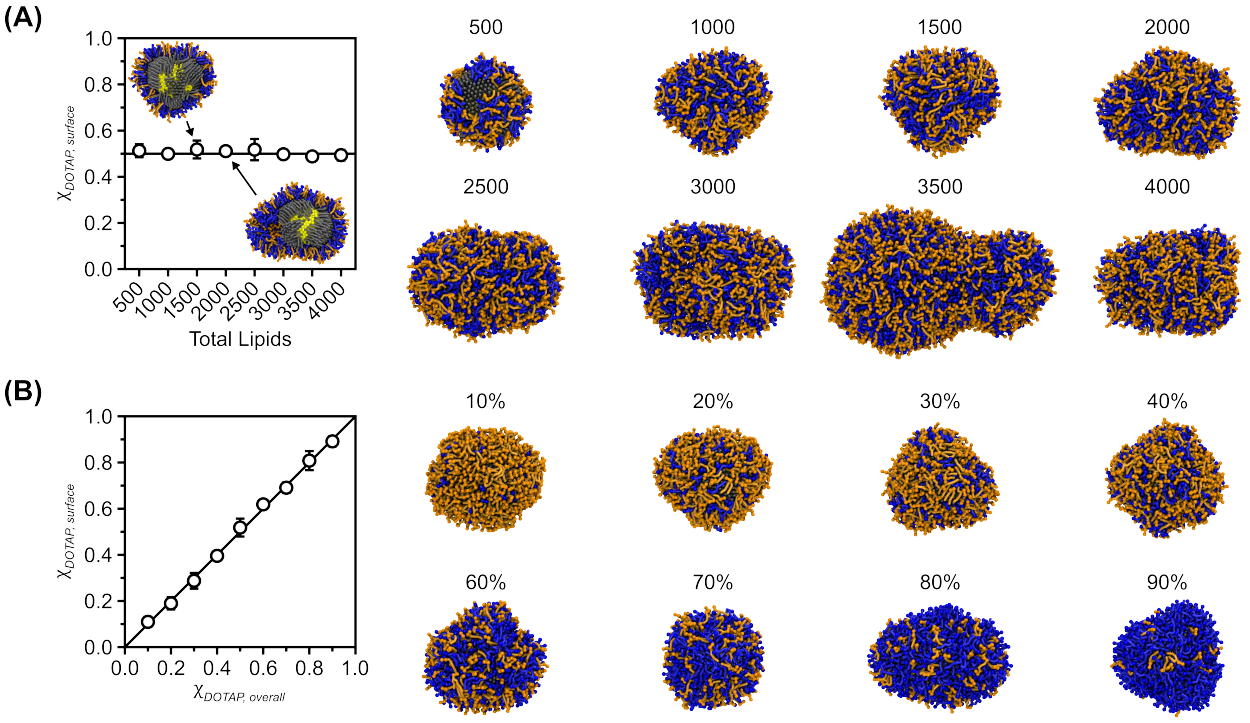


Figure 6.3: Encapsulation efficiency and surface charge of QDs is controlled by initial lipid compositions. (A) Fraction of DOTAP in the lipid coating as a function of the total number of lipids in solution and representative snapshots of the resulting lipid-coated QDs. (B) Fraction of DOTAP in the lipid coating as a function of the DOTAP concentration in solution and representative simulation snapshots of the resulting lipid-coated QDs. All simulation snapshots in this figure and in the rest of the manuscript were rendered using the Visual Molecular Dynamics software[34], release 1.9.4a55. The error in (A) and (B) was computed as the standard deviation between four replicates.

been formed.

After identifying the total number of lipids per particle that consistently yields fully encapsulated lcQDs and fewer multilayer structures (1,500 lipids per particle) from Figure 6.3A, we screened the effects of varying $\chi_{DOTAP,overall}$ (*i.e.*, DOTAP concentration in the initial lipid mixture) in Figure 6.3B. We found that $\chi_{DOTAP,surface}$ varies linearly with $\chi_{DOTAP,overall}$, in agreement with our previous hypothesis from experimental observations and Figure 6.3A. Simulation snapshots reveal that lipids intercalate into the ligand monolayer to ensure hydrophobic voids are filled with lipid tails. After these voids are filled, additional lipids adsorb over the remaining exposed alkyl chains to ensure full encapsulation, and in the process, lipid tails become intercalated within the lipid coating in an interlocked fashion to prevent their desorption (see SI). While the experimental ζ-potential appears to deviate from linearity at a high value of χ_{DOTAP}, the encouraging agreement between experimental and computational trends suggest that the simulated structural organization of lipids on the lcQD surface is reasonable and that overall surface charge of lcQDs is controlled by tuning the initial concentration of lipids during the preparation step.

In the following sections, we present data to study the mechanisms of adsorption for positively charged lcQDs, under the assumption that the fully saturated lcQDs from experiments are equal to the simulated lcQDs with regard to lipid coating composition and lipid arrangement. Our combined experimental and molecular modeling approach suffices to achieve tunable lcQDs and provides mechanistic insight into the molecular arrangement of the lipid coating and their nano-membrane interactions.

6.3.3 Lipid coating dictates interactions between lcQDs and HEK cells

To assess the effect of χ_{DOTAP} on lcQDs' functionality, we performed FACS experiments using HEK cells. These cells have an anionic outer membrane leaflet, representing an ideal platform to test the lcQDs' interaction strength with cell membranes. Cells were incubated with a series of variable-charge lcQD constructs diluted to the same concentration and washed with PBS buffer, lcQDs that interact strongly with the cell membranes are expected to remain adsorbed (*i.e.*, staining). The resulting solutions were then run in FACS to analyze the fluorescence intensity of each single cell. Stained cells will emit a fluorescent signal due to the adsorbed/membrane intact quantum dots that emit in the 600 nm region. Since cell staining is surface charge dependent, staining intensity is expected to increase with the lcQDs' surface charge. FACS analysis was performed on 10,000 cells for each lcQD construct to create the cell population emission histogram. Increasing the surface charge of the lcQDs (*i.e.*, by increasing χ_{DOTAP}) decreased their brightness, dividing the fluorescence signal to O.D relatively to the brightest construct showed by the lowest ζ-potential lcQDs- considering this effect and correction to relative brightness will increase the histograms separation further, The measured intensities in Figure 6.4 reveal an exponential increase of up to four orders of magnitude compared to unstained cells as a function of the lcQDs' ζ-potential. These data demonstrate that by simply tuning the initial lipid composition, we can control the macroscopic properties of lcQDs and consequently their interactions with lipid membranes.

6.3.4 Simulations reveal unbiased lcQD adsorption to anionic membranes

We sought to provide mechanistic insight into how the surface lipid composition of lcQDs can amplify the staining intensity and efficiency. To better capture electrostatic interactions compared to the self-assembly simulations, we performed simulations of the lcQDs and a model lipid membrane (80% zwitterionic DOPC and 20% anionic DOPG) using an explicit solvent coarse-grained force field, Martini 2.3[23], using the refined polarizable water model[24]. Since using the 5 nm diameter QDs from Figure 6.3 to perform these simulations would be computationally expensive, we decided to use smaller 2 nm diameter QDs based on our previous observation that larger QDs exhibit qualitatively consistent trends.

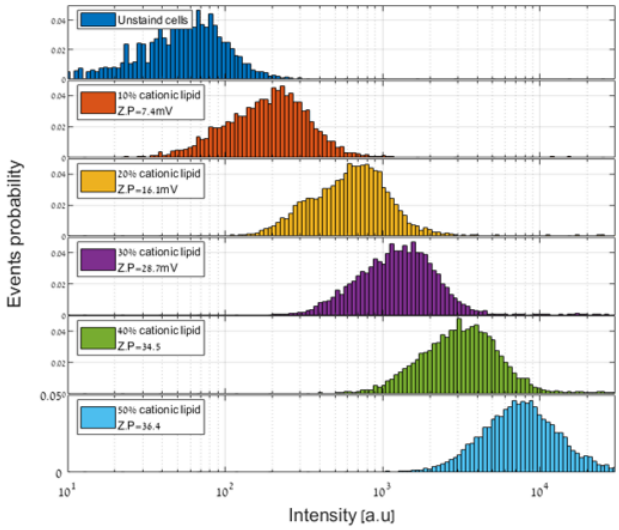


Figure 6.4: Flow cytometry results for HEK cells stained with a series of lcQDs with varying DMPC/DOTAP ratios (at fixed total # lipids per particle).

Self-assembly simulations yielded equivalent results for these QDs (see SI) from which we extracted lcQDs at three different values of $\chi_{DOTAP,overall}$ (10%, 50%, and 90%) that are representative of the whole range of DOTAP compositions.

Based on a preliminary set of simulations that showed variations in unbiased adsorption (*e.g.*, lcQDs would either partition to the membrane surface or into solution), we designed our simulation protocol around the quantification of unbiased adsorption events. Briefly, we placed each lcQD randomly oriented at a minimum distance of approximately 2 nm from the surface of an 18 nm $\times$ 18 nm membrane. The system was solvated with Martini polarizable water[25] and 150 mM NaCl; counterions were also added to neutralize the effective charge of the lcQD. For each of the lcQDs with $\chi_{DOTAP,overall}$ of 10%, 50%, and 90% we performed 16 $\times$ 50 ns unbiased simulations. This large number of unbiased simulations permitted the lcQDs to sample a variety of local membrane environments due to differences in initial configurations. Additional details are provided in the Methods section.

We computed the minimum distance between any lcQD bead and any membrane lipid bead throughout the simulation as a proxy for adsorption and observed large variations that reflected how strongly the lcQD interacts with the lipid membrane (see SI). Large fluctuations in these data indicate that the lcQD moves back and forth between the bulk solvent and the membrane interface, whereas small fluctuations within a minimum distance of 0.5 nm to 1.0 nm corresponds to the lcQD fluctuating at the membrane interface. In the latter case, there are weak interactions between lipids from the lipid coating and those from the membrane, as shown in Figure 6.5A, which slightly deforms the membrane, resulting in an average minimum distance of 0.50 nm over the last 5 ns for the simulation corresponding to Figure 6.5A. The deformation of the membrane is apparent from the plot of the lipid

number density, which shows pronounced negative curvature in the vicinity of the lcQD although with no notable lipid enrichment (*i.e.*, no increased local lipid density). This state reflects only a few positively charged DOTAP headgroups on the lcQD surface coordinating with the negatively charged headgroups from the membrane's DOPG. This contrasts with Figure 6.5B which shows DOTAP headgroups fully embedded within the headgroup region of the membrane, resulting in an average minimum distance of 0.44 nm over the last 5 ns for the simulation corresponding to Figure 6.5B. This intercalation is mediated by anionic DOPG lipids being localized at the NP-membrane interface and coordinating with the cationic DOTAP lipids, as shown by the local enrichment of lipid beads in the number density plot and without membrane deformation being induced.

6.3.5 Increasing DOTAP concentration promotes stronger membrane adsorption

Based on the variations of the minimum distance, we proceeded to establish cutoff values to determine whether a particular simulation replicate resulted in no membrane adsorption,

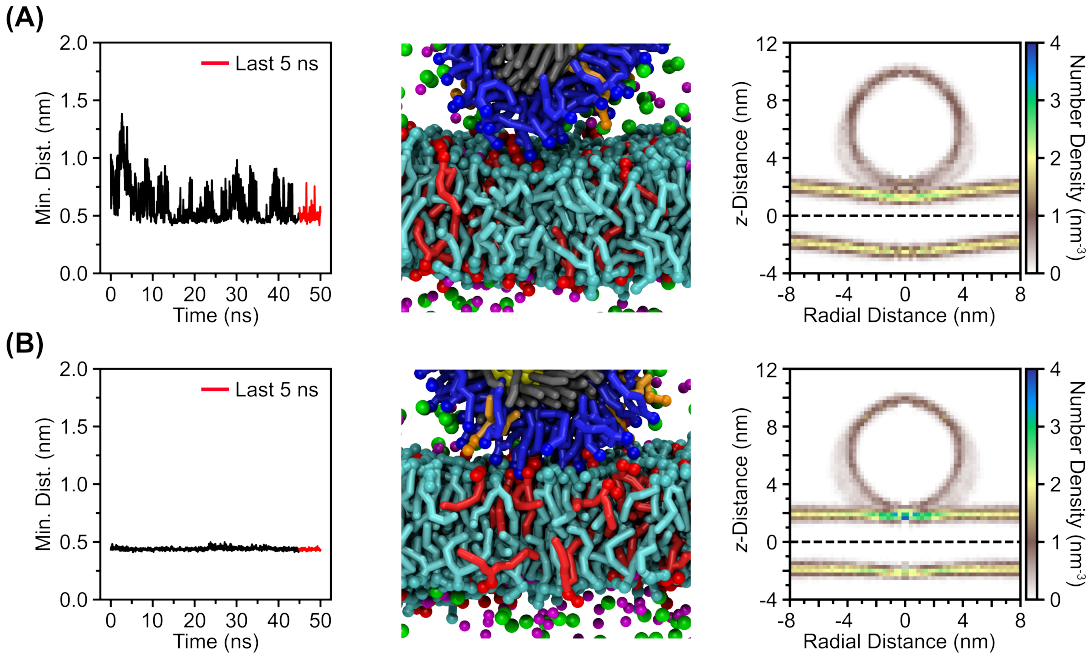


Figure 6.5: Minimum distance between lcQD and membrane correlates to local lipid enrichment. (A) Replicate in which weak adsorption is observed, and negative membrane curvature is induced. (B) Replicate in which strong adsorption is observed with a relaxed membrane and a local enrichment of lipid headgroups at the NP-membrane interface. Data correspond to lcQDs coated with a 90% DOTAP coating. Number density plots were generated using the phosphate headgroup of DMPC, DOPC, and DOPG; and the choline headgroup of DOTAP – bins were 0.26 nm in the radial dimension and 0.26 nm in the z-dimension with the coordinate system centered on the lcQD. Water molecules were omitted from the simulation snapshots for clarity.

weak adsorption, or strong adsorption (Figure 6.6A). Based on the number density plots, and the average minimum distance over the last 5 ns of simulation for each replicate, we identified that an average minimum distance between 0.50 and 0.90 nm was consistent with weak adsorption of the lcQD to the membrane. An average minimum distance greater than 0.90 nm was classified as no adsorption and a minimum distance less than 0.50 nm was classified as strong adsorption. Each replicate was classified according to these cutoff values, and their probability was computed in Figure 6.6B.

For lcQDs with a 10% cationic lipid coating, 69% of the replicates resulted in no adsorption and the remaining 31% resulted in weak adsorption; no replicate showed strong adsorption. For lcQDs with a 50% cationic lipid coating, only 25% of the replicates resulted in no adsorption; 69% of the replicates showed weak adsorption and the remaining 6% resulted in strong adsorption. Finally, for lcQDs with a 90% cationic lipid coating only 6% of the replicates showed no adsorption and 19% showed weak adsorption; the remaining 75% showed strong adsorption. These trends generally agree with our experimental FACS measurements (Figure 6.4) by showing that increasing the effective surface charge of the cationic lcQDs promotes stronger adsorption to the anionic membrane. The calculated probabilities for each state (Figure 6.6B) relative to each other are also in agreement of our hypotheses. The lcQDs with a 10% cationic surface charge showed no replicate where the QDs adsorbed strongly, and the opposite is observed for a 90% cationic surface charge where only once did the lcQD partition into solution.

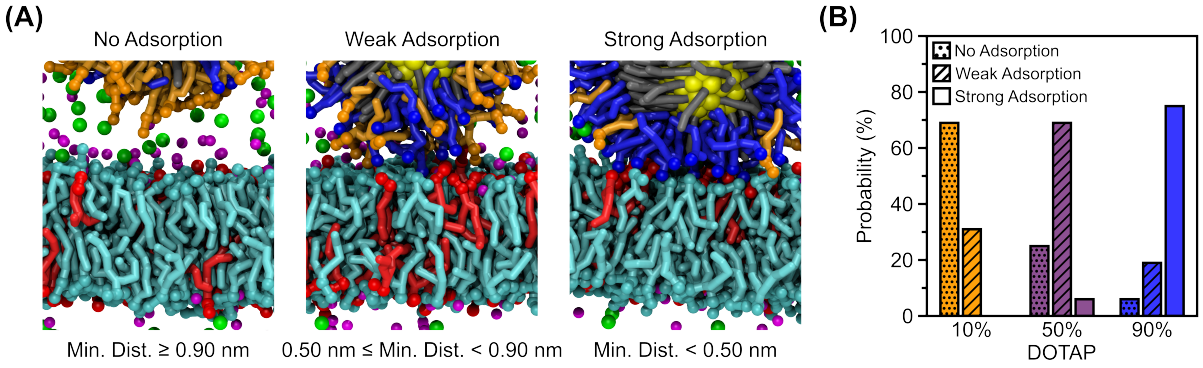


Figure 6.6: Effective surface charge of lcQDs determines strength of adsorption. (A) Simulation snapshots representative of the three adsorbed states we investigate. (B) Probability of observing no adsorption, weak adsorption, or strong adsorption within the ensemble of simulations for lcQDs with lipid coatings of 10%, 50%, and 90% DOTAP (16 simulations in each ensemble). Water molecules were omitted from the simulation snapshots for clarity.

6.3.6 Lipid-lipid interactions and displacement of ions drive lcQD adsorption

Since Figure 6.6 suggests electrostatic-mediated adsorption of lcQDs despite the relatively high salt concentration (150 mM) which is expected to screen these interactions, we further investigated potential descriptors that may be driving this process. In Figure 6.7 we quantified the number of charged species within the NP-membrane interface for each of the most probable adsorbed states of Figure 6.6B (*i.e.*, the ensemble of simulations for 10% DOTAP – No Adsorption, 50% DOTAP – Weak Adsorption, and 90% DOTAP – Strong Adsorption). This approach ensures that each state is described with accurate statistics by averaging over multiple independent trajectories. The interface region was defined as the cylindrical region between the center of mass of the QD and the midplane of the membrane with a radius equal to the average effective radius of the lipid coating headgroups relative to the center of the QD (see SI).

Figure 6.7A shows that DOPG lipids in the membrane reorganize over the simulation timescale in order to increase the DOPG density at the lcQD-membrane interface to enable strong adsorption for the lcQDs with a 90% cationic lipid coating; this enrichment is not observed for the other two lcQDs since the DOPG density is constant throughout the 50 ns timescale. This observation indicates that favorable DOPG-DOTAP electrostatic interactions drive changes to lipid organization at the lcQD-membrane interface. However, DOTAP rearrangement within the lipid coating is negligible for all lcQDs as suggested by Figure 6.7B, which suggests that lipid mobility within the ligand monolayer might be restricted or limited. For the lcQDs with the 90% lipid coating, the enrichment of anionic lipids at the QD-membrane interface leads to a corresponding displacement of chloride and sodium ions as shown in Figures 6.7C and 6.7D. The data in Figure 6.7C show first that the local density of chloride ions follows trends in the DOTAP content, with higher densities initially present in the region between the lcQD and membrane for higher DOTAP content since the chloride ions compensate for the cationic DOTAP charge. The chloride ion density substantially decreases for the strongly adsorbing lcQDs with the 90% DOTAP content while remaining minimally changed for the weakly adsorbed lcQDs with the 50% DOTAP coating. Figure 6.7D shows that the initial local densities of the sodium ions are similar for all three lcQDs because this density is defined by the DOPG content of the membrane. Similar to the chloride iones, the sodium ion density decreases for the strongly adsorbing lcQDs with a 90% DOTAP coating and is effectively unchanged for the lcQDs with the 50% DOTAP coating. The local densities of both chloride and sodium ions for lcQDs with a 10% DOTAP coating increase throughout the simulation due to the larger region that can accomodate these ions as the lcQD diffuses away from the membrane.

The displacement of counterions along with the increased adsorption strength observed for the lcQDs with a 90% DOTAP is consistent with the counterion release mechanism, which

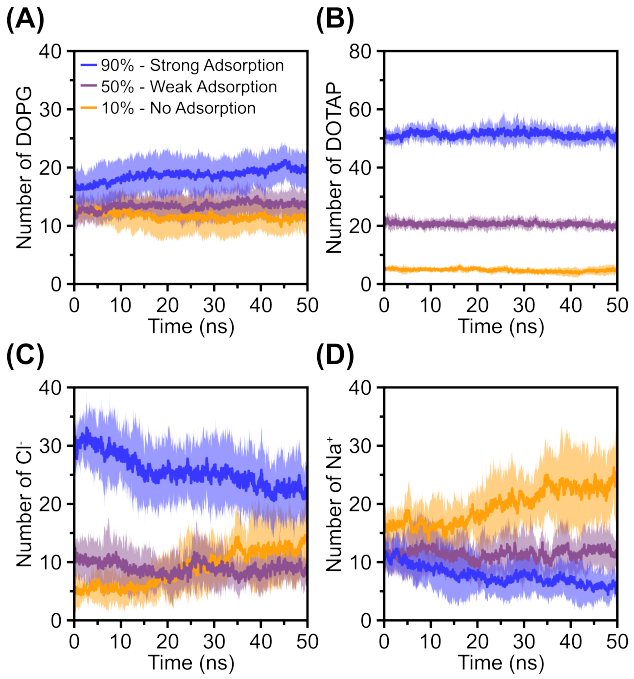


Figure 6.7: Average local density of charged species within the cylindrical region centered at the NP-membrane interface. The error was computed as the standard deviation within each ensemble of simulations (*i.e.*, 11 replicates for lcQDs with either a 10% or 50% DOTAP lipid coating and 12 replicates for lcQDs with a 90% DOTAP lipid coating).

is a common driving force in the complexation of different oppositely charged biomolecules (*e.g.*, protein, DNA, lipid membranes)[35]. In this mechanism, the release of counterions that were initially confined to the region between the membrane and lcQD leads to an increase in ion translational entropy, with release possible due to the opposite-charged attraction between DOTAP and DOPG lipids. This effect also an then strengthen interactions between oppositely charged lipids (*i.e.*, DOTAP from the lipid coating and DOPG from the lipid membrane). Because this mechanism depends upon the number of counterions released and the concomitant interactions between oppositely charged lipids, it is observed only for the 90% DOTAP lcQDs which both have highh counterion densities and ample DOTAP-DOPG interactions. In contrast, the 10% DOTAP lcQDs are instead repelled from the membrane as an alternative mechanism of reducing confinement, thereby leading to the increased local density of counterions in Figure 6.7.

Our finding that counterion release explains the strong adsorption of highly charged cationic lcQDs is consistent with a previous study that showed that the binding probability of solid NPs coated with a fixed number of DOTAP molecules to DOPC:DOPS membranes increased almost 5-fold as the DOPS concentration was increased from 25% to 33% [33]. They also observed NP diffusion between bulk solvent and the membrane interface for the less anionic membrane, consistent with our observations (see SI). Moreover, membrane binding was proposed to be a two-step process, where the NP first approaches the membrane due to

electrostatic attraction between the lipid headgroups of the lipid coating and the membrane, followed by internalization initiated by lipid tail protrusions[36, 37] and lipid exchange. This two-step mechanism is qualitatively similar to what we observed in our simulations with the exception of the lipid exchange step. However, this is attributed to the fact that we performed short simulations of only 50 ns, compared to 5 µs in this previous study, and the exchange of lipids between the lipid coating and the lipid membrane occurs at long timescales due to the fusion-like behavior during the NP internalization process.

Thus, we anticipate that lipid reorganization and van der Waals interactions (*e.g.*, hydrophobic contact between lipid tails from the lipid coating and the lipid membrane) could eventually initiate a fusion-like event that ultimately leads to lcQD internalization into the membrane on timescales beyond those studied in these simulations that could impact the experimentally observed lcQD fluorescence intensity in Figure 6.4.

6.4 Conclusions

In this study we demonstrate a tunable methodology for functionalizing QDs with a lipid coating to achieve precise control over their interactions with biological membranes. By combining experimental observations with CG MD simulations, we establish mechanistic insight on the control of the lcQDs surface charge and subsequently, their staining efficiency by adjusting the lipids-to-particle stoichiometry during preparation.

ζ-potential measurements and MD simulations suggest that the effective surface charge of lcQDs increases with the concentration of cationic DOTAP lipids.

FACS experiments with HEK cells validated these findings, showing an increase in staining intensity as a function of surface charge. This confirms that electrostatics, mediated by lipid ratio and compositions at preparation play a primary driving force for lcQD–membrane interactions. Explicit solvent simulations further indicate that the release of counterions from the lcQD-membrane interface promotes strong adsorption for lcQDs with high cationic lipid contents.

Overall, this work combines experiments and simulations to demonstrate a facile approach to controlling the surface charge of nanoparticles through a self-assembled lipid monolayer. This enhanced tunability of surface properties is advantageous in the design of membrane-active biocompatible inorganic nanoparticles that can act as membrane potential sensors, bioimaging agents, and drug carriers.

References

[1] M. Bruchez, M. Moronne, P. Gin, S. Weiss, A. P. Alivisatos, "Semiconductor Nanocrystals as Fluorescent Biological Labels", *Science* **1998**, *281*, 2013–2016.

[2] X. Michalet, F. F. Pinaud, L. A. Bentolila, J. M. Tsay, S. Doose, J. J. Li, G. Sundaresan, A. M. Wu, S. S. Gambhir, S. Weiss, "Quantum Dots for Live Cells, in Vivo Imaging, and Diagnostics", *Science* **2005**, *307*, 538–544.

[3] W. C. W. Chan, D. J. Maxwell, X. Gao, R. E. Bailey, M. Han, S. Nie, "Luminescent quantum dots for multiplexed biological detection and imaging", *Current Opinion in Biotechnology* **2002**, *13*, 40–46.

[4] I. L. Medintz, A. R. Clapp, H. Mattoussi, E. R. Goldman, B. Fisher, J. M. Mauro, "Self-assembled nanoscale biosensors based on quantum dot FRET donors", *Nature Materials* **2003**, *2*, 630–638.

[5] U. Resch-Genger, M. Grabolle, S. Cavaliere-Jaricot, R. Nitschke, T. Nann, "Quantum dots versus organic dyes as fluorescent labels", *Nature Methods* **2008**, *5*, 763–775.

[6] K. Yang, G. Luo, X. Zeng, M. Xu, P. Pi, S. Xu, X. Wen, "Aqueous quantum dots with high fluorescence, colloidal stability and biocompatibility encapsulated by an amphiphilic fluorine copolymer", *Polymer* **2019**, *179*, 121706.

[7] P. T. Snee, "The Role of Colloidal Stability and Charge in Functionalization of Aqueous Quantum Dots", *Accounts of Chemical Research* **2018**, *51*, 2949–2956.

[8] F. Pinaud, D. King, H.-P. Moore, S. Weiss, "Bioactivation and Cell Targeting of Semiconductor CdSe/ZnS Nanocrystals with Phytochelatin-Related Peptides", *Journal of the American Chemical Society* **2004**, *126*, 6115–6123.

[9] D. Gerion, F. Pinaud, S. C. Williams, W. J. Parak, D. Zanchet, S. Weiss, A. P. Alivisatos, "Synthesis and Properties of Biocompatible Water-Soluble Silica-Coated CdSe/ZnS Semiconductor Quantum Dots", *The Journal of Physical Chemistry B* **2001**, *105*, 8861–8871.

[10] B. Dubertret, P. Skourides, D. J. Norris, V. Noireaux, A. H. Brivanlou, A. Libchaber, "In Vivo Imaging of Quantum Dots Encapsulated in Phospholipid Micelles", *Science* **2002**, *298*, 1759–1762.

[11] L. Groc, M. Heine, L. Cognet, K. Brickley, F. A. Stephenson, B. Lounis, D. Choquet, "Differential activity-dependent regulation of the lateral mobilities of AMPA and NMDA receptors", *Nature Neuroscience* **2004**, *7*, 695–696.

[12] D. S. Lidke, K. A. Lidke, B. Rieger, T. M. Jovin, D. J. Arndt-Jovin, "Reaching out for signals : filopodia sense EGF and respond by directed retrograde transport of activated receptors", *Journal of Cell Biology* **2005**, *170*, 619–626.

[13] Y. Guo, E. Terazzi, R. Seemann, J. B. Fleury, V. A. Baulin, "Direct proof of spontaneous translocation of lipid-covered hydrophobic nanoparticles through a phospholipid bilayer", *Science Advances* **2016**, *2*, e1600261.

[14] L. Zhang, B. Lv, H. Yang, R. Xu, X. Wang, M. Xiao, Y. Cui, J. Zhang, "Quantum-confined stark effect in the ensemble of phase-pure CdSe/CdS quantum dots", *Nanoscale* **2019**, *11*, 12619–12625.

[15] D. Dorfs, T. Franzl, R. Osovsky, M. Brumer, E. Lifshitz, T. A. Klar, A. Eychmüller, "Type-I and Type-II Nanoscale Heterostructures Based on CdTe Nanocrystals: A Comparative Study", *Small* **2008**, *4*, 1148–1152.

[16] D. Dorfs, A. Salant, I. Popov, U. Banin, "ZnSe Quantum Dots Within CdS Nanorods: A Seeded-Growth Type-II System", *Small* **2008**, *4*, 1319–1323.

[17] K. Park, Y. Kuo, V. Shvadchak, A. Ingargiola, X. Dai, L. Hsiung, W. Kim, Z. H. Zhou, P. Zou, A. J. Levine, J. Li, S. Weiss, "Membrane insertion of—and membrane potential sensing by—semiconductor voltage nanosensors: Feasibility demonstration", *Science Advances* **2018**, *4*, e1601453.

[18] A. Ludwig, P. Serna, L. Morgenstein, G. Yang, O. Bar-Elli, G. Ortiz, E. Miller, D. Oron, A. Grupi, S. Weiss, A. Triller, "Development of Lipid-Coated Semiconductor Nanosensors for Recording of Membrane Potential in Neurons", *ACS Photonics* **2020**, *7*, 1141–1152.

[19] S. Dante, A. Petrelli, E. M. Petrini, R. Marotta, A. Maccione, A. Alabastri, A. Quarta, F. De Donato, T. Ravasenga, A. Sathya, R. Cingolani, R. Proietti Zaccaria, L. Berdondini, A. Barberis, T. Pellegrino, "Selective Targeting of Neurons with Inorganic Nanoparticles: Revealing the Crucial Role of Nanoparticle Surface Charge", *ACS Nano* **2017**, *11*, 6630–6640.

[20] B. Nikoobakht, C. Burda, M. Braun, M. Hun, M. A. El-Sayed, "The Quenching of CdSe Quantum Dots Photoluminescence by Gold Nanoparticles in Solution", *Photochemistry and Photobiology* **2002**, *75*, 591–597.

[21] P. A. Linkov, K. V. Vokhmintcev, P. S. Samokhvalov, M. Laronze-Cochard, J. Sapi, I. R. Nabiev, "The Effect of Quantum Dot Shell Structure on Fluorescence Quenching By Acridine Ligand", *KnE Energy* **2018**, 194–201.

[22] C. Arnarez, J. J. Uusitalo, M. F. Masman, H. I. Ingólfsson, D. H. de Jong, M. N. Melo, X. Periole, A. H. de Vries, S. J. Marrink, "Dry Martini, a Coarse-Grained Force Field for Lipid Membrane Simulations with Implicit Solvent", *Journal of Chemical Theory and Computation* **2015**, *11*, 260–275.

[23] H. M. Khan, P. C. T. Souza, S. Thallmair, J. Barnoud, A. H. de Vries, S. J. Marrink, N. Reuter, "Capturing Choline–Aromatics Cation− Interactions in the MARTINI Force Field", *Journal of Chemical Theory and Computation* **2020**, *16*, 2550–2560.

[24] S. O. Yesylevskyy, L. V. Schäfer, D. Sengupta, S. J. Marrink, "Polarizable Water Model for the Coarse-Grained MARTINI Force Field", *PLOS Computational Biology* **2010**, *6*, e1000810.

[25] J. Michalowsky, L. V. Schäfer, C. Holm, J. Smiatek, "A refined polarizable water model for the coarse-grained MARTINI force field with long-range electrostatic interactions", *The Journal of Chemical Physics* **2017**, *146*, 054501.

[26] S. J. Marrink, H. J. Risselada, S. Yefimov, D. P. Tieleman, A. H. de Vries, "The MARTINI Force Field: Coarse Grained Model for Biomolecular Simulations", *The Journal of Physical Chemistry B* **2007**, *111*, 7812–7824.

[27] D. H. de Jong, G. Singh, W. F. D. Bennett, C. Arnarez, T. A. Wassenaar, L. V. Schäfer, X. Periole, D. P. Tieleman, S. J. Marrink, "Improved Parameters for the Martini Coarse-Grained Protein Force Field", *Journal of Chemical Theory and Computation* **2013**, *9*, 687–697.

[28] A. Marzouq, L. Morgenstein, C. A. Huang-Zhu, S. Yudovich, A. Atkins, A. Grupi, R. C. Van Lehn, S. Weiss, "Long-Chain Lipids Facilitate Insertion of Large Nanoparticles into Membranes of Small Unilamellar Vesicles", *Langmuir* **2024**, *40*, 10477–10485.

[29] D. Van Der Spoel, E. Lindahl, B. Hess, G. Groenhof, A. E. Mark, H. J. C. Berendsen, "GROMACS: Fast, flexible, and free", *Journal of Computational Chemistry* **2005**, *26*, 1701–1718.

[30] F. Eisenhaber, P. Lijnzaad, P. Argos, C. Sander, M. Scharf, "The double cubic lattice method: Efficient approaches to numerical integration of surface area and volume and to dot surface contouring of molecular assemblies", *Journal of Computational Chemistry* **1995**, *16*, 273–284.

[31] O. Regev, R. Backov, C. Faure, "Gold Nanoparticles Spontaneously Generated in Onion-Type Multilamellar Vesicles. Bilayers−Particle Coupling Imaged by Cryo-TEM", *Chemistry of Materials* **2004**, *16*, 5280–5285.

[32] A. Scheeder, M. Brockhoff, E. N. Ward, G. S. Kaminski Schierle, I. Mela, C. F. Kaminski, "Molecular Mechanisms of Cationic Fusogenic Liposome Interactions with Bacterial Envelopes", *Journal of the American Chemical Society* **2023**, *145*, 28240–28250.

[33] L. Ou, H. Chen, B. Yuan, K. Yang, "Membrane-Specific Binding of 4 nm Lipid Nanoparticles Mediated by an Entropy-Driven Interaction Mechanism", *ACS Nano* **2022**, *16*, 18090–18100.

[34] W. Humphrey, A. Dalke, K. Schulten, "VMD: Visual molecular dynamics", *Journal of Molecular Graphics* **1996**, *14*, 33–38.

[35] D. Harries, S. May, A. Ben-Shaul, "Counterion release in membrane–biopolymer interactions", *Soft Matter* **2013**, *9*, 9268–9284.

[36] R. C. Van Lehn, M. Ricci, P. H. J. Silva, P. Andreozzi, J. Reguera, K. Voïtchovsky, F. Stellacci, A. Alexander-Katz, "Lipid tail protrusions mediate the insertion of nanoparticles into model cell membranes", *Nature Communications* **2014**, *5*, 4482.

[37] C. A. Huang-Zhu, J. K. Sheavly, A. K. Chew, S. J. Patel, R. C. Van Lehn, "Ligand Lipophilicity Determines Molecular Mechanisms of Nanoparticle Adsorption to Lipid Bilayers", *ACS Nano* **2024**, *18*, 6424–6437.

Chapter 7

Conclusion

7.1 General Summary

In this thesis, I leveraged classical molecular dynamics simulations to model NP-membrane interactions at the coarse-grained scale and address length and time scale limitations from conventional all-atom simulations. Although there's an inherent trade-off with regard to chemical accuracy, the ability to model large systems while elucidating mechanistic and thermodynamic insight on molecular-scale events that occur at long time scales, and are rarely accessible with atomistic systems, provided invaluable insight for future design of surface-engineered NPs. This work has advanced the field by demonstrating that NP-membrane interactions are mediated by complex ligand-ligand, ligand-lipid, and lipid-lipid interactions rather than by simple single ligand descriptors. Hence, this thesis establishes design rules for applications where both NPs and membranes are active participants in cellular uptake. For ligand-grafted AuNPs, single ligand descriptors such as lipophilicity and chain architecture determine mechanisms of adsorption to lipid bilayers, and both must be considered when engineering NP surfaces. However, subsequent AuNP internalization is dominated by lipid membrane mechanics. For alkyl-capped QDs, membrane internalization can be maximized by minimizing the hydrophobic mismatch with the lipid bilayer, specifically using long-chain lipids that can minimize the line tension of the membrane induced by the large morphology of the QDs. Moreover, cellular internalization can also be maximized by self-assembling charged lipids on the QD alkyl ligand monolayer to increase solubilization and favorable electrostatic attraction to lipid membranes without diminishing their intrinsic photophysical performance.

7.2 Key Findings

The central theme of Chapters 2–4 was centered on how ligand end groups influenced NP-membrane interactions for ligand-grafted cationic AuNPs, mainly during adsorption and

when individual ligands translocate between leaflet. The key findings form these chapters are:

- Coarse-grained models of AuNPs were individually parameterized through bottom-up approaches using fully atomistic data and can be used with advanced enhanced sampling techniques such as well-tempered metadynamics, the string method with swarms-of-trajectories, umbrella sampling, and replica-exchange simulations. (Chapters 2–4)

- Adsorption of cationic AuNPs to lipid bilayers is favorable when the reaction coordinate is described using two collective variables: NP-bilayer center-of-mass distance (in the z-coordinate) and ligand-lipid contacts. (Chapters 2–3)

- Free energy barriers to adsorption are nonmonotonic with respect to ligand end group lipophilicity. End groups of intermediate lipophilicity and medium alkyl chain length will protrude out of the ligand monolayer and intercalate into the lipid bilayer to minimize membrane disruption. In contrast, short and long alkyl end groups force unfavorable lipid tail protrusions – long alkyl chains will fold back into the ligand monolayer and prevent end group protrusions. (Chapter 2)

- Ligand end group chain architecture, in addition to ligand lipophilicity, influence AuNP adsorption to lipid bilayers. (Chapter 3)

- For end groups with alkyl chains of similar lipophilicities but different chain architectures (*i.e.*, linear vs. branched), adsorption is more thermodynamically favorable for branched ligands and with lower free energy barriers to adsorption. (Chapter 3)

- Ligand end group chemistry weakly influences individual ligand translocation across lipid membranes. Instead, lipid membrane mechanics, influenced by the coordination of polar and charged groups, and by the ligand distribution between leaflets, modulate ligand flipping between bilayer leaflets (Chapter 4)

- Ligands with end groups that induce lateral diffusion of lipids and increase AuNP inclusion into the NP-membrane interface or the transmembrane region promote configurations that facilitate the translocation of the ligand cationic quaternary amine across the hydrophobic bulk of the lipid bilayer. (Chapter 4)

The central theme of Chapters 5–6 was centered on how physical adsorption of lipids on alkyl-capped QDs, either in a membrane-embedded state or as a self-assembled monolayer coating, increase cellular internalization of large NPs. The key findings from these chapters are:

- Coarse-grained models enable simulations of complex membranes where slow lipid reorganization modulate favorable NP-lipid interactions. (Chapters 5–6)

- Lipids with long-chain tails aggregate at NP-membrane interfaces to minimize the line tension induced by large NPs. (Chapter 5)

- Ligands within the monolayer of alkyl-capped QDs rearrange to form spatial voids that allow lipid tails to interlock and minimize the hydrophobic mismatch and increase membrane stability. (Chapter 5)

- The surface of alkyl-capped CdSe/Zn S QDs can be coated with a self-assembled monolayer of cationic and zwitterionic lipids to control macroscopic properties such as solubility and surface charge that allow control over NP-membrane interactions. (Chapter 6)

- Lipid-coated QDs with higher positive surface charge will adsorb more strongly to negatively charged model membranes through counterion displacement and membrane reorganization to localize anionic lipids. (Chapter 6)

7.3 Future Work

The work discussed in this thesis provides invaluable insight on the thermodynamics and mechanisms of interactions underlying NP-membrane biointeractions that will further drive the molecular design and engineering of surface-functionalized NPs for biomedical applications. While these case studies primarily focused on the adsorption of NPs to model lipid membranes, they lay the groundwork for future work in studying more complex and biologically relevant model systems.

7.3.1 Machine-learning a collective variable for AuNP translocation across biomembranes

To further investigate the full translocation of cationic AuNPs across lipid membranes, I propose the implementation of machine-learned collective variables. As discussed throughout this thesis, the collective variables that describe a reaction coordinate of interest are most probably part of a high dimensional space. The choice then becomes a problem of physical interpretation and computational expense – where biasing multiple collective variables can better describe the reaction coordinate but becomes exponentially more expensive. Furthermore, choosing appropriate collective variables introduces human bias. Building on our ligand flipping framework, I plan to implement deep-learning linear discriminant analysis to obtain a collective variable in latent space that maximizes the separation between states. In essence, independent simulations of metastable states will be used to sample a large set of

descriptors (collective variables) that are fed into a neural network for nonlinear dimensionality reduction. Afterwards, linear discriminant analysis on the topmost hidden layer will yield a single collective variable in latent space that describes the transition between the sampled metastable states. This novel framework, known as DeepLDA, has been shown to promote sampling of the transition pathways between two metastable basins through nonlinear paths using suboptimal collective variables.[1, 2] These methods are thus promising for uncovering mechanisms of ligand translocation, mainly where the number of ligands that cross the transmembrane region is unknown.

In this thesis, I looked at individual ligands flipping between leaflets under the assumption that AuNP translocation follows a diffusive pathway where individual ligands flip in sequential order. To overcome this bias and implement the DeepLDA framework, I have performed steered MD simulations where the average angle projected on the z-axis for several ligands is biased as the collective variable. In this case, the NP insertion degree determines the subset of ligands where only those that are at the NP-membrane interface (*e.g.*, maximum contact with membrane lipids) will be biased.

Preliminary results for a fully inserted AuNP show that this collective variable indeed allows multiple different ligands to flip through a variety of mechanisms. While in most replicates, a bundle of neighboring ligands crosses the transmembrane region, strongly deforming the bilayer, individual ligands are also observed to cross. Since these simulations are inexpensive, they provide a platform to apply data-centric approaches for identifying a metastable state correlated to an average number of crossing ligands. This insight is critical in defining the characteristics of metastable states since, to the best of my knowledge, there has been no report on free energy landscapes for NP insertion into lipid bilayers with respect to the ligand distribution between leaflets. By identifying reasonable metastable states with minimal human bias, the DeepLDA framework can then provide a machine-learned collective variable that can better describe the nonlinear transition pathways between these states – enabling free energy calculations using enhanced sampling methods.

7.3.2 Informing the design of lipid-coated QDs through machine learning

The computational framework employed in this thesis to generate lipid-coated QDs and determine their adsorption to model membranes will be used to expand the design space and generate machine learning models that can predict adsorption for new lipid coating formulations. In the present work, I only focused on cationic DOTAP and zwitterionic DLPC lipids to generate the lipid coating and used a model anionic DOPC/DOPG membrane to quantify adsorption. However, I propose systematically evaluating a greater variety of lipids with different properties such as tail saturation, tail chain length, and headgroup charge

and at different concentrations with different sizes of QDs. Simultaneously, more complex and biologically relevant model membranes will be used.[3–6] These large sets of synthetic data can be used to train and evaluate different machine learning models.[7] This ML-guided framework will aid the computational design of lipid-coated QDs while identifying key physicochemical properties and compositional features that drive QD adsorption to realistic biomembranes.

In addition to enabling predictions on lipid formulation for membrane-active lipid-coated QDs, this study will also elucidate mechanisms of interactions for positive predictions. Long timescale simulations will be performed to provide insight on cellular uptake of adsorbed QDs. Specifically, these simulations will show pathways for translocation across biomembranes that will inform about potential cytotoxic effects and critical lipid reorganization that can influence the *in silico – in vivo* pipeline.

References

[1] L. Bonati, V. Rizzi, M. Parrinello, "Data-Driven Collective Variables for Enhanced Sampling", *The Journal of Physical Chemistry Letters* **2020**, *11*, 2998–3004.

[2] L. Bonati, G. Piccini, M. Parrinello, "Deep learning the slow modes for rare events sampling", *Proceedings of the National Academy of Sciences* **2021**, *118*, e2113533118.

[3] R. Vaiwala, K. G. Ayappa, "Martini-3 Coarse-Grained Models for the Bacterial Lipopolysaccharide Outer Membrane of Escherichia coli", *Journal of Chemical Theory and Computation* **2024**, *20*, 1704–1716.

[4] T. N. Ozturk, M. König, T. S. Carpenter, K. B. Pedersen, T. A. Wassenaar, H. I. Ingólfsson, S. J. Marrink in *Biophysical Approaches for the Study of Membrane Structure—Part B: Theory and Simulations*, (Eds.: M. Deserno, T. Baumgart), Methods in Enzymology, Academic Press, **2024**, pp. 237–285.

[5] H. I. Ingólfsson, T. S. Carpenter, H. Bhatia, P.-T. Bremer, S. J. Marrink, F. C. Lightstone, "Computational Lipidomics of the Neuronal Plasma Membrane", *Biophysical Journal* **2017**, *113*, 2271–2280.

[6] H. I. Ingólfsson, M. N. Melo, F. J. van Eerden, C. Arnarez, C. A. Lopez, T. A. Wassenaar, X. Periole, A. H. de Vries, D. P. Tieleman, S. J. Marrink, "Lipid Organization of the Plasma Membrane", *Journal of the American Chemical Society* **2014**, *136*, 14554–14559.

[7] G. Kumar, A. M. Ardekani, "Machine-Learning Framework to Predict the Performance of Lipid Nanoparticles for Nucleic Acid Delivery", *ACS Applied Bio Materials* **2025**, *8*, 3717–3727.